Actuator and Sensor Design and Modeling for Structural Acoustic Control

by

Robert Jeffrey Pascal

B.S., Aerospace Engineering
The University of Texas at Austin, 1994

SUBMITTED TO THE DEPARTMENT OF AERONAUTICS AND ASTRONAUTICS
IN PARTIAL FULFILLMENT OF THE DEGREE OF

MASTER OF SCIENCE IN AERONAUTICS AND ASTRONAUTICS

AT THE

MASSACHUSETTS INSTITUTE OF TECHNOLOGY

MAY 1999

Signature of Author .....
Department of Aeronautics and Astronautics
May 21, 1999

Certified by.....
David W. Miller
Professor of Aeronautics and Astronautics
Thesis Supervisor

Accepted by .....
Jaime Peraire
Professor of Aeronautics and Astronautics
Chairman, Department Graduate Committee

Actuator and Sensor Design and Modeling for Structural Acoustic Control

by

ROBERT JEFFREY PASCAL

Submitted to the Department of Aeronautics and Astronautics
on May 21, 1999 in Partial Fulfillment of the
Requirements for the Degree of Master of Science
at the Massachusetts Institute of Technology

ABSTRACT

The use of a high-fidelity finite element model is investigated for the design and closed-loop performance prediction of shaped and distributed sensors and actuators for structural acoustic control. Sensor and actuator design was found to be sensitive to nodeline discrepancies between the model and experiment caused by moderate manufacturing defects and/or boundary condition uncertainties. Relying on the finite element model for sensor shaping or distribution results in a slight difference between the desired and achieved sensor performance. The modeshape sensitivity is compounded when both the actuator and sensor are shaped or distributed, as is the case with a distributed sensuator design. This results in an unacceptable difference between the desired and achieved distributed sensuator performance. Since the advantages of shaping and distribution can be gained either at the system input (actuators) or output (sensors), modeshape information from a correlated analytic model should be used for one or the other, but not both. Experimental verification of critical modeshapes is also recommended to reduce sensor and actuator performance loss.

The finite element model was also used to predict achievable closed-loop acoustic performance for various sensor and actuator pairs for transmission and reflection control. Since a finite element model is generally not accurate enough to be used as the basis for high performance compensator design, the predicted performance was compared to experimental results of compensators designed with an accurate data-fit model using the same control design methods. Good correlation was achieved between predicted and implemented results for linear behavior of the system.

Finally, a comparison was made between a modally shaped PVDF sensor/PZT actuator design and a single wafer PZT sensuator. Both have desirable open-loop characteristics and comparable predicted performance. The predicted performance could not be implemented for the sensuator design due to a severe amplitude non-linearity. The PVDF sensor design is very linear, and the implemented performance slightly exceeded that predicted using the finite element model. Due to the implementation difficulties of the

sensuator, the PVDF sensor/PZT actuator design is the better choice for acoustic transmission control.

Thesis Supervisor:
Professor David W. Miller
Dept. of Aeronautics and Astronautics

ACKNOWLEDGMENTS

Funding for this research was provided by the U.S. Air Force Office of Scientific Research (AFOSR), under AASERT Grant No. F49620-97-1-0358 (Parent Grant No. F49620-96-1-0290) with Capt. Brian Sanders as the AFOSR contract monitor, Charlotte Morse as the MIT senior contract administrator, SharonLeah Brown as the MIT fiscal officer, and Karen Buck as the AFOSR contract administrator.

Continuous guidance for the research was provided by Professor David Miller. The foundation for this research was laid by Dr. Roger Glaese, who was always eager to offer detailed explanations of his work. Much of this research occurred in parallel with the work of Koji Asari, whose advice and support is greatly appreciated. Collaboration with Dr. Steve Griffin of AFRL during a January 1998 visit proved to be an extremely valuable experience, as well as the basis for continued interaction. Dr. Carl Blaurock of Mide Technology Corporation was consulted on many occasions for his knowledge of shaped PVDF sensors. Carlos Gutierrez assisted with and is continuing the work on the active membrane. Last but not least, the sensuator work could not have been accomplished without the electronics expertise and patience of Paul Bauer.

TABLE OF CONTENTS

LIST OF FIGURES

LIST OF TABLES

NOMENCLATURE

$(\cdot)_{\mathbf{spt}}$	Matrix of top speaker
$(\cdot)_{\mathbf{spb}}$	Matrix of bottom speaker
$(\cdot)_{\mathbf{p}}$	Matrix of plate
$(\cdot)_{\mathbf{ft}}$	Matrix of top acoustic chamber
$(\cdot)_{\mathbf{fb}}$	Matrix of bottom acoustic chamber
$(\cdot)_{\mathbf{r}}$	Matrix in modal coordinates
ϕ	Matrix of uncoupled, mass normalized modeshapes
ρ	Density of air
υ	Poisson's ratio
Ω	Diagonal matrix of natural frequencies
ζ	Modal damping ratios
$\mathbf{A}_{(\cdot\cdot)}$	FEM fluid-structure coupling matrix in physical coordinates
A, B, C, D	State space system, input, output, and feedthrough matrices
c_o	Wave propagation speed
C_{piez}	Blocked capacitance of PZT sensuator
C_{REF}	Reference capacitor in sensuator circuit
C_{SP}, C_{SR}	Charge sensor capacitors for piezo and reference leg of sensuator circuit
d_{31}	Piezoelectric strain coefficient in x-direction for electric field in z-direction
E	Young's modulus
G_R	Tuning gain for sensuator circuit
K	FEM stiffness matrix in physical coordinates
M	FEM mass matrix in physical coordinates
P	Pressure degrees of freedom in physical coordinates
$\underline{q}$	Structural and pressure degrees of freedom in modal coordinates
u	State space input vector
w	Out-of-plane structural displacement
$\underline{x}$	Structural degrees of freedom in physical coordinates (x, y, z, Rx, Ry, Rz)
y	State space output vector

Chapter 1

INTRODUCTION

1.1 Motivation

Vibro-acoustic loads during launch are by far the most severe vibration environment a payload experiences during its service life. This loading condition is often the design load for much of the payload structure. Significantly reducing this environment could result in lighter payload structures, and/or reduced spacecraft failures. Passive methods such as mass loading and acoustic blankets are currently used to reduce the acoustic environment inside a payload fairing; however, recent research has focused on active methods which hold promise for much greater acoustic attenuation. [Leo & Anderson, 1996]

As with any active control method, the achievable performance is closely linked to the choice of sensors and actuators. The type, shape, and distribution of sensors and actuators with respect to the dynamics of the structure determine the characteristics of the transfer functions ultimately used in a closed-loop control system. Careful design of the sensors and actuators can lead to very favorable transfer function attributes such as modal filtering, rolloff, and bounded phase over a frequency region. The best sensor and actuator design for achieving these attributes requires very accurate knowledge of the coupled structural-acoustic dynamics.

Several modeling methods are currently used to predict response of a structural-acoustic system. These include Statistical Energy Analysis (SEA), data identification models,

wave models, and finite element models. Only the latter two are appropriate for sensor and actuator design since they retain the physics of individual dynamic modes; however, these models are not very accurate unless correlated extensively with experimental data. The finite element method is widely used because it offers the flexibility required for model correlation. The motivation for this thesis is to better define the capabilities and limitations of a correlated finite element model for sensor and actuator design. Additionally, the prediction of closed-loop performance using a sensor/actuator pair is motivated by its obvious value to the design process.

1.2 Transmission Control

Vibro-acoustic energy from the launch vehicle engines must follow one of the following transmission paths in order to enter the payload fairing. The first is the direct structural load path supporting the fairing and payload. Energy traveling this path vibrates both the fairing and payload, both of which excite the enclosed acoustic field. The second path is acoustic transmission, where acoustic energy from the external field vibrates the payload fairing which then excites the enclosed acoustic field. This second path is the focus of transmission control for this research.

1.2.1 Passive Structural Redesign

The first option that should always be considered when solving a structural-acoustic or vibration control problem is passive structural redesign. For the acoustic transmission problem, this includes the effect of varying the structural mass and stiffness, or adding passive structural damping treatments. For this investigation, a wave model of a single degree of freedom oscillator (simple structural model) dividing a non-reverberant acoustic far-field (external acoustic field) from a reverberant acoustic enclosure (fairing) was used. This model is developed in Appendix D. The structural and acoustic parameters were set to be similar to the acoustic test chamber used in this research. The disturbance source for this model is an incoming acoustic wave in the non-reverberant far field.

Table 1.1 shows the acoustic performance improvements due to varying the structural parameters in the model. The performance was evaluated as the root sum square of five equally spaced pressure locations in the acoustic enclosure over a frequency range of 10Hz - 1kHz. The nominal performance is for 1% structural and 1% acoustic damping ratios.

TABLE 1.1 Effect of structural redesign on acoustic transmission

Structural Variation	Performance Improvement
5% Damping	0.92 dB
10% Mass Increase	0.70 dB
10% Mass Decrease	-0.81 dB
10% Stiffness Increase	-0.03 dB
10% Stiffness Decrease	0.004 dB

Increasing the structural damping or mass is seen to have a moderate effect on the performance. The performance is fairly insensitive to variations in structural stiffness. These performance trends are dependent on the acoustic resonances being at higher frequency than the fundamental structural mode. Adding mass causes attenuation at frequencies above the structural resonance, damping causes attenuation at the resonance, and stiffness causes attenuation below the structural resonance. Since almost all of the acoustic energy is at or above the structural resonance, adding structural mass or damping are the two primary passive options. Addition of non-structural mass is the most common form of passive structural redesign currently used to reduce acoustic transmission in payload fairings. [Leo & Anderson, 1996]

Another trend seen in Table 1.1 is that both increasing stiffness and decreasing mass cause an increase in the acoustic energy transmitted into the enclosure. This combination is similar to the effect of changing from a built-up aluminum to a composite fairing design. In addition, composite structures tend to have less damping than built-up metal ones. This

simple model therefore captures the trend that composite fairing designs generally exhibit which makes the enclosed acoustic environment more severe. [Denoyer, et al., 1998]

1.2.2 Active Transmission Control

The performance improvement achievable through passive means is only moderate, and for the case of composite fairings may only return the acoustic environment to the levels expected for a built-up aluminum fairing. The high launch cost per pound also presents practical limits on the use of added mass or passive damping treatments, and motivates the investigation of active control techniques for acoustic transmission. Feedback compensators which effectively add active damping to a structure can achieve very large equivalent damping ratios. A structural damping ratio of 50% actively added to the oscillator in the wave model produces an acoustic performance improvement of 4.30 dB.

Table 1.2 presents a limited survey of recent work in active transmission control. Prior to 1994, most of the work in the field was limited to control of tonal disturbances, and used point sensors (e.g. microphones or accelerometers) or crudely distributed strain sensors (e.g. PVDF strips). Much of this work also included a feedforward measure of the disturbance source in the control calculation. More recent work has utilized gain weighted sensor arrays, or shaped sensors to filter the structural modes which contribute most to acoustic transmission. The experimental research is generally limited to simple plate structures where analytic modeshapes are used for shaping the sensors. Other research presents only numerical simulations of control performance. An exception to this is the work of Denoyer et al. [Denoyer, et al., 1998] where a purely experimental method was used to choose sensor and actuator distribution for a scale payload fairing structure.

Advancing the use of shaped and distributed sensors and actuators to complex structures requires accurate knowledge of the structural modeshapes and their coupling to the acoustic field. The most likely method for obtaining this information is through a high-fidelity finite element model. One of the major goals of this thesis is to investigate the capabilities and limitations of a finite element model for sensor and actuator shaping, as well as pre-

TABLE 1.2 Survey of active structural acoustic transmission control research

Method	Actuators	Sensors	Disturbance	Reference
Feedforward	Point Force	Mic & Accel.	Narrowband	[Fuller, et al., 1989]
Feedback	PZT	PVDF strips	Narrowband	[Clark & Fuller, 1992]
Feedback	PZT	Accel.	Broadband	[Koshigoe et al., 1993]
Feedforward	PZT	Mic Array	Narrowband	[Fuller & Gibbs, 1994]
Feedback	PZT	Accel.	Broadband	[Falangas, et al., 1994]
Feedforward	PZT	Mic.	Narrowband	[Wang, et al., 1994]
Feedback	PZT	PZT	Broadband	[Ko & Tongue, 1995]
Feedback	PZT	Mic Array	Broadband	[Vadali & Das, 1996]
Feedback	PZT	Strain	Broadband	[Leo & Anderson, 1996]
Feedback	PZT	Pressure	Broadband	[Glaese, 1997]
Feedback	PZT	PVDF	Broadband	[Denoyer, et al., 1998]

dicting closed-loop compensator performance. The research is limited to a simple plate structure; however, the method is only limited by the model accuracy, not structural complexity.

1.3 Reflection Control

Regardless of the control method used, some vibro-acoustic energy will be transmitted into the payload fairing through both of the transmission paths. The acoustics of the fairing will filter this energy and cause large amplifications at the acoustic resonances of the enclosure. The resonances are caused by the constructive interference of transmitted and reflected waves inside the fairing. The goal of reflection control is to limit the reflection of the acoustic waves inside the fairing, thus attenuating the amplitude of the acoustic resonances.

1.3.1 Passive Acoustic Damping

Adding acoustic damping in the form of blankets is the most effective passive means of attenuating the acoustic environment inside a payload fairing. As an example of this, if the

acoustic damping ratio in the wave model were increased to 5%, the broadband performance would improve by 3.95 dB. Unfortunately, the attenuation from acoustic blankets is limited to frequencies where the blanket thickness is a significant fraction of the acoustic wavelength. This makes low frequency reflection control using blankets impractical due to weight and space constraints. Typical acoustic blankets are 2 to 4 in. thick, and provide effective acoustic attenuation beginning at 300 to 400 Hz. [Leo & Anderson, 1996]

1.3.2 Active Reflection Control

Two active approaches are available for limiting the constructive interference of reflected acoustic waves inside an enclosure. The first is Active Noise Control (ANC), and the second is Active Structural Acoustic Control (ASAC).

ANC relies on secondary acoustic sources, such as speakers, to create acoustic waves which destructively interfere with the transmitted and reflected waves at the location of the feedback sensors. This method is generally limited to tonal disturbances (e.g. propeller noise), and normally uses a feedforward measurement of the disturbance source. Additionally, ANC only guarantees attenuation at the location of the feedback microphones, which makes it unacceptable for broadband, global reflection control.

ASAC relies on controlling the structural vibration with actuators and sensors to globally attenuate the broadband acoustic environment. Active transmission control described in the previous section is a form of ASAC. Impedance matching is a wave reflection control method that was extended to ASAC by Glaese. [Glaese, 1997] An advantage of the impedance matching approach is that it only requires a local wave model of the structural reflection and transmission characteristics to achieve global acoustic attenuation. A practical limitation is that it requires observability of the acoustic modes through the structural vibration to resolve the incoming and outgoing components of the acoustic energy. Due to the mass of the structure, the observability of the acoustic modes using a structural sensor is typically poor, which limits the performance of the impedance matching approach. Although little work in this thesis focuses on reflection control, a sensor and actuator on a

membrane was investigated which improves the observability of acoustic modes in the structural vibration. This work is presented in Appendix C, with suggestions for its future use given in Chapter 6.

1.4 Approach for Current Research

It is apparent from the simple wave model that the mass vs. performance associated with passive methods, except acoustic blankets for high frequency attenuation, is unacceptable for broadband acoustic launch load alleviation in payload fairings. The goal for this research program is thus to develop an active transmission and reflection control system for low frequencies (< 500 Hz) to augment acoustic blankets. As part of that goal, this thesis focuses on the design and modeling of shaped and distributed sensors and actuators for active transmission control.

The shaping and placement of distributed sensors and actuators is determined by the system dynamics. Additionally, the input/output characteristics of an actuator/sensor pair limit achievable closed-loop performance. This thesis therefore has three objectives: 1) creation of a high-fidelity finite element model that captures the dynamics of a coupled structural-acoustic system; 2) determination of the capabilities and limitations of this finite element model for actuator and sensor design and placement; 3) determination of the capabilities and limitations of this finite element model for prediction of closed-loop acoustic compensator performance. Conclusions will be drawn on each of these objectives, as well as comparison of two types of actuator/sensor configurations that are promising for active structural acoustic transmission control.

1.4.1 Experimental Description

The test chamber configuration for the finite element model and experiments consists of a 1/32 in. thick aluminum plate dividing a 52 in. long chamber into an 11 in. "exterior" section and 41 in. "interior" section as shown in Figure 1.1. The disturbance source is white noise from the speaker at the top of the chamber. The "exterior" section of the chamber is

lined with acoustic foam to minimize reverberation. The "interior" section is lined with a small amount of foam and fiberglass to simulate high frequency attenuation from acoustic blankets. Three microphones provide a distributed performance metric of the "interior" acoustics. A speaker at the bottom of the chamber is used to control "interior" acoustic modes.

Several "active" plates were created that could be placed in the chamber. The one shown in the figure has a single PZT wafer as an actuator and a modally shaped PVDF sensor. Other plates used accelerometers, strain gages, or a simultaneous PZT sensor/actuator (Sensuator) for active transmission control.

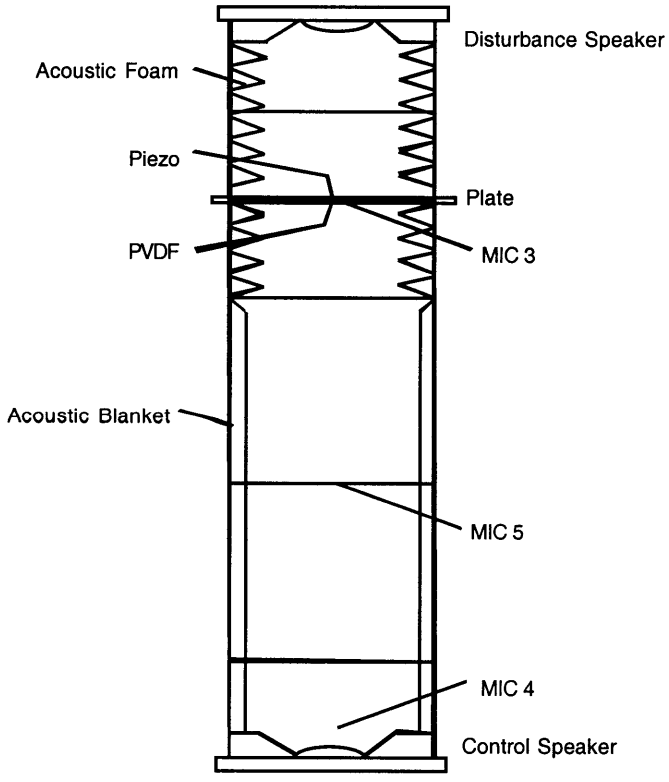

Figure 1.1 Diagram of acoustic test chamber configuration.

In some instances, especially during structural identification and initial sensor/actuator testing, an open chamber configuration was used to reduce the effect of the structural-

acoustic coupling. This configuration consists of the plate clamped between two 7.5 in. long chamber sections. One of the speakers is placed below these sections and separated by three 1.0 in steel bolts. The purpose of the gap is to prevent the acoustic stiffening of the plate that would be present from an enclosure, but still maintain the ability to excite the plate dynamics acoustically. A diagram of the open chamber configuration is shown in Figure 1.2.

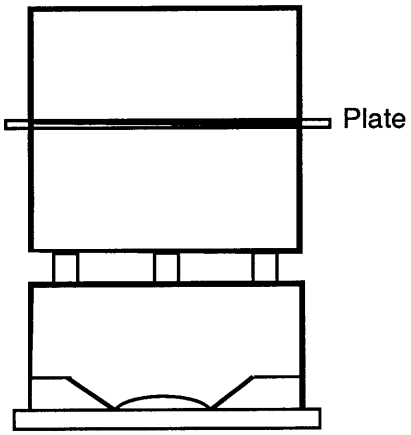

Figure 1.2 Diagram of open chamber configuration used for structural identification and initial sensor/actuator testing.

1.4.2 Thesis Outline

- Finite element modeling
- Sensor/Actuator design using the finite element model
- Predicted closed-loop performance using the finite element model
- Experimental validation of closed-loop performance predictions
- Conclusions

Chapter 2

FINITE ELEMENT MODELING

2.1 Discussion of Model Fidelity and Uses

The Finite Element Method (FEM) has become an industry standard modeling tool for structural design, analysis and research. This method lends itself especially well to coupled structural-acoustic modeling since the governing wave equation of an acoustic enclosure is a simplification to that of an elastic solid. As with any modeling method, the complexity of a finite element model is driven by the intended use of its results. Capabilities of FEM span from basic physical understanding of a complex structure or system to accurate quantitative analysis of the response of a system to a set of inputs. A few of the typical uses of a finite element model are described below in order of increasing model complexity.

The most basic use of a finite element model is to provide a physical understanding of a system. For a structural acoustic system this use includes understanding how structural motion results in pressure distributions in the acoustic fluid, or how changes in structural mass, stiffness or damping affect the coupled acoustic field and vice versa. At this low level, a relatively simple model, often of reduced geometry or dimension, is sufficient and sensor/actuator modeling is usually not required.

The next higher level is a conceptual design model used for evaluating the feasibility of an idea on a specific system. At this level, the model should be representative of the geome-

try of the system, and capture basic dynamic response properties such as modal frequency, damping, residue and density reasonably well. Correlation of the model to an actual system is not important at this level because of the assumption that performance predicted on the model will reflect performance achievable on a similar physical system once accurate models are obtained. An example of the use of this level of FEM for a structural acoustic system is the virtual 3-D control experiment of Glaese. [Glaese, 1997]

A significant improvement to the conceptual design model involves correlation with an actual system. Here sensor and actuator modeling becomes vital to accurately capture the input/output characteristics of the physical system. Correlation is achieved by modifying unknown or uncertain parameters to match data from the physical system. The term system identification model will be used to describe this level since one of the important uses is to identify the nature of unknown modes in the experimental transfer functions.

The final level of a finite element model is a high-fidelity analysis model. This level is characterized by the ability to accurately predict response other than the input/output responses used for model correlation. The most significant example for this research is the use of a finite element model to design a compensator that is implemented on the physical system. Not only do the individual input/output transfer functions need to be accurate, but their combined closed-loop error and bandwidth must be within stability and performance tolerances. This level of model was used to design 0-g compensators for the Middeck Active Control Experiment (MACE) flown on STS 67 after correlating the input/output response in the laboratory at 1-g. [Glaese, 1994]

A large part of the research presented in this thesis is dependent on the development and correlation of a high-fidelity finite element model of the MIT acoustic test chamber, and subsequent use of this model to design shaped and distributed sensors and actuators and predict closed-loop performance. The remainder of this chapter describes the modeling procedure, assumptions and open-loop correlation for this model.

2.2 Structural Acoustic Modeling in ANSYS

The commercial FEM software ANSYS was used for the creation and eigensolution of the structural acoustic model of the acoustic test chamber. A commercial package was chosen for several reasons. First, it provides a graphical interface for pre- and post-processing which minimizes the likelihood of modeling errors. Second, the elements are proven and solution methods optimized to minimize computation time. Finally, the software provides enough flexibility in both the pre- and post-processing stages to allow the model to build upon methods used in previous research.

The acoustic test chamber is a 52 in. long, 11.75 in. diameter steel pipe with low frequency speakers at the top and bottom ends. The configuration for this research includes a 0.032 in. thick aluminum plate inserted 11 in. below the top speaker to divide the chamber into two sections. The chamber has circular symmetry about its vertical axis, and keeping this symmetry in the mesh of the finite element model will allow for an investigation of a reduced solution method called circulance (Appendix B). The mesh chosen for the dividing plate is a modification of that used by Grocott in his work on flexible active mirrors. [Grocott, 1997]

A MATLAB code is used to create geometric entities (keypoints and areas) for the mesh. This geometry is imported into ANSYS for meshing with quadrilateral and triangular shell elements with 6 degrees of freedom (DOF) per node (three translations and three rotations, $\underline{x}$). A clamped boundary condition is used around the edge of the plate. The two dimensional plate mesh is then extruded vertically to form triangular and rectangular prism acoustic elements. These elements have only 1 DOF per node (pressure, P) except at the interface with a structure where they have 7 (6 structural and 1 pressure). A rigid boundary condition is assumed by ANSYS for the acoustic fluid except where it is in contact with a flexible structure. Finally, the speakers on the top and bottom of the chamber are modeled as relatively rigid shell elements with a grounded spring accounting for the single DOF piston motion of the speakers.

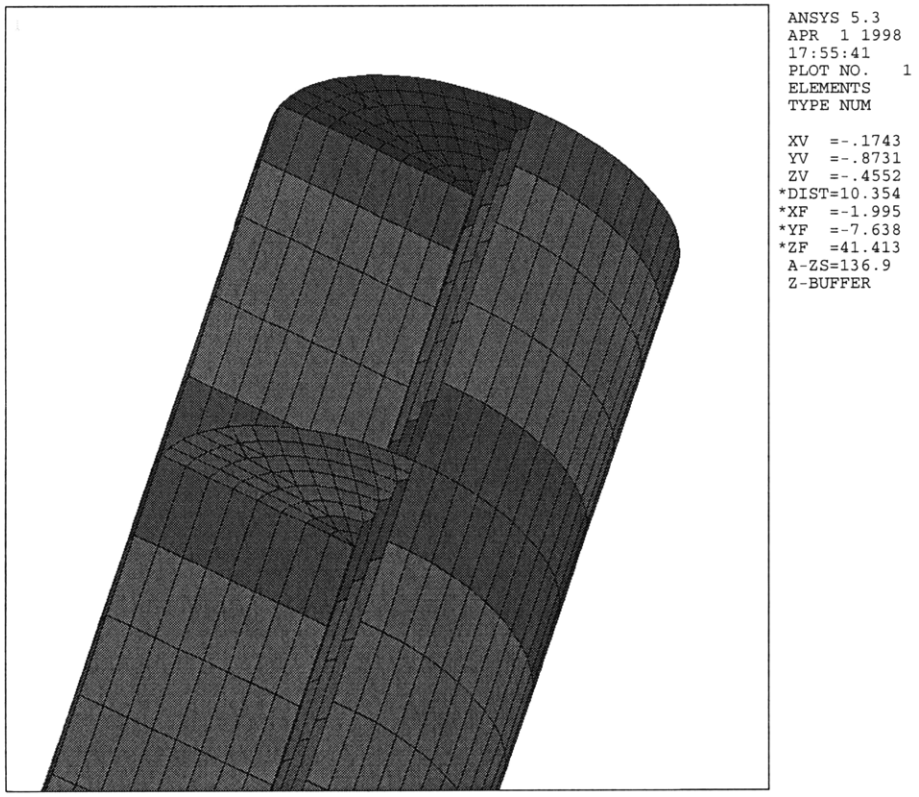

Figure 2.1 ANSYS mesh of chamber finite element model with wedge cutaway from acoustic elements to expose structural components.

Since there is only 1 pressure DOF at each node, and the plate creates a pressure discontinuity between the top and bottom sections of the chamber, a second "dummy" set of shell elements must be created for the plate with nodes coincident with the first. This "dummy" plate is given no structural stiffness or mass, but the structural DOF are coupled to those of the actual plate model. This technique does not affect the structural behavior of the plate, but allows for separate pressure DOF on the upper and lower side of the plate which is required. This method is not necessary for the speaker models since they only interface with the acoustic elements on one side. The back-side acoustic stiffness of the speakers is lumped into the spring using measured data of the speakers outside the chamber.

The unforced finite element equations of motion in nodal coordinates are given in (2.1). [ANSYS Users Manual, 1992] In this equation, the subscripts spt, spb, p, ft, and fb corre-

spond to the top speaker, bottom speaker, plate, top acoustic chamber, and bottom acoustic chamber respectively. These equations show how the fluid-structure coupling matrices $\mathbf{A_{spt}}$, $\mathbf{A_{spb}}$, $\mathbf{A_{pt}}$, and $\mathbf{A_{pb}}$ enter the mass and stiffness matrix, and the unsymmetric nature of the coupled system.

$$\begin{bmatrix} \mathbf{M_{spt}} & \mathbf{0} & \mathbf{0} & \mathbf{0} & \mathbf{0} \\ \mathbf{0} & \mathbf{M_{spb}} & \mathbf{0} & \mathbf{0} & \mathbf{0} \\ \mathbf{0} & \mathbf{0} & \mathbf{M_p} & \mathbf{0} & \mathbf{0} \\ -\rho\mathbf{A_{spt}} & \mathbf{0} & -\rho\mathbf{A_{pt}} & \mathbf{M_{ft}} & \mathbf{0} \\ \mathbf{0} & -\rho\mathbf{A_{spb}} & -\rho\mathbf{A_{pb}} & \mathbf{0} & \mathbf{M_{fb}} \end{bmatrix} \begin{bmatrix} \ddot{x} \\ \ddot{P} \end{bmatrix} + \begin{bmatrix} \mathbf{K_{spt}} & \mathbf{0} & \mathbf{0} & \mathbf{A_{spt}} & \mathbf{0} \\ \mathbf{0} & \mathbf{K_{spb}} & \mathbf{0} & \mathbf{0} & \mathbf{A_{spb}} \\ \mathbf{0} & \mathbf{0} & \mathbf{K_p} & \mathbf{A_{pt}} & \mathbf{A_{pb}} \\ \mathbf{0} & \mathbf{0} & \mathbf{0} & \mathbf{K_{ft}} & \mathbf{0} \\ \mathbf{0} & \mathbf{0} & \mathbf{0} & \mathbf{0} & \mathbf{K_{fb}} \end{bmatrix} \begin{bmatrix} x \\ P \end{bmatrix} = 0 \tag{2.1}$$

The unsymmetric matrix equations of motion can be solved directly in ANSYS using an iterative solution method. This method is computationally expensive, and can be avoided if the uncoupled mode shapes form an acceptable basis for the coupled system. This is a valid assumption for this model since the plate and speakers are massive and stiff compared to the acoustic fluid. This assumption allows for the use of the Lanchoz method to efficiently solve for the mass normalized mode shapes and frequencies of the two speakers, plate, and two acoustic enclosures separately. Each of these uncoupled systems are symmetric, and can be solved directly. Additionally, a partial solution is run in ANSYS to create the full unsymmetric mass and stiffness matrices, and the fluid structure coupling matrices are extracted. The next section will explain how the component modes and coupling matrices are assembled to form a coupled modal state space model.

2.3 Modal State Space Approach

The method to create a modal state space model using the uncoupled component modes and fluid structure coupling matrices is presented by Glaese. [Glaese, 1997] The first 40 modes of the plate, 26 modes of the upper acoustic chamber, and 30 modes of the lower acoustic chamber are used along with the piston modes of the two speakers. This set includes all of the component modes up to 1250 Hz.

Equation (2.2) shows the coordinate transformation from nodal coordinates to modal coordinates using the uncoupled component modes. This transformation is applied to (2.1), and the unforced system is pre-multiplied by Φ^T to give the modal equations of motion (2.3). Recall that the component modes were each mass normalized. This eliminates the need to perform all of the matrix multiplications except for the coupling terms, and the modal mass and stiffness matrices take the form given in (2.4)

A diagonal modal damping matrix is used as shown in (2.5). The damping ratios are a variable used to correlate the finite element model to data from the chamber. Table 2.1 lists the damping ratios used for the chamber configuration in this thesis. The damping ratio of the first structural mode is high because of its coupling to both acoustic chambers. The damping of the top acoustic chamber reflects thick acoustic foam used to simulate a far field effect. The damping of the bottom acoustic chamber reflects the use of a fiberglass blanket to simulate acoustic blankets present in payload fairings.

TABLE 2.1 Modal damping ratios for finite element model

Mode Description	Damping Ratio (ζ)
Speaker Piston Mode	0.102
First Symmetric Plate Mode	0.06
All Other Plate Modes	0.03
Top Chamber Acoustic Modes	0.2
Bottom Chamber Acoustic Modes	0.02

$$\begin{bmatrix} \underline{x} \\ P \end{bmatrix} = \begin{bmatrix} \phi_{spt} & 0 & 0 & 0 & 0 \\ 0 & \phi_{spb} & 0 & 0 & 0 \\ 0 & 0 & \phi_p & 0 & 0 \\ 0 & 0 & 0 & \phi_{ft} & 0 \\ 0 & 0 & 0 & 0 & \phi_{fb} \end{bmatrix} \underline{q} = \Phi \underline{q} \tag{2.2}$$

$$\Phi^T \begin{bmatrix} M_{spt} & 0 & 0 & 0 & 0 \\ 0 & M_{spb} & 0 & 0 & 0 \\ 0 & 0 & M_p & 0 & 0 \\ -\rho A_{spt} & 0 & -\rho A_{pt} & M_{ft} & 0 \\ 0 & -\rho A_{spb} & -\rho A_{pb} & 0 & M_{fb} \end{bmatrix} \Phi \ddot{\mathbf{q}} + \tag{2.3}$$

$$\Phi^T \begin{bmatrix} K_{spt} & 0 & 0 & A_{spt} & 0 \\ 0 & K_{spb} & 0 & 0 & A_{spb} \\ 0 & 0 & K_p & A_{pt} & A_{pb} \\ 0 & 0 & 0 & K_{ft} & 0 \\ 0 & 0 & 0 & 0 & K_{fb} \end{bmatrix} \Phi \mathbf{q} = 0$$

$$\mathbf{M_r} = \begin{bmatrix} I & 0 & 0 & 0 & 0 \\ 0 & I & 0 & 0 & 0 \\ 0 & 0 & I & 0 & 0 \\ -\rho \phi^T_{ft} A_{spt} \phi_{spt} & 0 & -\rho \phi^T_{ft} A_{pt} \phi_p & I & 0 \\ 0 & -\rho \phi^T_{fb} A_{spb} \phi_{spb} & -\rho \phi^T_{fb} A_{pb} \phi_p & 0 & I \end{bmatrix} \tag{2.4}$$

$$\mathbf{K_r} = \begin{bmatrix} \Omega_{spt}^2 & 0 & 0 & \phi^T_{spt} A_{spt} \phi_{ft} & 0 \\ 0 & \Omega_{spb}^2 & 0 & 0 & \phi^T_{spb} A_{spb} \phi_{fb} \\ 0 & 0 & \Omega_p^2 & \phi^T_p A_{pt} \phi_{ft} & \phi^T_p A_{pb} \phi_{fb} \\ 0 & 0 & 0 & \Omega_{ft}^2 & 0 \\ 0 & 0 & 0 & 0 & \Omega_{fb}^2 \end{bmatrix}$$

$$\mathbf{Cr} = \begin{bmatrix} 2\varsigma_{spt}\Omega_{spt} & 0 & 0 & 0 & 0 \\ 0 & 2\varsigma_{spb}\Omega_{spb} & 0 & 0 & 0 \\ 0 & 0 & 2\varsigma_{p}\Omega_{p} & 0 & 0 \\ 0 & 0 & 0 & 2\varsigma_{ft}\Omega_{ft} & 0 \\ 0 & 0 & 0 & 0 & 2\varsigma_{fb}\Omega_{fb} \end{bmatrix} \tag{2.5}$$

With the modal mass, stiffness and damping matrices known, the modal state space system matrix (**A**) can be assembled in the standard manner. This involves pre-multiplying (2.3) by $\mathbf{M_r}^{-1}$, and solving for $\ddot{q}$. The state space system is shown in (2.6), with the form of the **A** matrix given explicitly. To complete the state space model, the effect of various sensors and actuators must be modeled and transformed to modal coordinates to form the forcing, sensing and feed-through matrices (**B**,**C** and **D**). Sensor and actuator modeling is the topic of the next section.

$$\begin{bmatrix} \dot{q} \\ \ddot{q} \end{bmatrix} = \begin{bmatrix} \mathbf{0} & \mathbf{I} \\ -\mathbf{M_r}^{-1}\mathbf{K_r} & -\mathbf{M_r}^{-1}\mathbf{C_r} \end{bmatrix} \begin{bmatrix} q \\ \dot{q} \end{bmatrix} + \begin{bmatrix} \mathbf{0} \\ \mathbf{B} \end{bmatrix} u \tag{2.6}$$

$$y = \mathbf{C} \begin{bmatrix} q \\ \dot{q} \end{bmatrix} + \mathbf{D}u$$

2.4 Sensor and Actuator Modeling

Sensors and actuators are modeled to capture their effect on the input/output behavior of the chamber. The basic method for modeling the sensors and actuators involves 4 steps:

- Model the stiffness and mass of the sensor or actuator in ANSYS so the modal basis will reflect these passive properties.
- Create the forcing or sensing matrices in nodal coordinates. This may be as simple as selecting a single DOF, or involve interpolating between nodal positions and summing the effect of a distributed sensor or actuator.
- Transform to modal coordinates by pre-multiplying the forcing matrix by Φ^{T} or

post-multiplying a sensing matrix by Φ.

- Model any sensor or actuator dynamics that are within the bandwidth of the finite element model.

Figure 2.2 is a block diagram of the input/output model. Note that both the input and output variables are voltage which must be related to physical forces and sensed variables through sensor and actuator modeling.

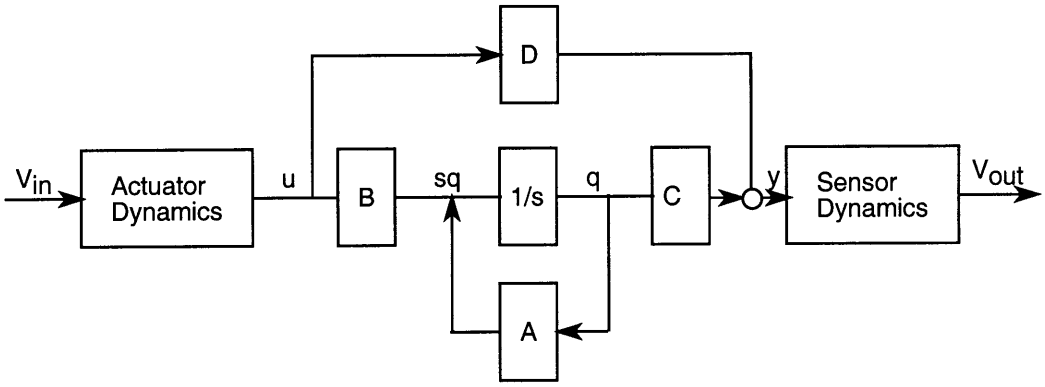

Figure 2.2 Block diagram of input/output characteristics of finite element model.

2.4.1 Microphones

Modeling a microphone is described first since it is the simplest of the sensors and actuators. The microphones are physically placed inside the acoustic chamber, and do not significantly affect the acoustics since the dimension of the microphones is much less than the smallest acoustic wavelength of interest. This eliminates the need for step one in the modeling process. Additionally, the sensing matrix in nodal coordinates simply selects the pressure DOF of the node where the microphone is placed. The model is not very sensitive to exact microphone location, so interpolation of pressure between nodes in not necessary. Finally, the microphone dynamics are well above the bandwidth of the model, and can be ignored without affecting the fidelity. This reduces the sensor dynamics to a scalar representing the gains in the data acquisition system.

Equation (2.7) is a typical sensing matrix in nodal coordinates. The sub-matrices $\mathbf{C}_{yx}$, $\mathbf{C}_{yp}$, $\mathbf{C}_{y\dot{x}}$, and $\mathbf{C}_{y\dot{p}}$, select the nodal structural and pressure DOF and their derivatives which form the output characteristics of the sensor. For a microphone, the only non-zero submatrix is $\mathbf{C}_{yp}$. Equation (2.8) shows the transformation to modal coordinates, and explicitly how only part of this transformation is necessary due to the sparseness of $\mathbf{C}_y$.

$$\mathbf{C}_y = \begin{bmatrix} \mathbf{C}_{yx} & \mathbf{C}_{yp} & \mathbf{C}_{y\dot{x}} & \mathbf{C}_{y\dot{p}} \end{bmatrix} \begin{bmatrix} \underline{x} \\ P \\ \underline{\dot{x}} \\ \dot{P} \end{bmatrix} \tag{2.7}$$

$$\mathbf{C}_{\mathbf{mic}} = k\mathbf{C}_y \begin{bmatrix} \Phi & 0 \\ 0 & \Phi \end{bmatrix} \begin{bmatrix} q \\ \dot{q} \end{bmatrix} = k \begin{bmatrix} 0 & \mathbf{C}_{yp} \begin{bmatrix} \phi_{\mathbf{ft}} & 0 \\ 0 & \phi_{\mathbf{fb}} \end{bmatrix} & 0 & 0 \end{bmatrix} \begin{bmatrix} q \\ \dot{q} \end{bmatrix} \tag{2.8}$$

2.4.2 Accelerometers

An accelerometer is slightly more difficult to model than a microphone since acceleration is not a state variable. Accelerometers can be placed on any of the structural components in the chamber, and the mass of the accelerometer may significantly affect the dynamic response. For this research, Endevco 2222 accelerometers are used, and their passive effect is modeled in ANSYS as a concentrated mass (1g) at the node closest to the actual location. A complication of the accelerometer output matrices is that a feedthrough term exists (**D**) if the actuator and accelerometer are located on the same component structure. As was the case with the microphone, the accelerometer dynamics are well above the bandwidth of the model, and can be ignored.

Since the state space equations for the system are in modal coordinates, it is more straightforward to derive the accelerometer output matrices in modal coordinates and then transform back to nodal coordinates. The left side of (2.6) includes an expression for $\ddot{q}$ in

terms of the state variables and the applied modal force, u. Equation (2.9) shows the output equation for acceleration in modal coordinates.

$$\ddot{q} = \begin{bmatrix} -\mathbf{M}_r^{-1}\mathbf{K}_r & -\mathbf{M}_r^{-1}\mathbf{C}_r \end{bmatrix} \begin{bmatrix} q \\ \dot{q} \end{bmatrix} + \mathbf{B}u \tag{2.9}$$

The left side of this equation is transformed to nodal coordinates, but the right side is left in terms of modal state variables and forces. This results in a matrix equation with a row corresponding to the acceleration of each nodal DOF as shown in (2.10).

$$\begin{bmatrix} \ddot{u} \\ \ddot{P} \end{bmatrix} = \Phi \begin{bmatrix} -\mathbf{M}_r^{-1}\mathbf{K}_r & -\mathbf{M}_r^{-1}\mathbf{C}_r \end{bmatrix} \begin{bmatrix} q \\ \dot{q} \end{bmatrix} + \Phi\mathbf{B}u = \mathbf{C}_{acc} \begin{bmatrix} q \\ \dot{q} \end{bmatrix} + \mathbf{D}_{acc}\, u \tag{2.10}$$

Only one row of this equation is needed for each accelerometer corresponding to the nodal DOF that the accelerometer senses. This results in a single row for $\mathbf{C}_{acc}$ and a scalar for $\mathbf{D}_{acc}$.

Due to the coupling between the fluid and structure, $\mathbf{C}_{acc}$ includes terms multiplying the modal displacement and velocity states of the component structure, and the modal pressure states of any fluid interfacing with the structure (but not the pressure velocity states). At first it is not intuitive why the acceleration of the structure should be a function of the acoustic modes, but this is physically explained by thinking of the pressure states as a distributed force acting on the structure. Just as a force acting on the plate directly influences its acceleration though the $\mathbf{D}_{acc}$ matrix, forcing the acoustics (either directly or indirectly through a speaker model) will directly influence the acceleration of the plate through the coupling in the $\mathbf{C}_{acc}$ matrix even though $\mathbf{D}_{acc}$ is zero for this pair of actuator and sensor.

2.4.3 Strain Gages

Like an accelerometer, a strain gage does not directly measure a state variable. Strain gages can be bonded to the aluminum plate at any location and direction to provide a measure of the strain at that point on the plate. The addition of strain gages to the plate does

not significantly affect the dynamics of the plate since the gages are light and by design very flexible. Modeling the output characteristics of a strain gage requires an interpolation of the nodal solution so the curvature of the plate can be approximated at any given point and direction.

The bending strain in an elastic material is given by (2.11). [Gere and Timoshenko, 1990] A cubic interpolation matching the nodal solution at the four closest nodes to the strain gage is necessary to evaluate the curvature. The interpolation function is derived from a general bi-cubic polynomial with 16 constants subject to the constraint that it satisfy the steady state Kirchoff plate theory equation (2.12). [Craig, 1981, Strang, 1986]

$$\varepsilon_x = \frac{\partial^2 w}{\partial x^2}\left(\frac{-h}{2}\right) \tag{2.11}$$

$$\nabla^4 w(x, y) = \frac{\partial^4 w}{\partial x^4} + 2\frac{\partial^4 w}{\partial x^2 \partial y^2} + \frac{\partial^4 w}{\partial y^4} = 0 \tag{2.12}$$

$$w(x, y) = c_1 + c_2 x + c_3 x^2 + c_4 x^3 + c_5 y + c_6 y^2 + c_7 y^3 + c_8 xy + c_9 xy^2 + c_{10} xy^3 + c_{11} x^2 y + c_{12} x^3 y \tag{2.13}$$

The resulting bi-cubic interpolation (2.13) has 12 unknown constants which can be expressed as a combination of the state variables by matching the vertical displacement and two slopes at each of the four nodes. Since the state variables are in cylindrical coordinates, the substitutions $x = r\cos\theta$, and $y = r\sin\theta$ must be made which results in the appropriate cubic interpolation (2.14). Figure 2.3 is a sketch of the nodal locations used for the interpolation. The slopes are denoted as rotations about the r and θ coordinates with $R_r = \frac{\partial w}{\partial \theta}$, and $R_\theta = -\frac{\partial w}{\partial r}$. The curvature at a specific point is obtained by differentiating (2.14) twice with respect to the direction of measured strain. This is inserted into (2.11) to produce the strain output matrix in nodal coordinates $\mathbf{C_y}$. A transformation similar to (2.8) is used to transform this output matrix to modal coordinates.

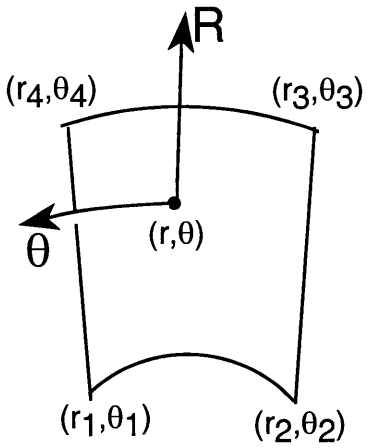

Figure 2.3 Sketch of nodal locations and coordinate directions for bi-cubic interpolation of FEM results.

$$w(r,\theta) = c_1 + c_2 r\cos\theta + c_3 r^2(\cos\theta)^2 + c_4 r^3(\cos\theta)^3 + c_5 r\sin\theta + c_6 r^2(\sin\theta)^2 + c_7 r^3(\sin\theta)^3 + c_8 r^2\cos\theta\sin\theta + c_9 r^3\cos\theta(\sin\theta)^2 + c_{10} r^4\cos\theta(\sin\theta)^3 + c_{11} r^3\sin\theta(\cos\theta)^2 + c_{12} r^4\sin\theta(\cos\theta)^3 \quad (2.14)$$

2.4.4 Speakers

The speakers at the top and bottom of the test chamber are essentially pressure actuators which are used to excite the acoustics in the chamber. The simplest model of the speakers would be to directly drive the pressure DOF's at the speaker location. This approach may be valid for very low frequency excitation; however, the speakers have both mechanical and electrical dynamics within the bandwidth of the model. These dynamics must be captured if the fidelity of the model is to be maintained.

The coupled electro-mechanical model of the speaker is given by (2.15), where the constants are defined in Table 2.2. [Glaese, 1997] The expanded form of (2.15) shows that with an approximation to the mechanical damping, the system can be decoupled into a mechanical model and a disturbance model. This approximation is reasonable since damping is added to the model as a correlation variable to match the input/output charac-

teristics, and not a strictly modeled physical parameter. As described in Section 2.2, the speaker is modeled in ANSYS as a single DOF oscillator, and with the addition of modal damping, the entire mechanical model of the speaker is captured in the modal state space formulation.

$$\begin{bmatrix} \dot{x} \\ \ddot{x} \\ \dot{i} \end{bmatrix} = \begin{bmatrix} 0 & 1 & 0 \\ -\frac{k}{m} & -\frac{c}{m} & \frac{Bl}{mL_e} \\ 0 & -Bl & -\frac{R_e}{L_e} \end{bmatrix} \begin{bmatrix} x \\ \dot{x} \\ i \end{bmatrix} + \begin{bmatrix} 0 \\ 0 \\ V \end{bmatrix} \Rightarrow m\ddot{x} + \left(c + \frac{Bl^2}{sL_e + R_e} \right) \dot{x} + kx = \frac{Bl}{sL_e + R_e} V \qquad (2.15)$$

TABLE 2.2 Physical parameters of speaker

Parameter	Value
Mass (m)	33.2 g
Stiffness (k)	3.83 x 10^4 N/m
Damping (c)	7.32 Ns/m
Electrical Resistance (R_e)	11.9 Ω
Electrical Inductance (L_e)	2.25 x 10^{-3} H
Electro-mechanical Coupling (Bl)	9.83 N/A

The right side of (2.15) forms the speaker disturbance model which describes how a drive voltage, V, results in a modal force actuation of the speaker. This is inserted into the "Actuator Dynamics" block of Figure 2.2, and augmented to the mechanical dynamics when calculating the input/output response due to excitation of the speaker. The remaining part of the speaker model involves determining the input matrix (**B**) for the speaker. This follows a similar formulation to that of **C** for the sensors.

Since only one mechanical mode of each speaker is retained in the modal state space model, the forcing vector for the speaker in nodal coordinates is somewhat arbitrary as long as it results in excitation of this mode. A single force acting at the center node of the speaker in the positive z-direction for the bottom speaker and negative z-direction for the top speaker is used. This results in a single non-zero entry in the nodal forcing vector for

each speaker. This forcing vector is transformed to modal coordinates as shown in (2.16) The scalar k represents the gain of the amplifier used to drive the speaker.

$$\mathbf{B}_{sp} = k\mathbf{M}_r^{-1}\Phi^T \begin{bmatrix} 0 \\ 1 \\ 0 \\ \mathbf{0} \end{bmatrix} = k\mathbf{M}_r^{-1} \begin{bmatrix} & 0 \\ \phi_{sp}^T & 1 \\ & 0 \\ \mathbf{0} & \end{bmatrix} \tag{2.16}$$

2.4.5 Piezoelectric Sensors and Actuators

Piezoelectric materials bonded to a structure are commonly used as both actuators and sensors for structural and acoustic control. These actuators and sensors are naturally distributed, and can be placed on the structure or shaped to provide favorable modal observability and controllability. For this research, PZT wafers are used as structural actuators and/or sensors, and PVDF film is used as a modally shaped sensor. The modeling of both relies on the ability to characterize the electro-mechanical behavior of the material in terms of forces or displacements around its contour.

PZT Actuator

A 2.5" x 1.5" x 0.01" PZT wafer bonded to the aluminum plate is used as the structural control actuator. The wafer adds considerable mass and stiffness to the plate, and is modeled in ANSYS by altering the density and modulus of the shell elements in the vicinity of the wafer. The added stiffness contribution is calculated using laminated plate theory considering the plate and wafer as separate laminates. Since the wafer is rectangular and the finite element mesh is circular, the added mass and stiffness is approximated over a 1.5" diameter circle at the center of the plate.

A method developed by Griffin and Henderson was used which treats the actuation of the PZT as the blocked force acting against the finite element model of the plate and wafer. This force results in a distributed moment around the edge of the wafer, as shown in Figure 2.4, due to the offset of the wafer from the neutral axis of the plate. The modeling

method has been validated with experimental data for aluminum plates 0.018in to 0.125in thick. [Griffin & Henderson, 1997]

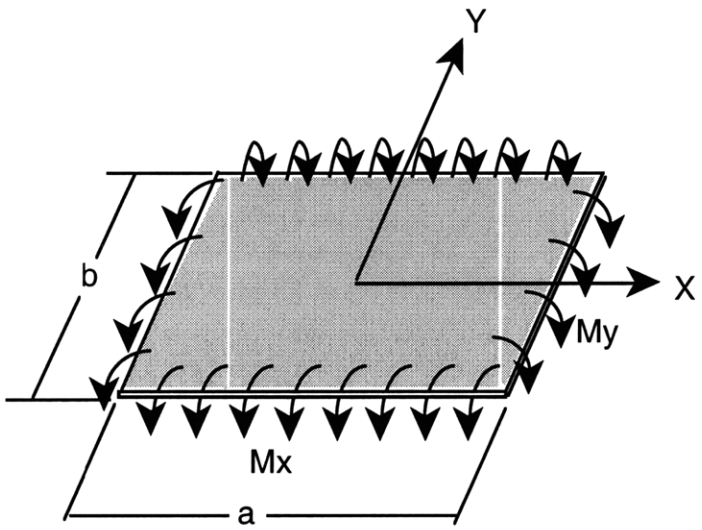

Figure 2.4 Edge moment actuation of PZT wafer.

The equations of motion for the plate with PZT actuator are given in (2.17). The left side of this equation comes from Kirchoff plate theory, and is captured by the finite element model. The terms on the right side are distributed forces applied by the piezoelectric material and reduce to distributed moments along the edge of the PZT when integrated over the area using the finite element shape functions. These distributed moments are given in (2.18) with the variables described in Table 2.3.

$$\frac{Eh^3}{3(1-\upsilon)}\nabla^4 w + m'\ddot{w} = -\frac{\partial^2 M_{x(pe)}}{\partial y^2} - \frac{\partial^2 M_{y(pe)}}{\partial x^2} \tag{2.17}$$

$$M_x = \frac{E_{pe}}{1-\upsilon_{pe}} d_{31} \frac{a}{n}\left(\frac{t_{pe}+h}{2}\right)$$
$$M_y = \frac{E_{pe}}{1-\upsilon_{pe}} d_{31} \frac{b}{n}\left(\frac{t_{pe}+h}{2}\right) \tag{2.18}$$

TABLE 2.3 Constants used for modeling PZT wafer on aluminum plate

Piezoelectric Modeling Variable	Value
Piezo Elastic Modulus (E_{pe})	8.833×10^6 psi
Piezo Poisson's Ratio (υ_{pe})	0.35
Transverse Piezo Strain Constant (d_{31})	6.7333×10^{-9} in/V
Piezo Thickness (t_{pe})	0.01 in.
Plate Thickness (h)	0.032 in.
Edge Length of Distributed Moment (a,b)	a = 2.5 in. b = 1.5 in.
Discretization Points Along Edge (n)	10

The cubic interpolation function developed in Section 2.4.3 is used to apply this distributed moment at 10 discrete points along each edge of the wafer. Since the finite element model is in cylindrical coordinates, and the applied moments are described in Cartesian coordinates, an additional coordinate transformation (2.19) is necessary. This produces a forcing vector in nodal coordinates that is a function of the displacement states of several nodes near the edge of the wafer. The transformation to modal coordinates and addition of the scalar gain for the amplifier completes the input model for the PZT actuator.

$$\begin{bmatrix} \frac{\partial w}{\partial x} \\ \frac{\partial w}{\partial y} \end{bmatrix} = \begin{bmatrix} \cos\theta & -\frac{1}{r}\sin\theta \\ \sin\theta & \frac{1}{r}\cos\theta \end{bmatrix} \begin{bmatrix} \frac{\partial w}{\partial r} \\ \frac{\partial w}{\partial \theta} \end{bmatrix} \tag{2.19}$$

PVDF Sensor

Two circularly shaped PVDF sensors are used to provide high modal observability of the first and second symmetric plate modes while filtering the response of the asymmetric modes. PVDF film is extremely thin, and does not affect the dynamics of the plate. An analog charge amplifier circuit is used to produce an output voltage proportional to the charge on the PVDF electrode, which is in turn proportional to the area integral of strain.

The signal voltage of PVDF bonded to a plate is the area integral of the strain multiplied by the transverse piezoelectric strain constant (2.20). It is seen that for a circular sensor, the contribution of the second integral is zero, and the signal reduces to the integral of $\frac{\partial w}{\partial r}$ around the contour of the sensor. This integral is approximated as a summation of 100 discrete points along the contour, and the interpolation function of Section 2.4.3 is used to relate this summation to the state displacement variables of the nodes near the contour. This results in a sensor matrix in nodal coordinates that is transformed to modal coordinates in the same manner as (2.8).

$$
\begin{aligned}
y &= d_{31}\frac{t}{2}\int_0^{2\pi R}\int_0 \frac{\partial^2}{\partial r^2}w(r,\theta)\partial r\partial\theta + d_{31}\frac{t}{2}\int_0^{R}\int_0^{2\pi} \frac{\partial^2}{\partial\theta^2}w(r,\theta)\partial\theta\partial r \\
&= d_{31}\frac{t}{2}\int_0^{2\pi} \frac{\partial}{\partial r}w(R,\theta)\partial\theta + d_{31}\frac{t}{2}\int_0^{R} \frac{\partial}{\partial\theta}w(r,2\pi) - \frac{\partial}{\partial\theta}w(r,0)\partial r \\
&\cong d_{31}\frac{t}{2}\sum_{i=1}^{n} \frac{\partial}{\partial r}w(R,\theta_i)\frac{2\pi R}{n}
\end{aligned}
\tag{2.20}
$$

The same modeling approach is used for a PZT wafer acting as a distributed sensor. For this case, the integral in (2.20) is carried out in Cartesian coordinates over the area of the wafer, and reduces to a summation of line integrals over each edge. Again, the interpolation function is used to discretize this integral, and the two coordinate transformations are applied to transform to cylindrical and modal coordinates.

2.5 Open-Loop Model Correlation

Open-loop correlation of the finite element model is accomplished by comparing transfer functions from the control and disturbance actuators to the feedback and performance sensors. With few exceptions, this comparison shows that the finite element model captures the coupled dynamics of the chamber. Table 2.4 summarizes this correlation by comparing the frequency of the uncoupled and coupled component modes. This shows that the model captures the significant stiffening of the first plate mode and two speaker modes, as well as the de-stiffening of the first lower chamber acoustic mode.

TABLE 2.4 Open loop correlation between finite element model and data

		Uncoupled Model	Uncoupled Data	Coupled Model	Coupled Data
Plate					
(symmetric)	**Mode 1**	71.9 Hz	71.2 Hz	79.9 Hz	85.3 Hz
	Mode 2	297.8 Hz	299.4 Hz	298.2 Hz	290.9 Hz
	Mode 3	703.8 Hz	681.3 Hz	714.3 Hz	675.8 Hz
Speakers					
	Top	143.0 Hz	144.4Hz	166.0 Hz	156.9 Hz
	Bottom	170.0 Hz	170.9 Hz	199.7 Hz	198.0 Hz
Lower Chamber					
Acoustics	**Mode 1**	166.4 Hz	166.3 Hz	140.3 Hz	134.0 Hz
	Mode 2	334.1 Hz	333.0 Hz	347.9 Hz	333.7 Hz
	Mode 3	504.7 Hz	498.8 Hz	510.0 Hz	492.3 Hz

2.5.1 Control to Feedback Transfer Functions

Figure 2.5 shows overlay plots of transfer functions from the piezo wafer at the center of the plate to the three sensors used for feedback. These transfer functions, along with the compensator, form the loop transfer function which governs the closed-loop stability of the system. Each of these plots show that the model captures the zeros and phase of the input/output response reasonably well.

2.5.2 Disturbance to Feedback Transfer Functions

Figure 2.6 shows overlay plots of transfer functions from the top speaker to the three sensors used for feedback. One of the errors in the finite element model is present in this figure. Each of the data transfer functions lose phase faster than is predicted in the model. This phase loss resembles an acoustic propagation delay of 11 in. between the top speaker and plate. It is not clear why the finite element model would not capture this delay in the upper chamber when it is captured in the lower chamber. A more likely cause for the phase loss is unmodeled speaker dynamics. Due to the complex geometry, material prop-

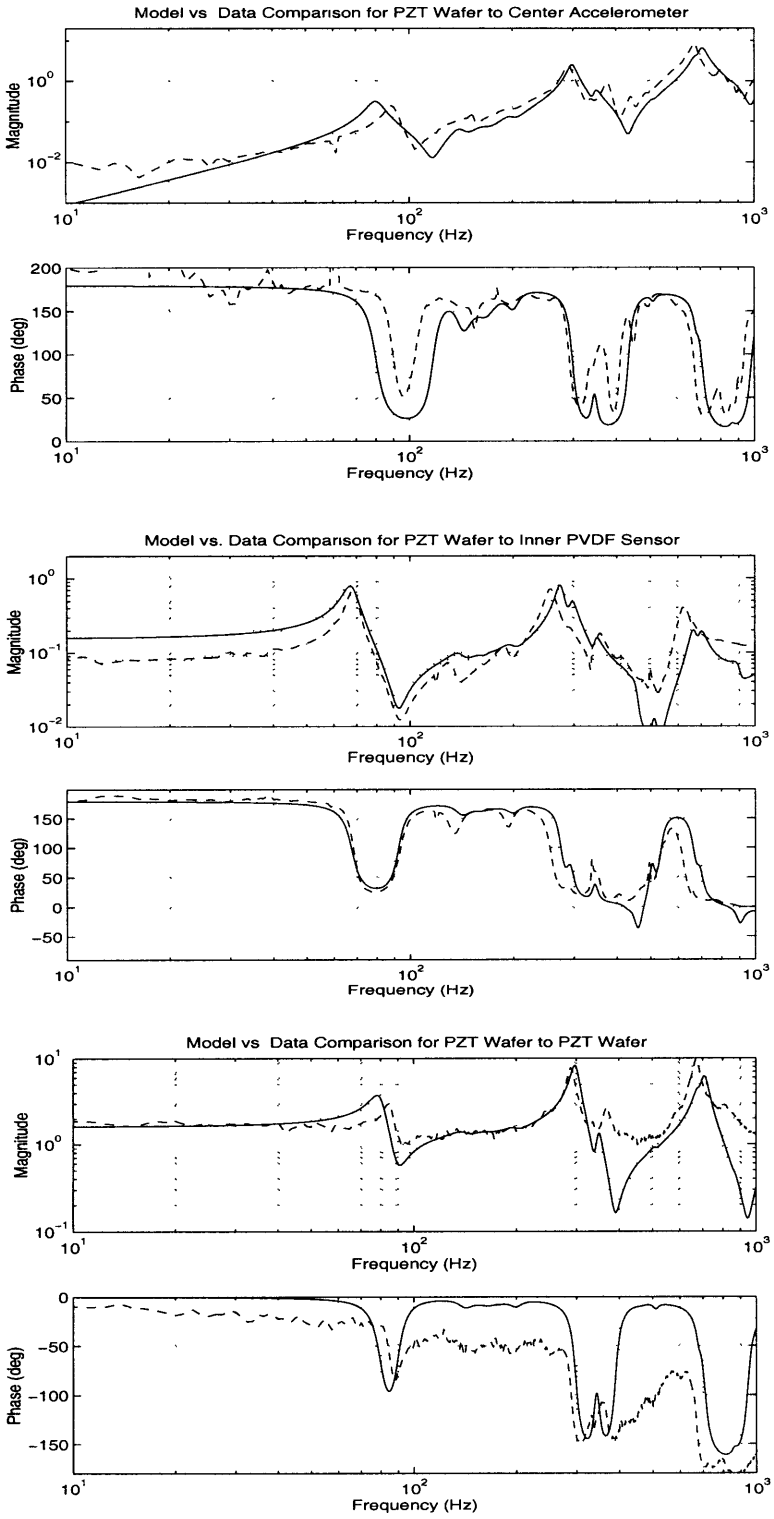

Figure 2.5 Finite element model to data correlation transfer functions for control input to various feedback sensors.

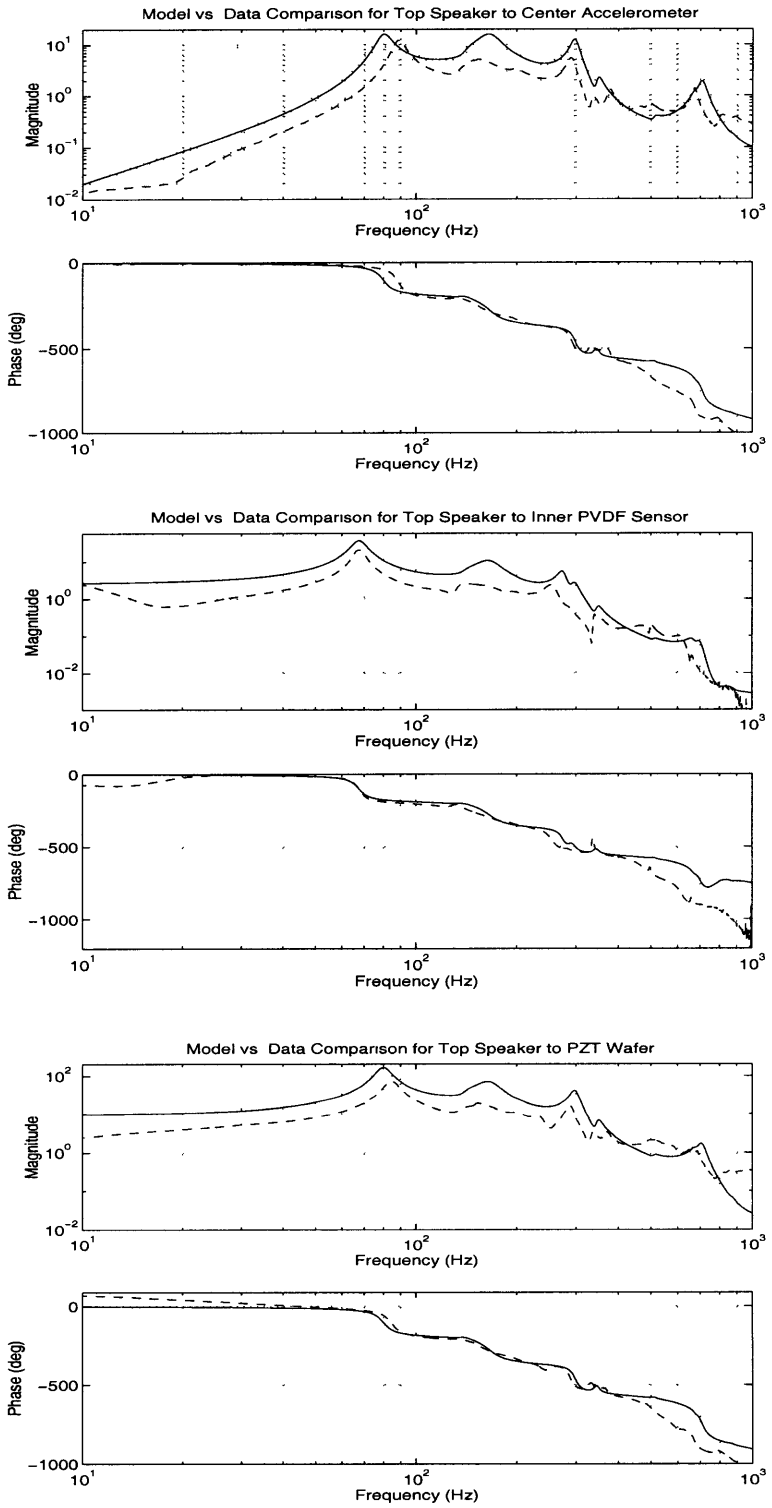

Figure 2.6 Finite element model to data correlation transfer functions for disturbance input to various feedback sensors.

erties and boundary conditions of the speaker cone, modeling these flexible modes is very difficult.

Regardless of the cause, phase loss in the disturbance to performance transfer function does not affect the stability of a compensator. Furthermore, accurate modeling of the disturbance to feedback sensor transfer function is only important in the frequency region where performance is desired. [Crawley, Campbell & Hall, 2000] The phase of the data begins to deviate from the model above 500 Hz, and the expected control frequency band is between 70 Hz - 300 Hz. For these reasons, phase loss in these transfer functions, especially above the expected control bandwidth, should not affect the ability of the model to predict achievable closed loop performance.

2.5.3 Control to Performance Transfer Functions

Figure 2.7 shows overlay plots of transfer functions from the PZT wafer to the three microphones in the lower chamber. In general, the model captures the zeros and phase very well. One obvious difference is the location of the first zero in the microphone 3 transfer function. The data shows that this zero occurs at a slightly lower frequency than the first plate mode. The model predicts that the zero should appear at a slightly higher frequency. Figure A.7 in Appendix A shows that the acoustic pressure at this microphone position is close to zero for the coupled modeshape. This accounts for the close spacing of the zero to the pole. The fact that the sign of the residue is changed between the model and data could indicate that using the uncoupled modeshapes as a basis for the model is not accurate enough for this transfer function. Since all three of these transfer functions are used together to evaluate the distributed performance in the lower chamber, this error is averaged and not as prevalent. The error in this transfer function would be significant if this microphone is used as a feedback sensor.

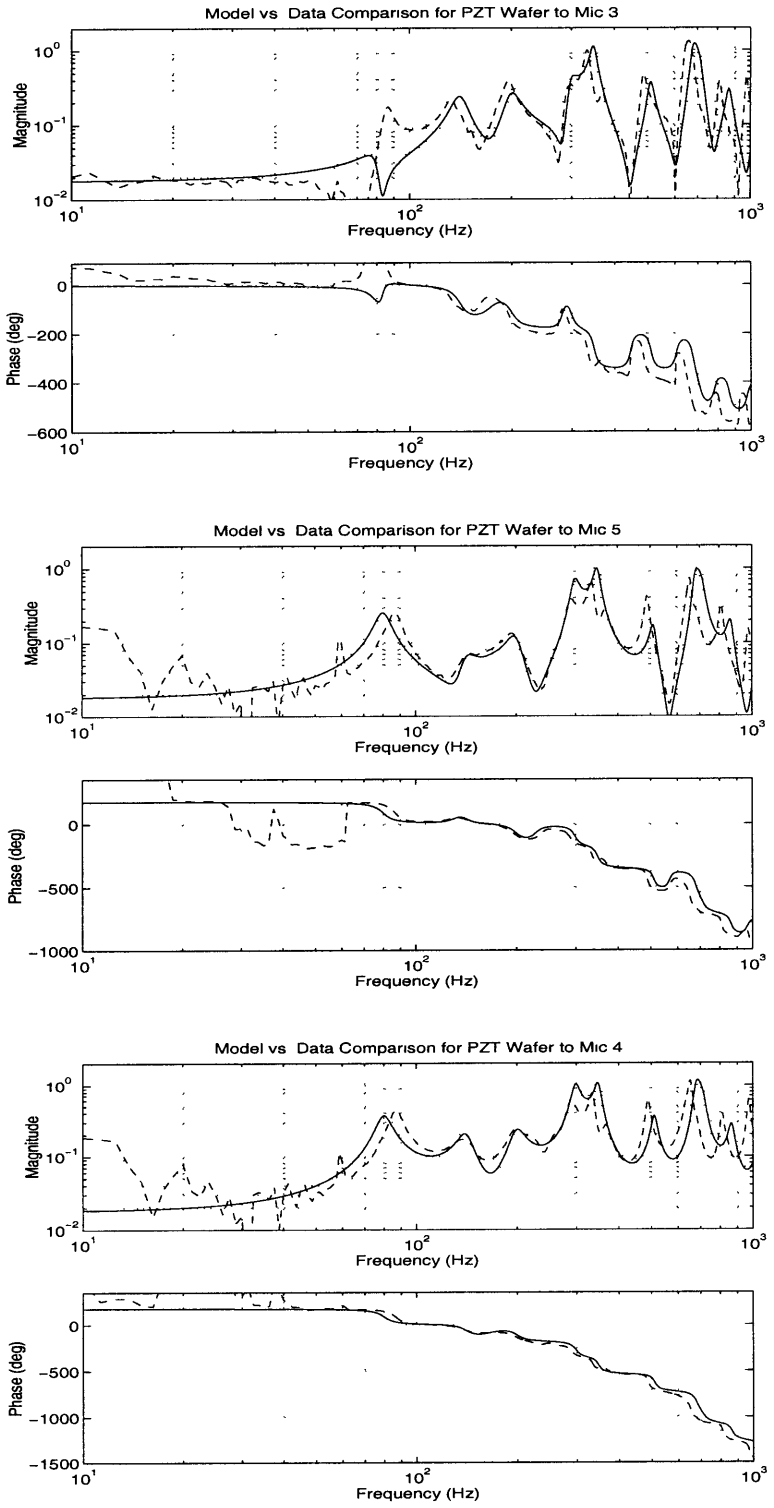

Figure 2.7 Finite element model to data correlation transfer functions for control input to performance microphones.

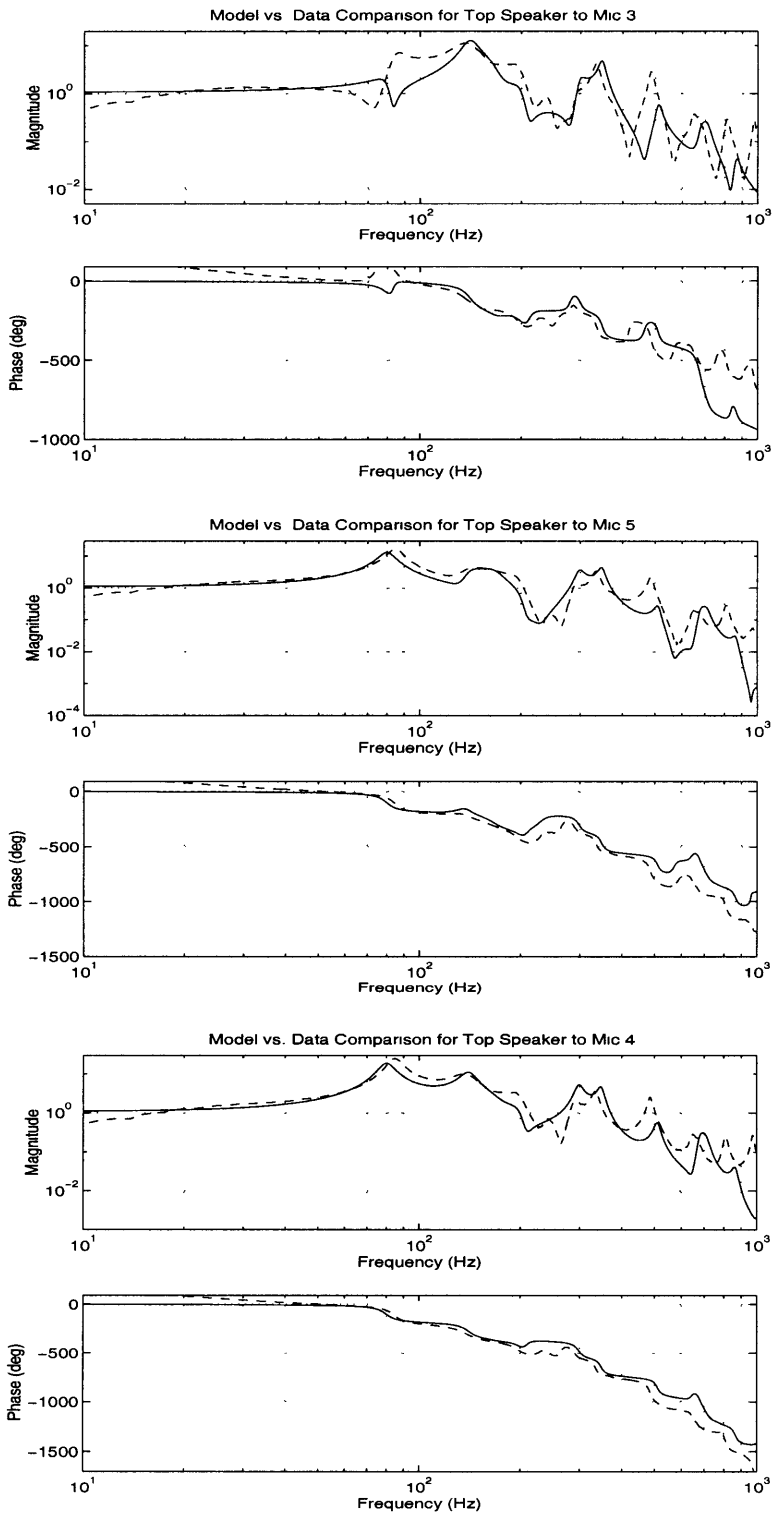

Figure 2.8 Finite element model to data correlation transfer functions for disturbance input to performance microphones.

2.5.4 Disturbance to Performance Transfer Functions

Figure 2.8 shows overlay plots of transfer functions from the top speaker to the three microphones in the lower chamber. Both of the errors previously discussed are apparent in these transfer functions. For the same reasons given previously, these errors are not critical to predicting closed loop performance.

2.6 Summary

This chapter described the development of a high fidelity finite element model of the acoustic test chamber. Assumptions regarding the modal basis and modeling of sensor and actuator dynamics were validated through comparison of the finite element model transfer functions to data. In subsequent chapters, the capabilities and limitations of this finite element model for sensor/actuator design, and prediction of closed-loop performance will be investigated.

Chapter 3

SENSOR AND ACTUATOR DESIGN

The previous chapter described the development of the finite element model of the acoustic chamber. In this chapter, the use of this model for the design of shaped and distributed sensors and actuators is investigated. Since model development occurred somewhat in parallel with experimental implementation, the sensor and actuator designs used information from the model at various stages of completion. This, along with unmodeled manufacturing and boundary condition factors, limit the ability of the model to predict sensor and actuator performance.

The design method for shaped and distributed piezoelectric sensors and actuators follows from the forcing (2.18) and sensing equations (2.20) in Chapter 2. Two types of distributed sensors and actuators are used in this research for acoustic transmission control. The first is a modally shaped strain sensor made from polyvinylidene fluoride (PVDF) film. The second is a simultaneous sensor and actuator (sensuator) made from PZT wafers. The basic goal of both designs is to provide high observability of the modes targeted for active control while maintaining minimal phase loss over the expected controller bandwidth.

3.1 Modally Shaped PVDF Sensor

PVDF film is a very thin, light piezoelectric polymer which can be easily cut into a spatially filtering structural sensor. Carl Blaurock of Mide Technology Corporation in Cambridge designed two shaped PVDF sensors for this research using modeshape information

from the finite element model of the aluminum plate. One of these sensors was used by Asari to implement high performance acoustic transmission control in the test chamber. [Asari, 1998] The design process for this sensor will be briefly discussed here as the basis for the design of other shaped and distributed piezoelectric actuators and sensors. The limitations of this PVDF sensor will also be explained so they can hopefully be avoided (or at least anticipated) in future designs.

3.1.1 Modal Observability and Rolloff

Figure 3.1 shows the slope $\left(\frac{\partial w}{\partial r}\right)$ node lines of the second and third symmetric plate modes. At the time of the design of the shaped PVDF sensor, the first two symmetric modes of the plate had been identified from the disturbance to performance transfer functions as the primary contributors to acoustic transmission. The design goal of the sensor was to provide high modal observability of these two modes, while filtering the response of the third symmetric and all asymmetric modes to allow rolloff of the compensator. As shown in (2.20), using a circular sensor will automatically filter the asymmetric modes since the integral of $\frac{\partial w}{\partial r}$ around a circular contour will be zero for these modes. Likewise, if the third symmetric mode is to be filtered, the edge of the sensor must be placed close to a slope node line of this mode. [Blaurock,1998]

Figure 3.1 reveals that a 2.0 in. radius circular sensor will have its edges close to the slope node line of the third symmetric plate mode. It is also away from the slope node line of the second symmetric mode to provide good observability of this mode. This sensor should meet all of the design goals.

3.1.2 Sensitivity to Predicted Modeshape

Figure 3.2 shows the actual and predicted transfer functions from the piezo wafer in the center of the plate to the modally shaped PVDF sensor. The high observability of the first and second symmetric modes is achieved; however, the third symmetric mode is also highly observable. The primary reason for the difference between the expected and actual

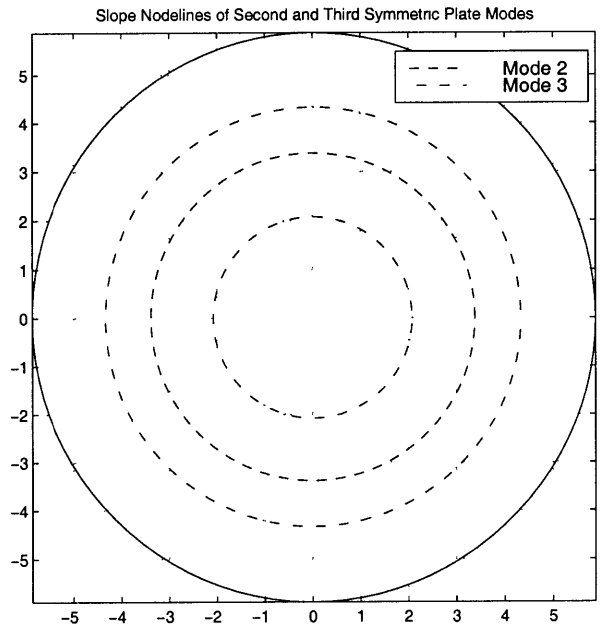

Figure 3.1 Slope nodelines of the second and third symmetric plate modes used for design of a modally shaped PVDF strain sensor.

response of the sensor is a mild unmodeled warp of the aluminum plate. When this plate is clamped around its edges, the warp results in a residual in-plane compression which significantly reduces its transverse stiffness. This destiffening was experimentally quantified by comparing the frequencies of the first symmetric mode of the warped and unwarped plates outside the acoustic chamber. The frequency of the unwarped plate is 71 Hz, while the frequency of the warped plate is 56 Hz. At the time of the sensor design, the finite element model did not include this warp effect, thus the node lines of Figure 3.1 are not accurate enough to achieve the desired filtering for the third symmetric mode.

3.2 Piezoelectric Sensuator Design

A piezoelectric sensuator is a device which simultaneously actuates and senses the vibration of a structure. This is accomplished by using an analog circuit to subtract the charge on a piezo due to the drive voltage from the total charge. The remaining charge is proportional to the strain or force in the piezo (depending on the relative stiffness of the structure

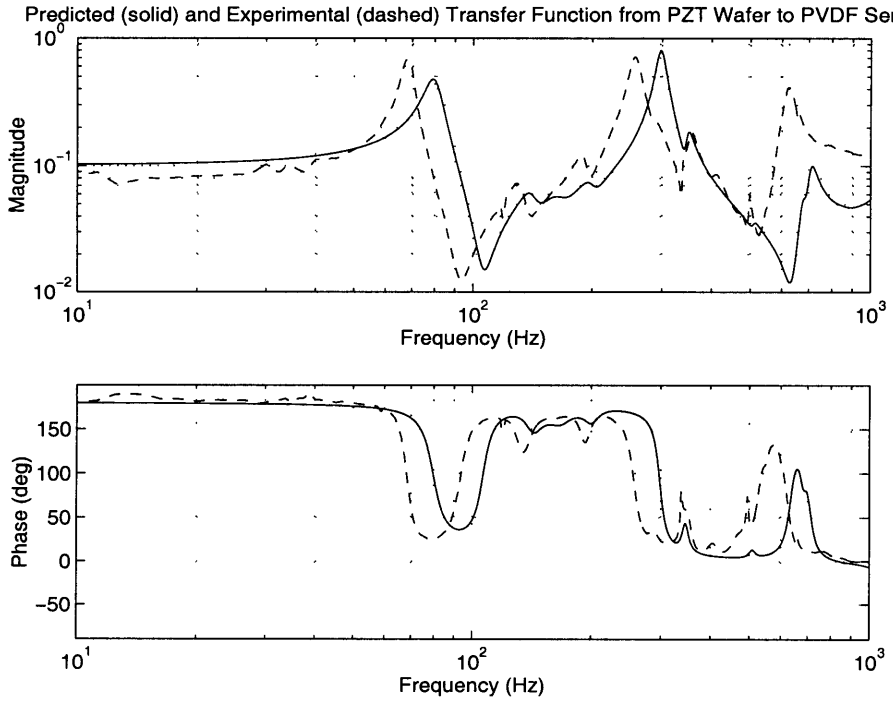

Figure 3.2 Comparison of predicted and experimental transfer function from PZT wafer to modally shaped PVDF strain sensor.

to which it is bonded). The approach is particularly attractive for acoustic transmission control since the resulting actuator-to-sensor transfer function is perfectly collocated, and ideally has bounded phase to infinite frequency.

Previous work in this area used terms such as "simultaneous sensing and actuation" [Spangler, 1994, Anderson & Hagood, 1994] or "self-sensing actuator" [van Schoor, Lengyel & Spangler, 1996, Ko & Tongue, 1995] to describe what will be referred to in this thesis as a sensuator. Parts of the previous work have focused on reducing phase nonlinearity [Spangler, 1994] or amplitude nonlinearity [van Schoor, Lengyel & Spangler, 1996] in the simple analog circuit. For this research, the simple analog circuit shown in Figure 3.3 is used to implement a PZT sensuator for acoustic transmission control.

In the circuit above, C_{sp} and C_{sr} are ideally equal capacitors which act as charge sensors to provide voltages V_p and V_R proportional to the charge on the piezo element and reference capacitor. The drive voltage across the piezo is thus V_I - V_p. Assuming the piezo acts elec-

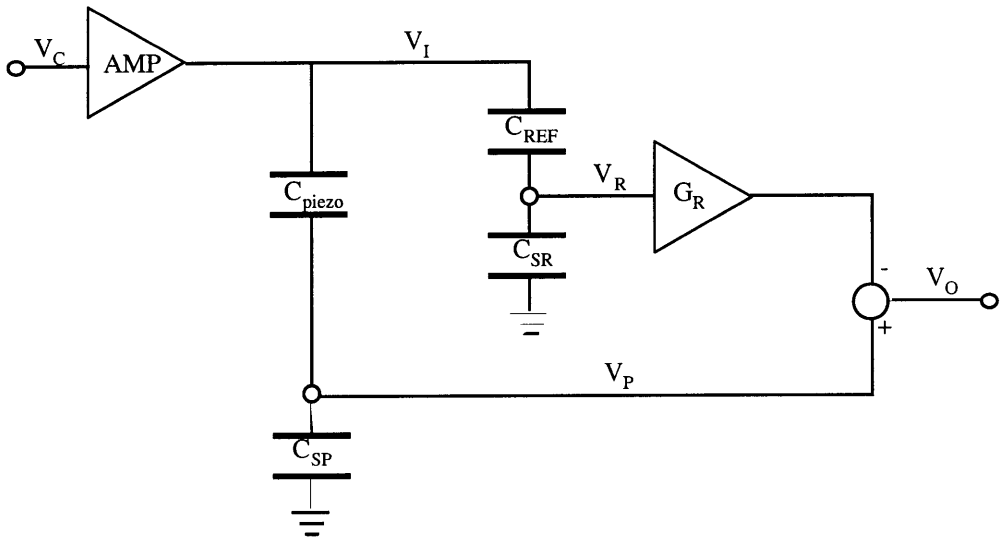

Figure 3.3 Simple piezoelectric sensuator circuit for simultaneous actuation and sensing of structural vibration.

trically as an ideal capacitor, the voltages V_R and V_p are given in (3.1) where K is the stiffness of the piezo and structure, G_{33} is a piezoelectric coefficient composed of the charge coefficient and geometry, C_2 is the output influence coefficient for the piezo, C_{piez} is the blocked capacitance of the piezo, and q is the dynamic state vector. If $C_{REF} = C_{piez}$, then differencing the two voltages will result in an output voltage proportional to the dynamic state vector, q. A tuning gain, G_R, is included in the circuit to reduce the effect of the capacitors not being exactly equal. An additional tuning gain could be placed in the piezo leg of the circuit, but this would be redundant for a single piezo element. It will be shown in the following sections that the circuit tuning gain can greatly affect the frequency of the zeros in the sensuator transfer function.

$$V_p = KG_{33}\frac{C_{piez}}{C_{sp}+C_{piez}}C_2 q + \frac{C_{piez}}{C_{sp}+C_{piez}}V_I \tag{3.1}$$

$$V_R = \frac{C_{REF}}{C_{sr}+C_{REF}}V_I$$

3.2.1 Single Wafer PZT Sensuator on Plate

The first attempt at a sensuator for transmission control used the same PZT wafer originally used only as an actuator. This was chosen since it was already proven to have good actuation authority over the symmetric plate modes of interest. Since the strain sensor matrix for this wafer is simply the transpose of the distributed force actuation matrix, it was predicted that the sensuator should also provide good observability of these same modes.

The simple sensuator circuit shown in Figure 3.3 was built on a small protoboard. A detailed schematic of this circuit is shown in Figure 3.4, and a photograph of the circuit on the protoboard is shown in Figure 3.5. In addition to the reference capacitor and charge sensor capacitors, the actual circuit contains conditioning elements such as voltage buffers and a final high-pass filter. The piezo wafer capacitance is 136ηF, and the reference capacitor is 134.3ηF. C_{sp} and C_{sr} were chosen to be 985ηF and 960ηF respectively, which makes V_p and V_R approximately 0.10 V_I.

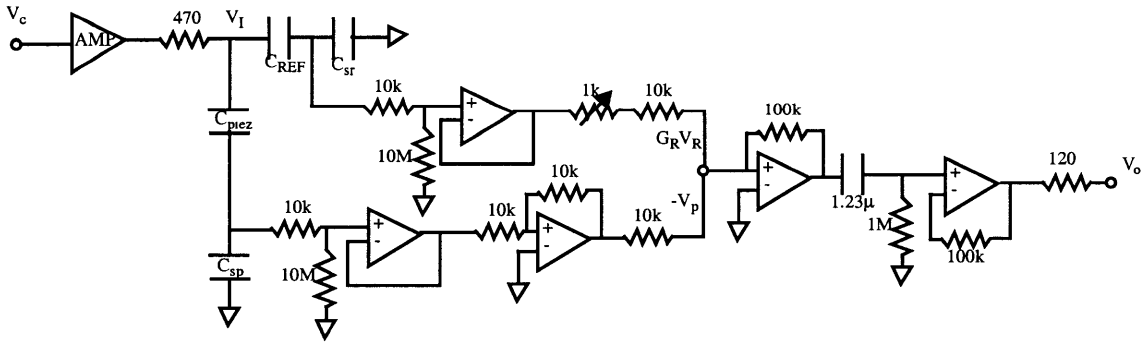

Figure 3.4 Detailed schematic of single wafer PZT sensuator circuit.

Tuning the circuit is accomplished by varying the 1kΩ trimpot resistor on the reference leg. The nominal tuning for the circuit is to set such that V_R is exactly equal to the second term of V_p in (3.1). This tuning closely corresponds to sensing distributed strain over the area of the wafer. Other tunings correspond to mixing a feedthrough term proportional to the actuated distributed force into the sensor signal. This causes a migration of the trans-

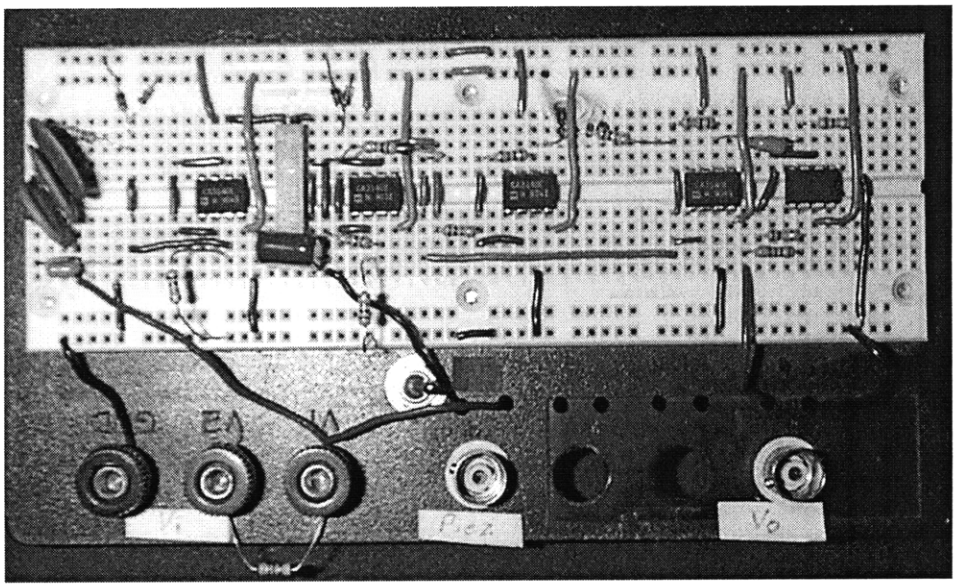

Figure 3.5 Photograph of single PZT sensuator circuit on protoboard.

fer function zeros between the poles, and also leads to a range where the system is non-minimum phase. Finally, for the minimum phase tunings the output can either be differentiated or integrated with a negative unit gain (depending on the tuning) to yield a positive real transfer function. All of these characteristics of the sensuator tuning will be discussed in the following subsections with emphasis to their effect on closed-loop control design.

Pole/Zero Separation

Separation of the zeros from the targeted poles in the control input to feedback output transfer function determines the observability of the system modes, and governs the achievable performance of a feedback compensator. As stated above, adjusting the reference leg gain in the sensuator has the effect of mixing a signal proportional to the applied distributed force into the output signal. This causes a migration of the zeros, which has been documented in previous sensuator work, [Spangler, 1994] and in work where separate strain and force sensors were mixed to achieve favorable input/output transfer functions for control design. [Makarenko & Crawley, 1998]

The mixing of strain and applied force by the sensuator circuit can be better understood by considering a simple model of the sensuator output. The sensuator input matrix, **B**, is identical to that for the piezo wafer acting as an actuator, but has a slightly smaller gain since part of the voltage drop across the piezo is used to extract the strain signal. The sensuator strain matrix, $\mathbf{C}_{\mathbf{strain}}$, is determined by integrating the curvature over the area of the wafer as described in Section 2.4.5. Finally, a feedthrough term proportional to the applied moment, **D**, is added using the sensuator tuning parameter k as given in (3.2). For this research, the value of **D** was determined experimentally by disconnecting the reference leg of the sensuator circuit, and measuring the amplitude of the mostly non-dynamic transfer function.

$$y = \mathbf{C}_{\mathbf{strain}}\, x + (1-k)\mathbf{D}u \tag{3.2}$$

For $k \ll 1$ the output is dominated by the feedthrough term. The structural dynamics of the plate are not observable since the zeros migrate to cancel the poles. The same is true for $k \gg 1$, except the phase is $180°$ for this tuning. For $k = 1$ the feedthrough term is canceled, and the strain signal from the piezo is recovered. For tunings $1 \le k \le 1.2$, the frequency of zeros of the sensuator transfer function quickly increase until they are just below the next higher pole in the system. Figure 3.6 shows transfer functions for this zero migration from both the finite element model and experimental data for three tuning cases in this region. The third graph on each plot is a step response of the system with the input shown as the dashed line. This step response shows that tuning case 3 for the sensuator is nonminimum phase.

Nonminimum Phase

Figure 3.7 shows the zero migration vs. tuning gain in the complex plane near the first two poles of the system. The values for this figure (shown as separate zero markers) were taken from the finite element model using five values of the tuning parameter, k. The values of k used are 1, 1.025, 1.065 1.085 and 1.175 corresponding to tuning cases 1 through 5, respectively. The migration pattern shows that the highest frequency zero pair, which

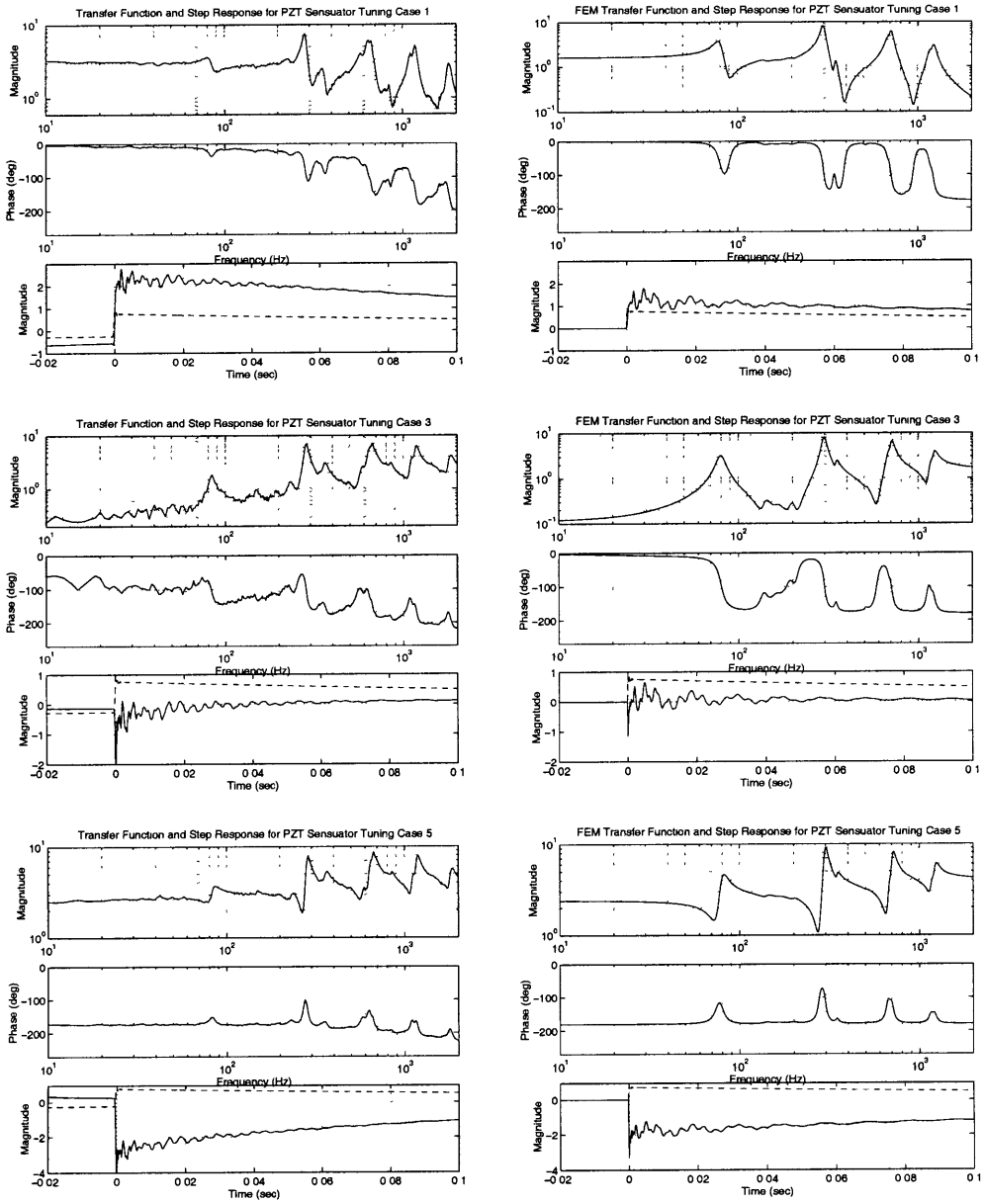

Figure 3.6 Experimental and finite element model single PZT sensuator transfer functions for various circuit tunings.

occurs at $\pm j\infty$ in the absence of a feedthrough term, migrates to become a pair of real zeros as k is increased above 1. This migration pattern is consistent with the mathematical concept of the extended complex plane, where points receding from the origin infinitely far in any direction converge to a single "point at infinity". [Hildebrand, 1976] As k is

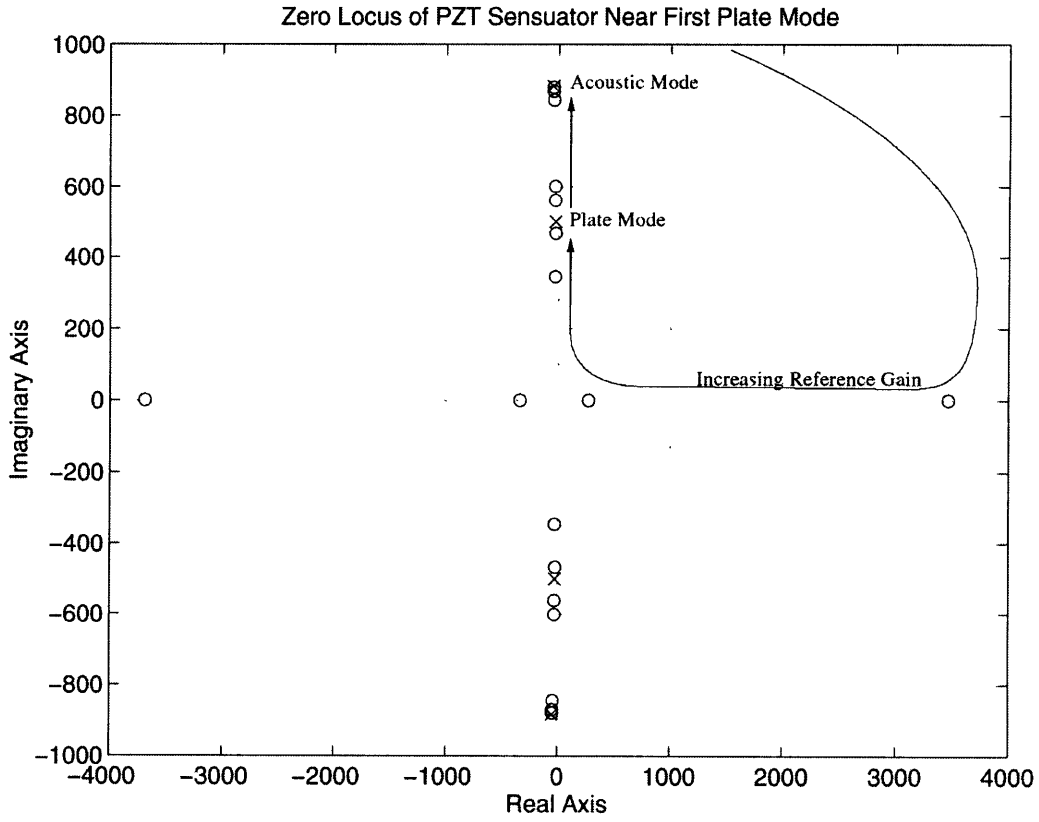

Figure 3.7 Zero locus of single wafer PZT sensuator near first plate mode.

increased further, the real zeros meet at the origin, and asymptote to a complex pair just below the frequency of the first system poles.

A question that arises from this figure is whether the real zeros are actually present in the system, or a product of the discretization and truncation of the finite element model. To address this question, an infinite order wave model of a compression rod fixed at one end and subjected to a force at the other end was created. Since strain is proportional to force for a rod, the output analyzed is a mixture of displacement at the forced end with a feedthrough of the applied force. The equation for this output is given in (3.3). Values of $E = 1.0\frac{N}{m^2}$, $\rho = 1.0\frac{kg}{m^3}$, $A = 0.1m^2$, and $L = 1.0m$ were used.

$$\frac{out}{F} = \frac{1 - e^{\frac{-2\varsigma sL}{jc_0\pi}} e^{\frac{-2sL}{c_0}} + (1-k)EA\left(\frac{\varsigma s}{jc_0} - \frac{s}{c_0}\right)\left(e^{\frac{-2\varsigma sL}{jc_0\pi}} e^{\frac{-2sL}{c_0}} + 1\right)}{EA\left(\frac{\varsigma s}{jc_0} - \frac{s}{c_0}\right)\left(e^{\frac{-2\varsigma sL}{jc_0\pi}} e^{\frac{-2sL}{c_0}} + 1\right)} \tag{3.3}$$

$$\lambda_n = \left.\frac{(2n-1)\pi c_0}{2L}\right|_{n = 1, 2\ldots}$$

The zero migration for this equation is qualitatively similar to the single PZT wafer on a plate. This equation was solved numerically to determine if transmission zeros exist for any real values of s. For values of the mixing parameter $0 > 1 - k > \frac{-c_0}{EA}$ a pair of real zeros move toward the origin from $\pm\infty$. Table 3.1 gives the migration of zeros near the first two system poles. This model proves that the presence of real zeros is inherent to the physics for a range of negative mixing ratios of the applied force with a displacement type sensor.

TABLE 3.1 Numerical solution of zero migration in infinite order model as function of sensuator tuning parameter

Mixing Parameter (k)	Real Zeros	Zeros Between 1st & 2nd Pole
1.005	±2003.0 rad/s	±3.142j rad/s
1.05	±199.380 rad/s	±3.154j rad/s
1.5	±19.938 rad/s	±3.303j rad/s
3	±5.001 rad/s	±3.793j rad/s
10	±0.582 rad/s	±4.467j rad/s
10.9	±0.175 rad/s	±4.488j rad/s
11	0 rad/s	±4.498j rad/s
11.1	±0.172j rad/s	±4.498j rad/s
12	±0.517j rad/s	±4.498j rad/s
20	±1.136j rad/s	±4.498j rad/s

The presence of a nonminimum phase zero in the loop transfer function introduces a conservation trade-off in the sensitivity transfer function. The closer the nonminimum phase zero is to the frequency range where performance is desired (sensitivity transfer function < 1), the more the sensitivity transfer function will exceed 1 in other ranges. [Freudenberg & Looze, 1985] This results in disturbance amplification and increased sensitivity to model errors. Historically, control design has focused on performance over a bandwidth from DC to some rolloff frequency. A nonminimum phase zero effectively limits the bandwidth of this type of control to frequencies well below the nonminimum phase zero. For flexible structural control, performance, noise rejection, and robustness can all be achieved with a nonminimum phase zero on either side of the performance bandwidth. The trade-off then becomes higher sensitivity below the control frequency band. This may be acceptable if the system is well modeled at low frequency.

Positive Real

For a structural transfer function to be positive real, the input and output must be collocated and their product must be power. The phase of the transfer function will then be bounded between $\pm 90°$. There is an equivalence between systems which produce positive real transfer functions, and hyperstable systems. [Anderson, 1968] This leads to the very useful result that the negative feedback connection of two positive real systems is always stable. Thus, if a transfer function G_{yu} is positive real, any positive real feedback compensator (e.g. a simple proportional gain) is guaranteed not to cause closed-loop instability.

For the nominal tuning of $k = 1$, the sensuator transfer function has an input which is distributed force over the area of the PZT wafer (resolved as a line moment around the edge of the wafer), and output which is distributed strain (resolved as the integral of the slope around the edge of the wafer). The product of the input and output is work, not power; however, if the output were differentiated to give strain rate, the resulting transfer function would be positive real. It has also been determined that for the other minimum phase tuning of the sensuator ($k > 1.085$), the system can be made positive real by integrating the output and multiplying by -1. [Spangler, 1994] None of the nonminimum phase tunings

can produce a positive real transfer function. Figure 3.8 shows the two cases for positive real G_{yu} from the finite element model of the single wafer sensuator.

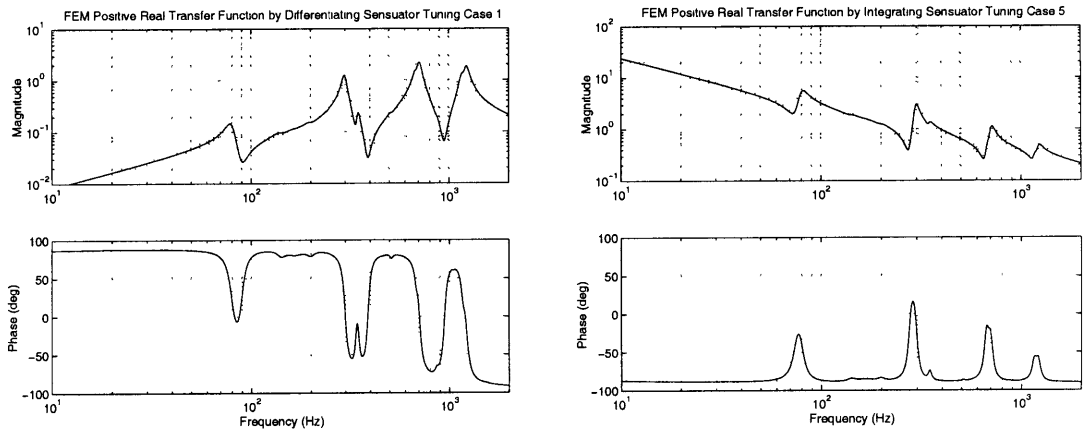

Figure 3.8 Positive real transfer functions for single wafer PZT sensuator.

Both of the above transfer functions present practical implementation problems due to their dereverberated slope. The transfer function achieved through differentiation results in high frequency modes with large magnitude. This means that the compensator must be designed to roll-off very fast to insure gain stabilization of unmodeled high frequency modes. If the compensator were positive real and could be implemented infinitely fast, this would not be a problem since those modes would be phase stabilized. Time delay in digital implementation of the compensator effectively destroys the positive real properties of G_{yu} at high frequencies, so the unmodeled dynamics in practice must be gain stabilized.

The transfer function achieved through integration results in a high gain at low frequency. This presents a practical problem due to the amplitude nonlinearity of the sensuator circuit. As will be discussed in more detail in Chapter 5, the amplitude nonlinearity is quite severe at low frequencies, and has the effect of de-tuning the sensuator. This nonlinearity causes closed-loop stability problems using a PZT sensuator, and integrating the sensuator output will only amplify this problem.

In conclusion, although the stability guarantees of positive real feedback are enticing, the practical problems of time delay and nonlinearity destroy its advantages for this application.

3.2.2 Distributed PZT Sensuator on Plate

Both of the minimum phase tunings for the single wafer sensuator result in a closely spaced zero near the first structural mode. The frequency of transfer function zeros is determined by the sensor and actuator location, or more specifically, where the sum of the modal residues (3.4) equal zero.

$$\frac{\mathbf{C}\Phi_i\Phi_i{}^T\mathbf{B}(s^2-\omega_i{}^2)}{\mathbf{M}_i} \tag{3.4}$$

For the single wafer sensuator, the residue of the second symmetric structural mode is large compared to the first. This forces the zero between these two modes to be close to the first mode. The motivation for the distributed sensuator design is to separate the zero from the first mode by choosing sensuator locations that cause the modal residue of the second mode to be small compared to the first.

Design

A simple clamped-clamped beam was used to determine if varying the location of a collocated PZT sensuator can affect the pole/zero spacing of the transfer function. The modeshapes of a clamped-clamped beam are similar to a cross section of the modes of a clamped circular plate; therefore, what is possible on the beam should be reproducible on the plate. Analytical modeshapes were used and differentiated once with respect to the length coordinate along the beam. [Blevins, 1979] To a rough approximation, the **B** and **C** matrix for a piezo wafer on the beam can be modeled simply as the difference of the slope at the edges of the wafer.

The slope modeshapes of the first two symmetric modes of a clamped-clamped beam are shown in Figure 3.9. It is seen that increasing the coverage area of a centrally placed

piezo does not decrease the residue of the second mode compared to the first until the outer edge of the coverage area exceeds the curvature nodeline of the second symmetric mode. For comparison, the optimum radius of a centrally located circular sensuator for the first two symmetric modes of a clamped circular plate is 0.5153R. [Ko & Tongue, 1995] This is not an effective option using a heavy piezoelectric material like PZT since it would increase the structural weight by approximately 25%. Figure 3.9 also shows that if two PZT wafers are placed near the clamped edges of the beam, their location can be varied to decrease the residue of the second mode compared to the first. For the beam, this configuration would also filter the response from all of the asymmetric modes.

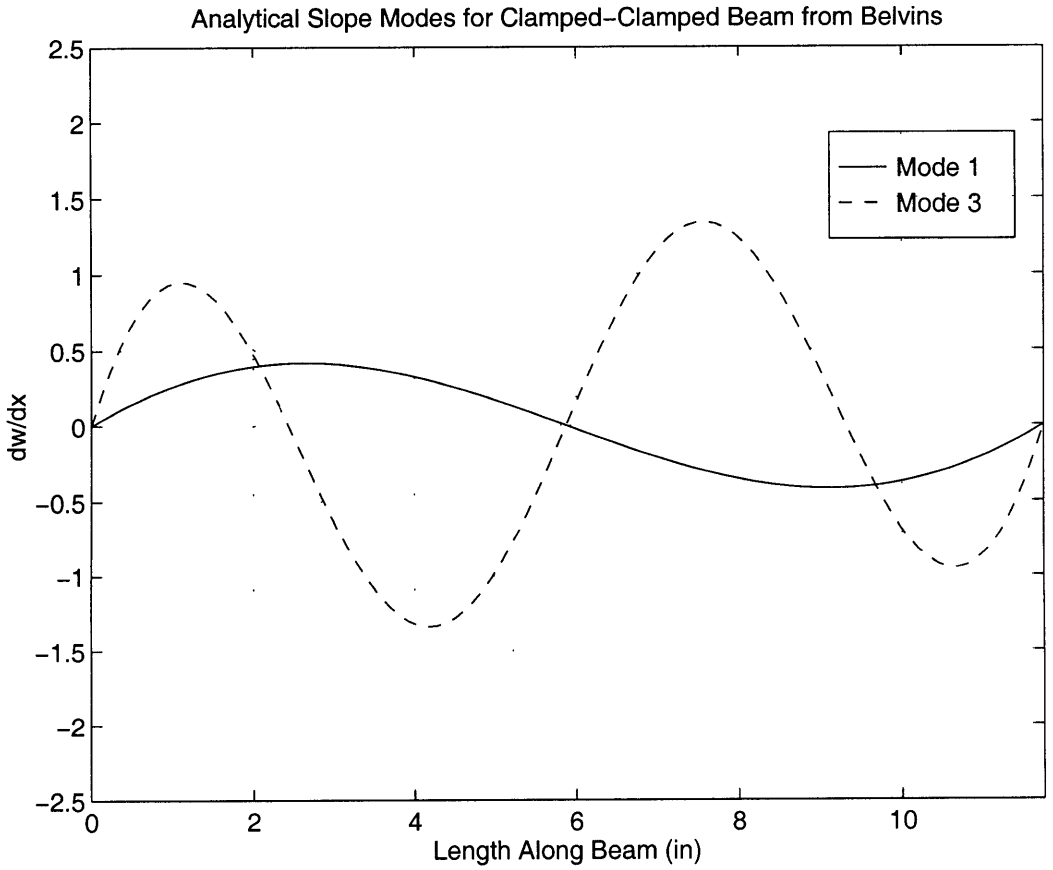

Figure 3.9 Slope nodelines for first two symmetric modes of clamped-clamped beam used for preliminary design of a distributed sensuator.

The final stage in the design is to use the finite element model of the test chamber to determine the best size and configuration of the distributed sensuator on the plate. This is an iterative process where the passive properties of the distributed sensuator are added to the finite element model in ANSYS. The plate modeshapes are recalculated and incorporated into the coupled modal model. The forcing and strain sensing matrices for the sensuator are modeled, and then the sensuator transfer function is predicted. One constraint placed on the sensuator design was that the entire distributed sensuator must be cut from a single 2.5 in. x 1.5 in. wafer. This limits the additional weight that could be added to the structure, and allows actuation authority to be compared between the two sensuator designs.

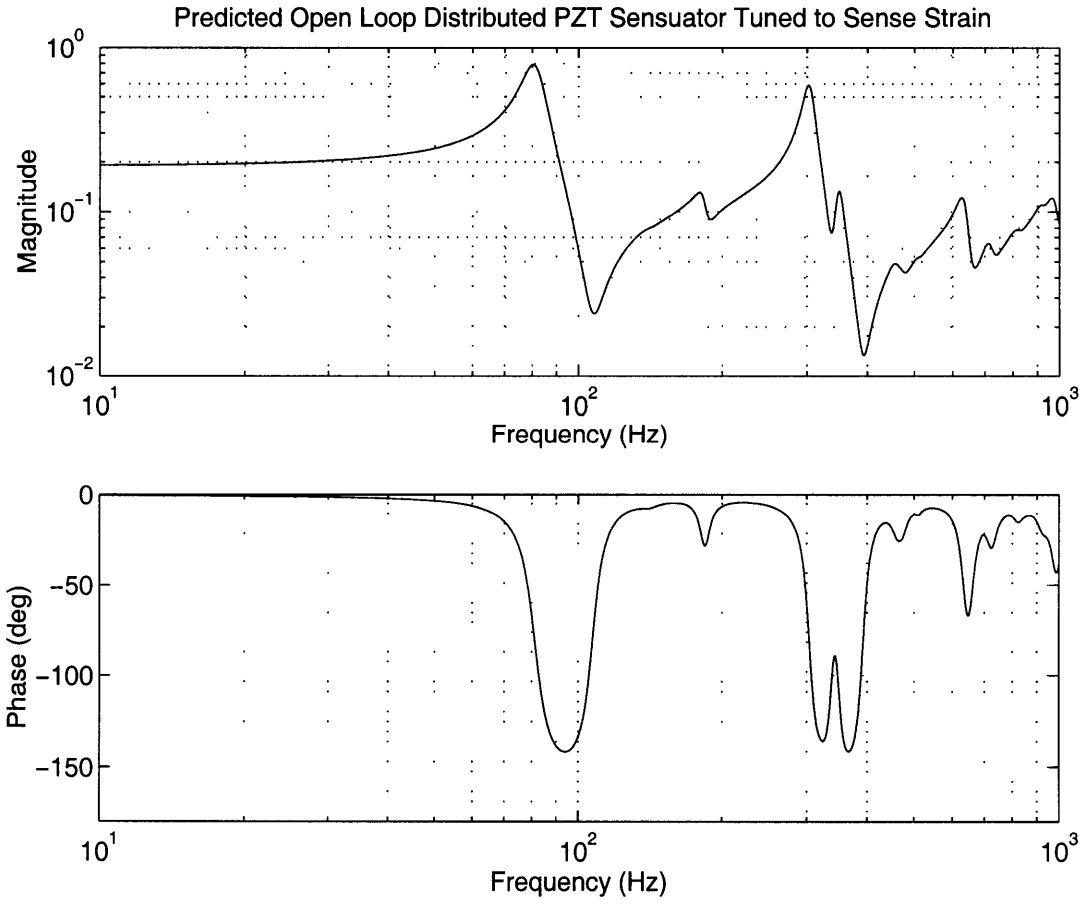

Figure 3.10 Predicted sensuator transfer function from finite element model using four symmetrically distributed PZT wafers.

The best configuration was determined by trial and error to be four 1.5 in. x 0.625 in. wafers placed symmetrically around the circumference with their outer edge 0.35 in. from the clamped edge of the plate. The finite element model of this configuration produces the transfer function shown in Figure 3.10. It is seen that the zero between the first and second plate modes moves to 108 Hz (vs. 90 Hz for the single wafer design). The overall magnitude of the transfer function is less than the single wafer design since the sensuator is not at the optimal location for actuation authority. Finally, an additional mode at 620 Hz is observable in this transfer function. This mode is the plate mode with 8 nodal diameters and corresponding positive lobes centered around each of the four piezo wafers. Below this frequency, the distributed sensuator design effectively filters the asymmetric plate modes (they are slightly visible in the transfer function due to asymmetric approximations made in the passive modeling of the piezo properties).

Implementation

The implementation of a distributed sensuator is more complex than the single wafer design primarily due to slight variations in the capacitance of the wafers. If each of the wafers used in the distributed design were identical, then their electrodes could be connected in parallel. The parallel connection would then be electrically identical to a single wafer, and the circuit in Figure 3.4 would be adequate.

In practice, the magnitude and phase of the electrical admittance (inverse of impedance) of each wafer varies from the others and with frequency. This variance is shown in Figure 3.11 for the four wafers used in the distributed sensuator design. Some of the noise in a sensuator circuit is related to how well the phase of the admittance of a real reference capacitor (nominally 90°) matches the piezo. The tuning gain does not help this part of the noise. Noise is also introduced due to the magnitude of the reference and associated charge sensor capacitance varying from that of the piezo and associated charge sensor capacitance. To solve this problem, a distributed sensuator circuit was constructed which includes independent tuning controls for each wafer. This circuit is shown in Figure 3.12. This circuit replaces the piezo leg of Figure 3.4 between V_I and $-V_p$. In addition, the refer-

ence capacitor of the sensuator circuit is changed to 34ηF to match the distributed wafers, and the fixed resistor in the reference leg is changed to 2.4kΩ.

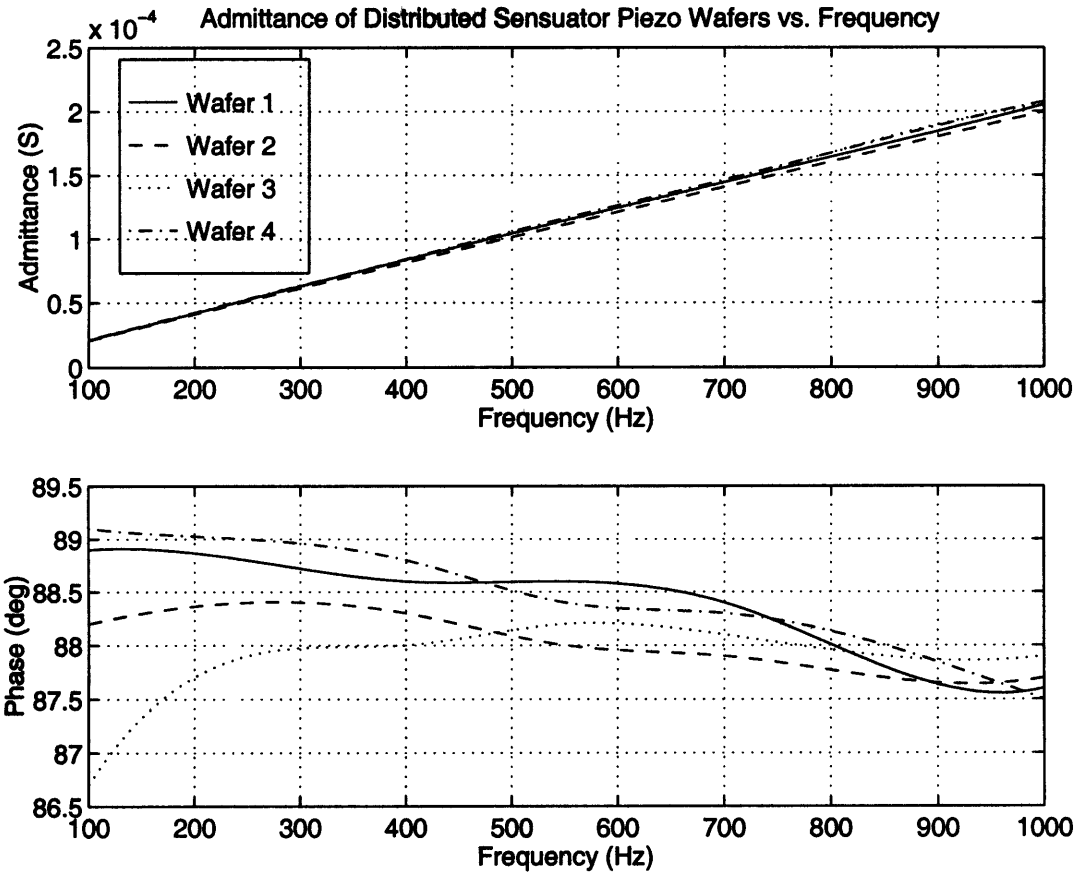

Figure 3.11 Magnitude and phase variation of electrical admittance of distributed sensuator PZT wafers vs. frequency.

Another implementation problem arises since a conductive aluminum plate is used for the experiments. Bonding the wafers to the plate will result in an electrical connection. To resolve this problem, a 0.001 in. layer of Mylar was bonded to the plate to insulate the wafers from each other. Thin copper foil was used to provide access to the lower electrode on each wafer. A photograph of the distributed sensuator wafers bonded to the plate is shown in Figure 3.13.

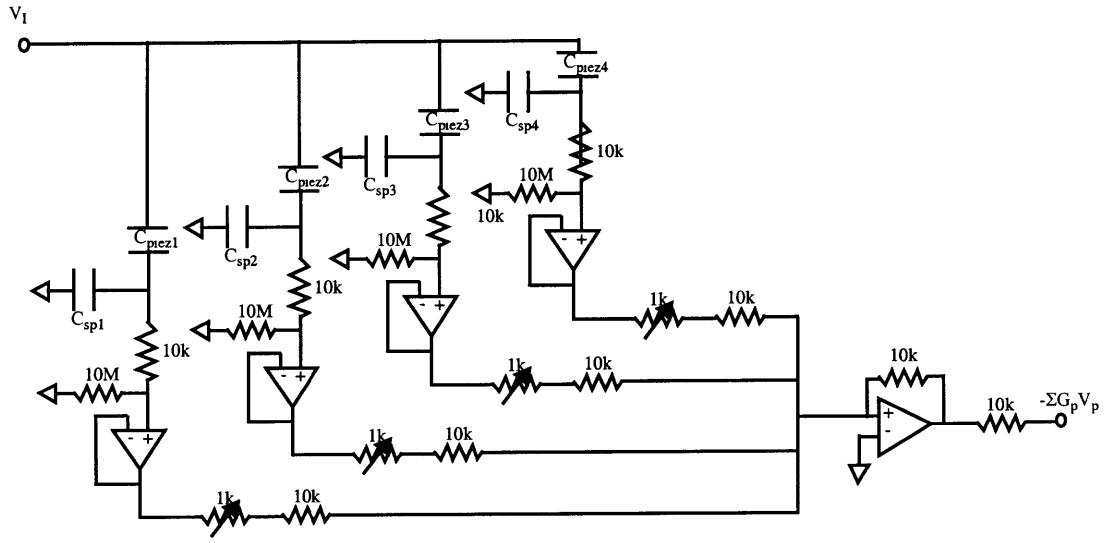

Figure 3.12 Detailed schematic of distributed sensuator circuit.

The wafers are tuned relative to each other by making the output 90° out-of-phase with a low frequency sinusoidal input with unit gain on the reference leg. This tuning assures that Equation (3.5) is satisfied where θ_i is the phase of the piezo admittance. All of the wafers are then connected to the distributed sensuator circuit, and the reference gain is adjusted to tune the sensuator for any of the cases described in Section 3.2.1. This was first done for the plate clamped in the open chamber configuration. The resulting transfer function for the distributed sensuator is shown in Figure 3.14.

$$G_{p1}\frac{C_{piez1}\sin\theta_1}{C_{piez1}+C_{sp1}} = G_{p2}\frac{C_{piez2}\sin\theta_2}{C_{piez2}+C_{sp2}} = \ldots \tag{3.5}$$

Obviously, this transfer function does not achieve the design goal of increasing the pole-zero separation near the first mode. This is caused by either the wafers being placed in the wrong location relative to the structural nodelines, or the noise level of the sensuator covering the actual location of the zeros. To determine if noise is the cause, PVDF sensors were cut to 1.5 in. x 0.625 in. rectangles and bonded to the back of the plate in the same location as the PZT wafers. This gives an independent strain signal with the same spatial filtering as the distributed wafers, but without the electrical noise inherent in the sensuator circuit.

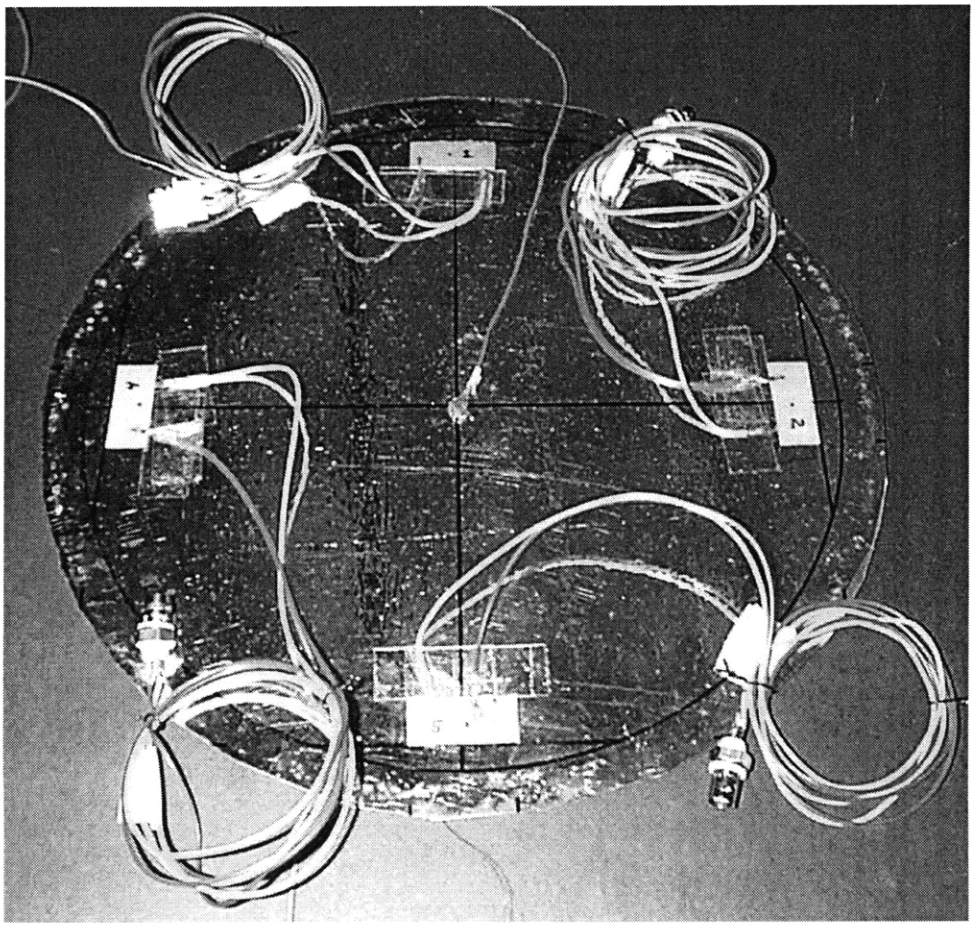

Figure 3.13 Photograph of distributed sensuator wafers bonded to plate.

Figure 3.15 shows the transfer function from the distributed PZT wafers to the sum of the PVDF sensors. As expected, this transfer function is much less noisy than the distributed sensuator. It also shows no observability of the first structural mode near 70 Hz. The similarities between Figure 3.14 and Figure 3.15 are the unobservability of the structural modes near 300 Hz and 700 Hz, and the high observability of the mode near 500 Hz. Since the independent strain measurement is consistent with the sensuator, electrical noise in the circuit is not the cause of the discrepancy between the predicted and experimental transfer functions. Sensitivity of the wafer placement to modeshape uncertainty is more likely the cause of the discrepancy.

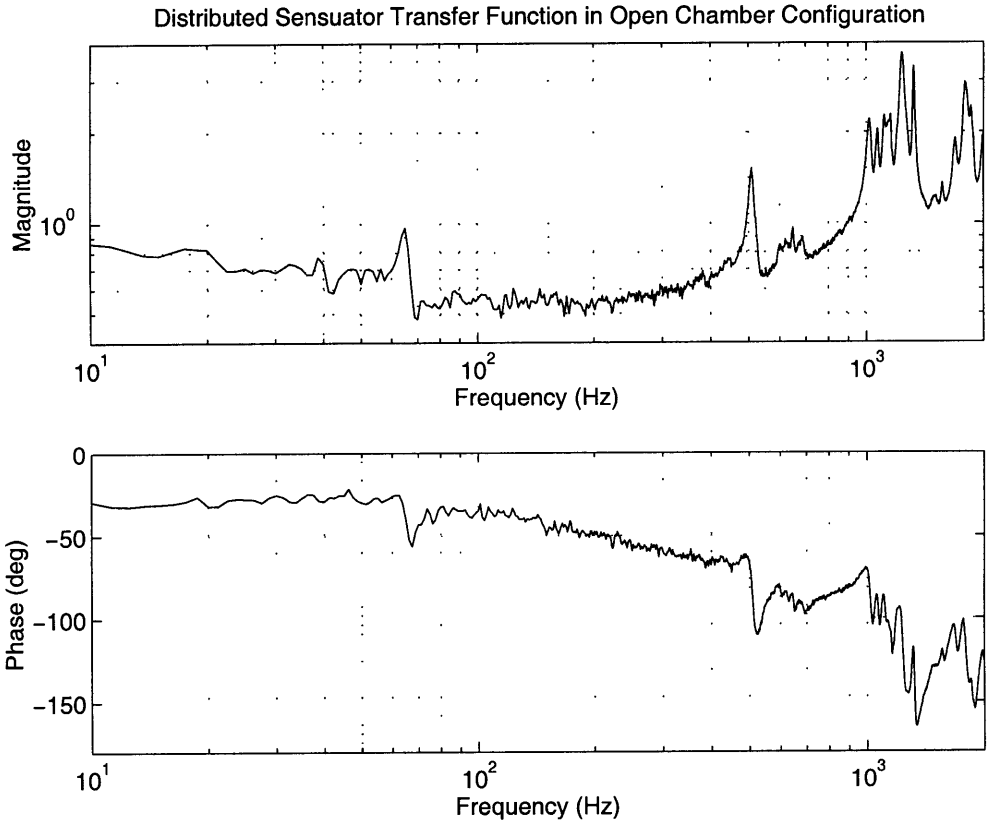

Figure 3.14 Experimental transfer function for distributed PZT sensuator in open chamber configuration.

Sensitivity Analysis

The finite element model was used to determine the sensitivity of the critical zero of the distributed sensuator transfer function to small variations in wafer location. This analysis is motivated by noting that if the wafers are placed 0.25 in. from the edge of the plate in the model (instead of 0.35 in.), the structural modes at 70 Hz, 300 Hz, 620 Hz, and 700 Hz become much less observable. Additionally, a mode near 500 Hz becomes highly observable.

The sensitivity of transmission zeros is derived by taking perturbations of the generalized eigenvalue problem of the input/output system (3.6). The final result of this derivation is (3.7), where Ψ and η are the left and right eigenvectors of (3.6), and $\Delta\mathbf{A}/\Delta\alpha_k$, $\Delta\mathbf{B}/\Delta\alpha_k$,

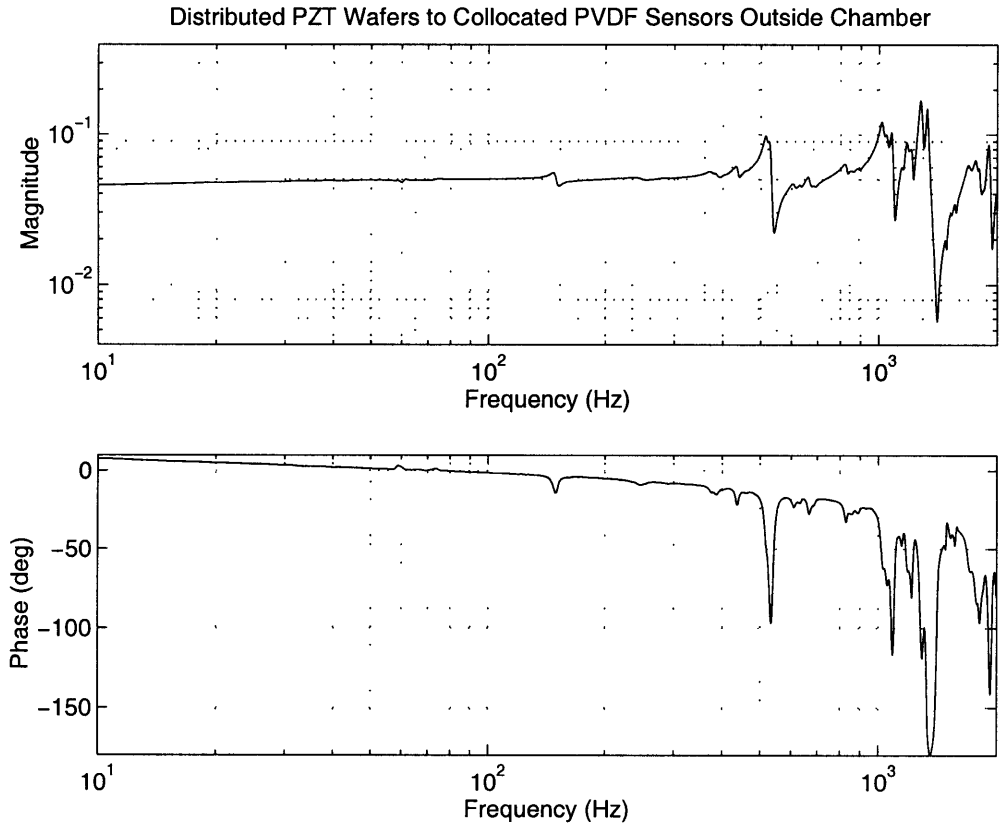

Figure 3.15 Transfer function from distributed PZT wafers to collocated PVDF sensors in open chamber configuration.

$\Delta\mathbf{C}/\Delta\alpha_k$, and $\Delta\mathbf{D}/\Delta\alpha_k$ are discrete derivatives of the state space matrices due to small perturbations. [Masters & Crawley, 1997] Equation (3.7) shows that the zero sensitivity is dependent on changes to the dynamics, sensors, actuators and feedthrough. Sensitivity due to the dynamics can be brought about through manufacturing or boundary condition uncertainties, as well as the passive effect of the sensors and actuators. Sensitivity due to the sensors and actuators is brought about by changing their location, and sensitivity due to feedthrough corresponds to tuning discrepancy in the sensuator circuit.

$$\begin{bmatrix} (z_i\mathbf{I}-\mathbf{A}) & -\mathbf{B} \\ -\mathbf{C} & -\mathbf{D} \end{bmatrix} \begin{bmatrix} \eta_i^s \\ \eta_i^i \end{bmatrix} = 0 \tag{3.6}$$

$$\frac{\Delta z}{\Delta \alpha_k} = \frac{1}{(\Psi^s)^H \eta^s}\left[(\Psi^s)^H \frac{\Delta \mathbf{A}}{\Delta \alpha_k}\eta^s + (\Psi^s)^H \frac{\Delta \mathbf{B}}{\Delta \alpha_k}\eta^i + (\Psi^o)^H \frac{\Delta \mathbf{C}}{\Delta \alpha_k}\eta^s + (\Psi^o)^H \frac{\Delta \mathbf{D}}{\Delta \alpha_k}\eta^i\right] \quad (3.7)$$

For this analysis, the dynamics and feedthrough were assumed to be constant ($\Delta\mathbf{A}/\Delta\alpha_k=0$, $\Delta\mathbf{D}/\Delta\alpha_k=0$), but the radial locations of the sensuator wafers were perturbed. The **B** and **C** matrix derivatives were calculated using a first order central difference with a 0.01 in. change in radial location. This method is similar to assuming that the wafer locations are well defined with the modeshapes being uncertain, but is simpler since it does not require the modeshapes to be recalculated due to an assumed perturbation (e.g. warp or boundary condition uncertainty). Additionally, the zero sensitivity was normalized to the nominal zero frequency to allow comparison of sensitivities in different frequency regions.

The normalized sensitivity of the critical distributed sensuator mode (nominally at 108 Hz) is 0.0103. This corresponds to the zero frequency changing 1.03% for a 0.02 in. change in the radial wafer location. For comparison, the normalized sensitivity of the first zero (nominally at 92 Hz) in the piezo-to-PVDF transfer function due to a perturbation in the sensor radius is 0.0027. As suspected, the distributed sensuator is much more sensitive than the PVDF sensor. This is due primarily to a change in PVDF sensor radius only affecting $\Delta\mathbf{C}/\Delta\alpha_k$, while perturbations in the sensuator location affect both the **B** and **C** matrix derivatives.

A final attempt to implement the distributed sensuator was to bond new sets of four PZT wafers 0.20 in. and 0.50 in. from the edge of the plate. The two new distributed sensuator sets should span the area of reasonable modeshape errors, and hopefully one will provide better observability of the first structural mode for control design. Unfortunately, neither of the two new designs provided a usable transfer function. Additionally, adding the extra wafers to the plate changed the dynamics enough such that the modal observablity achieved with the first design was not able to be reproduced. All of the distributed sensuator designs are based on the assumption that the modeshapes consist of nodal circles and diameters as predicted analytically. The results suggest that the true modeshapes consist

of nodal ovals and chords that would be caused by asymmetries such as warp or localized boundary condition discrepancies.

3.3 Summary

The capabilities and limitations of the finite element model for design of a shaped PVDF sensor and distributed PZT sensuator were investigated. In both cases, the designs are seen to be sensitive to how well the predicted and actual modeshapes match. For the shaped PVDF sensor, this sensitivity was mild and caused only an undesirable observability of the third symmetric plate mode. The distributed sensuator is much more sensitive since modeling errors affect both the actuation and sensing capabilities.

Many of the errors in predicted modeshapes can be attributed to unforeseeable uncertainties such as manufacturing defects (e.g. warp in the aluminum plate) and imperfect boundary conditions. Since manufacturing defects and boundary condition uncertainty are common and tolerated, design methods should not rely solely on ideal finite element model results for sensor and actuator placement. Recent work at Air Force Research Laboratory [Griffin & Denoyer, 1997] addressed this problem by relying totally on experimental data to determine the best location for piezoelectric sensors and actuators. Although this eliminates uncertainty, it also prohibits the use of analytical methods (e.g. modal residue or grammians) for selecting the optimal location. A better approach would be to use information from both a model and experimental data in the design process. This is more time consuming, but necessary if extremely high precision sensor response is needed since it is unrealistic to expect any analytic model to capture unknown manufacturing defects and boundary condition uncertainties.

Chapter 4

PREDICTED COMPENSATOR PERFORMANCE

The previous chapter demonstrated the use of the finite element model for shaped and distributed sensor and actuator design. Since the model is not an exact representation of the physical system, limitations were encountered in the design process, especially where shaping or distribution is very sensitive to modeshape errors. In this chapter, the capabilities and limitations of the finite element model for predicting performance of structural acoustic compensators is investigated.

In order to reduce the sensitivity of these results to parametric (frequency and damping) discrepancies between the model and physical system, the evaluation is based on comparison of compensators designed and implemented on the finite element model vs. compensators designed on a data-fit model and validated through experiment. This comparison is logical since the finite element model is intended as a design tool for predicting response, and not as the basis for a model based compensator (data fit models are much better for the latter).

All of the compensators were designed using the linear quadratic Gaussian (LQG) method. The similarity of the compensators is defined by the sensors and actuators used, and the selection of targeted modes in the cost functional. The acoustic performance metric is defined as the root sum square (RSS) of three discrete microphones distributed in the lower acoustic chamber over a frequency range from 10 Hz - 1000 Hz. The maximum acoustic attenuation is limited by regions of acoustic amplification increasing with control

effort. This is fundamentally driven by open-loop transfer function characteristics (e.g. pole/zero separation). This chapter will present the predicted compensator performance for various sensor/actuator pairs, while Chapter 5 will present experimental results for similar compensators.

4.1 Transmission Compensators

Four acoustic transmission compensators were designed using the finite element model. The first three compensators are meant to be compared as candidates for achieving high levels of acoustic transmission reduction. The final compensator is meant to demonstrate the fidelity of the finite element model, and show the performance trade-off caused when a compensator must be very robust to modeling errors. All of the transmission compensators are designed using the LQG method, with the modal velocity of the first two symmetric plate modes (near 80 Hz and 300 Hz, respectively) targeted in the cost functional. Additionally, a Pade approximation of the time delay due to real-time implementation is augmented to the model so the predicted performance can be compared to experimental results. It is very important to note that although the finite element model captures the acoustics of the chamber, this information is only used to evaluate the performance of a compensator. The feedback sensor for all of the transmission compensators is some measure of the structural vibration (e.g. acceleration, strain etc.), and information about the acoustic performance is not included in the cost functional.

4.1.1 Shaped PVDF Sensor

The first transmission compensator uses a single PZT wafer in the center of the aluminum plate as an actuator and the modally shaped PVDF strain sensor described in Section 3.1. The finite element model was updated between the PVDF sensor design and compensator design to account for the warp in the plate used for the PVDF sensor. This was accomplished by adding an in-plane compressive force along the edge of the plate in ANSYS to account for the destiffening observed when the warped plate is clamped in the chamber. The update allows the model to better capture the output of the shaped sensor on the plate.

Figure 4.1 shows the open-loop vs. predicted closed-loop transfer functions for the disturbance speaker to PVDF sensor and RSS pressure (acoustic performance). The predicted acoustic sound pressure level reduction (performance) at the first and second structural modes is 17.88 dB and 9.46 dB, respectively. The predicted broadband acoustic reduction between 10 Hz and 1000 Hz is 3.64 dB. In addition to the local and broadband performance predictions, Figure 4.1 also shows predicted acoustic amplification below 45 Hz, and between 170 Hz - 250 Hz.

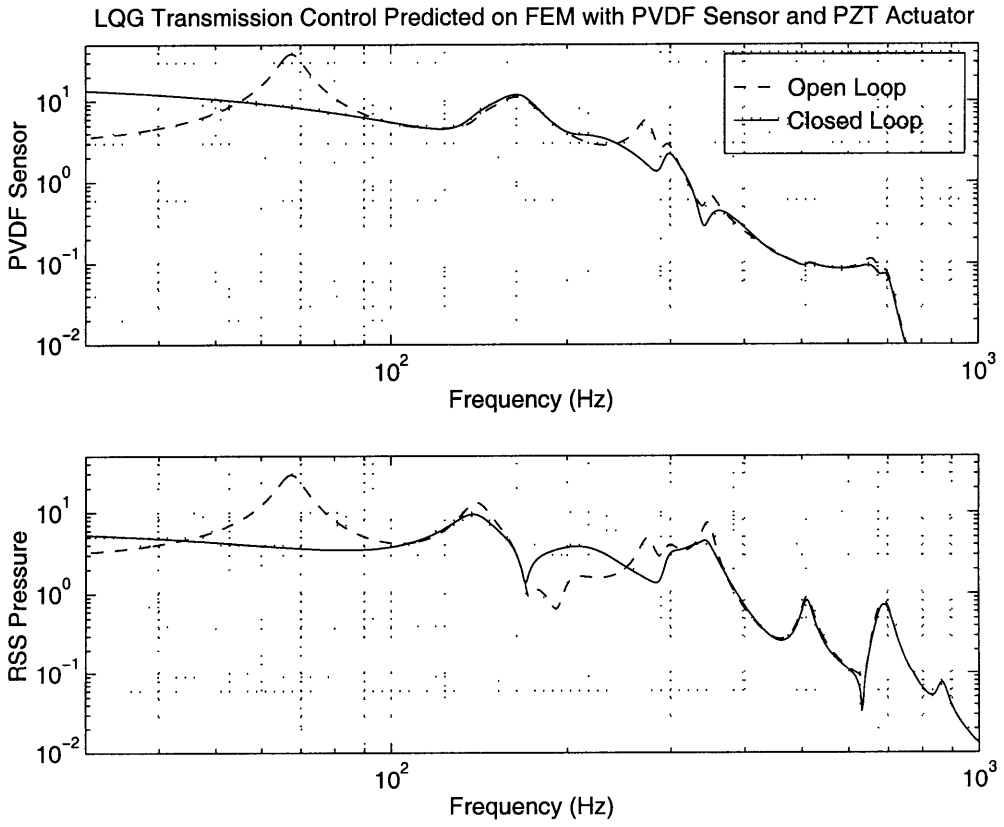

Figure 4.1 Predicted performance of LQG transmission compensator from disturbance speaker to PVDF sensor and RSS pressure.

4.1.2 Single PZT Sensuator

Tuning case 3 was selected as the most favorable transfer function for control design using the single wafer PZT sensuator due to its good pole-zero separation near the first structural

mode. This tuning case is nonminimum phase; however, the nonminimum phase zero occurs far below the first structural mode. Since performance is not sought near the frequency of the nonminimum phase zero, its presence should only cause a slight penalty in robustness and sensor noise rejection outside the control frequency band.

The predicted closed-loop structural and acoustic performance using the single wafer PZT sensuator is shown in Figure 4.2. The broadband acoustic reduction is 3.31 dB, with 13.31 dB and 10.05 dB at the first and second structural modes, respectively. Acoustic amplification is also predicted below 55 Hz, and between 180 Hz - 280 Hz. The predicted acoustic performance using the PVDF sensor and the PZT sensuator is very similar. Effects of the sensor distribution and nonlinearity will be shown in Chapter 5 to cause significant implementation differences between the two designs.

4.1.3 Distributed PZT Sensuator

Although the distributed sensuator was not successfully implemented, the predicted performance in a feedback compensator is presented for comparison to the other designs. Since the goal of the distributed sensuator is to increase the pole-zero separation without creating nonminimum phase zeros, tuning the sensuator to sense distributed strain (tuning case 1) is the obvious choice for this design. For this tuning, the observability and controllability of the first structural mode is not as good as for tuning case 3 using the single wafer sensuator. The performance therefore should be less than for the nonminimum phase tuning of the single wafer sensuator; however, this design will be more robust to model discrepancies since it is minimum phase.

Figure 4.3 shows the predicted open and closed-loop performance from the disturbance speaker to the distributed sensuator and RSS pressure. The predicted broadband acoustic reduction is 2.88 dB, with 12.34 dB and 8.54 dB attained at the first and second structural modes, respectively. As expected, this is less than predicted for the nonminimum phase tuning of the single wafer sensuator.

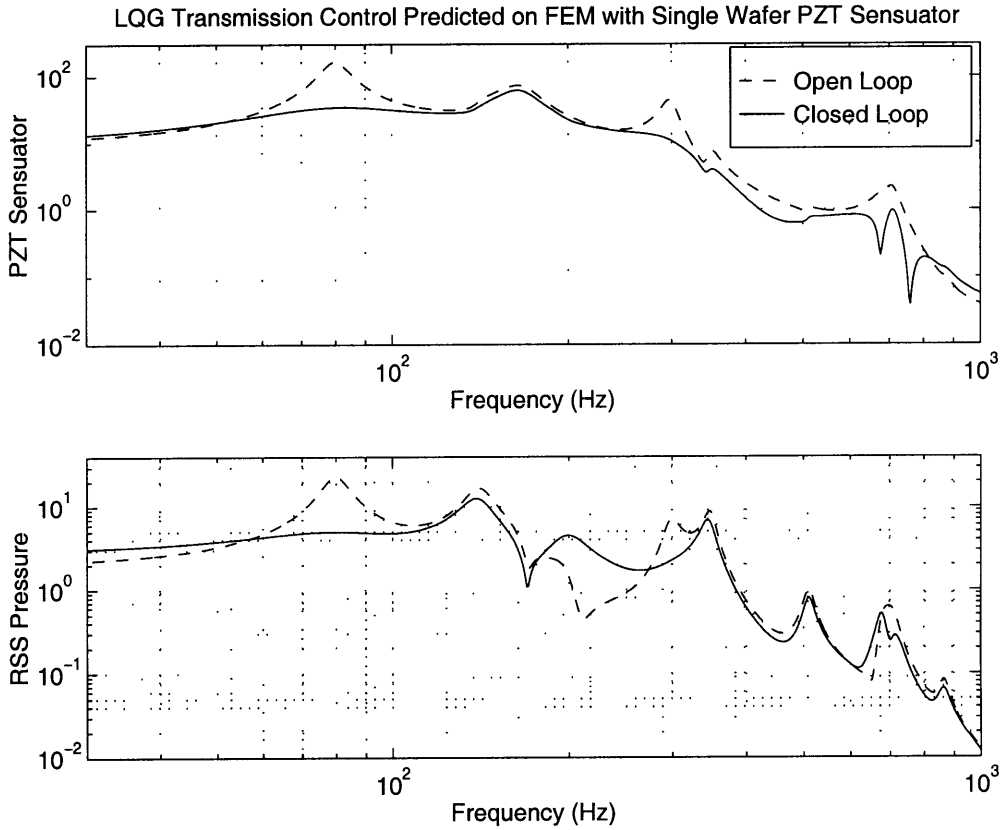

Figure 4.2 Predicted performance of LQG transmission compensator from disturbance speaker to single wafer PZT sensuator and RSS pressure.

4.1.4 FEM Based Compensator

A LQG transmission compensator was designed and implemented using the finite element model as the basis for the state estimator. The feedback sensor used for this compensator was a single accelerometer located at the center of the plate. As with the previous compensator designs, the finite element model is used to predict the closed-loop performance. Unlike the previous designs, the same compensator is intended to be implemented on the chamber. The purpose of this compensator design is to demonstrate the fidelity of the finite element model, and show the performance trade-off required for robustness to modeling errors in the performance frequency band.

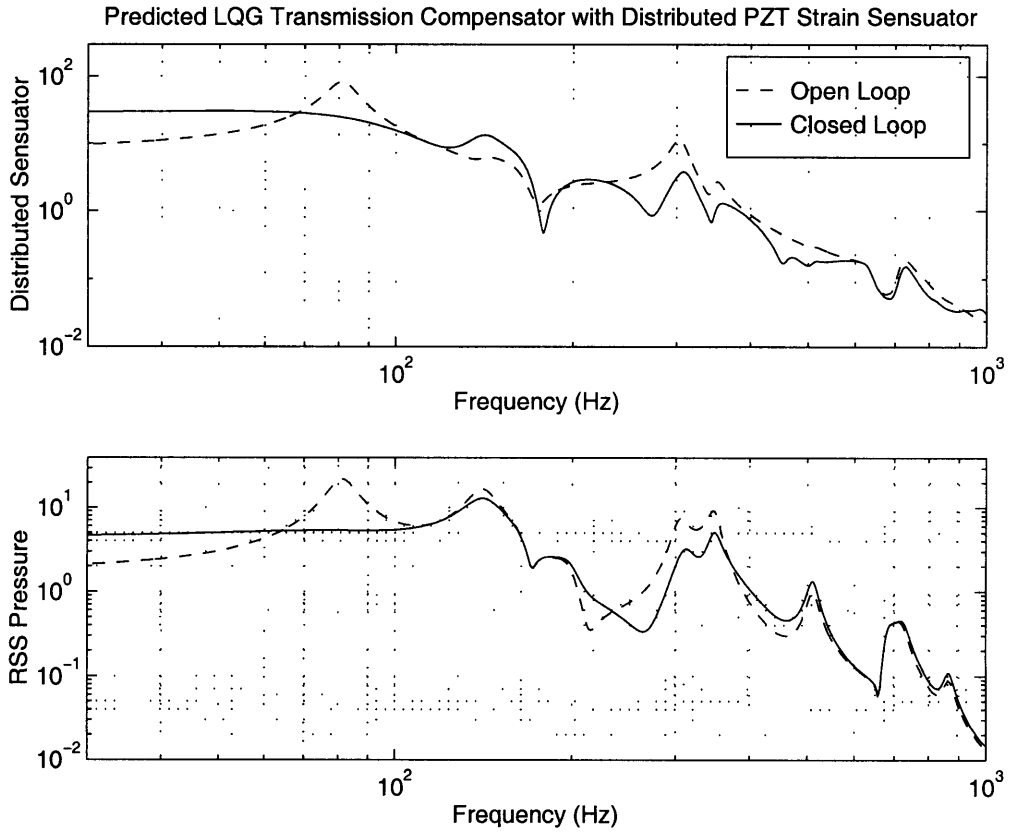

Figure 4.3 Predicted performance of LQG transmission compensator from disturbance speaker to distributed PZT sensuator and RSS pressure.

Since the PZT wafer to accelerometer transfer function rolls up, a control frequency weighting was used to penalize the control input more at high frequency than in the region near the targeted structural modes. This forces the compensator transfer function to roll off fast enough to gain stabilize unmodeled high-frequency dynamics. The targeted modes were sensitivity weighted to make the compensator robust to modeling errors. [Lublin & Athans, 1996] This results in decreased predicted performance, but is necessary to achieve performance and stability when implemented experimentally. This step was not included in the previous designs since it is assumed that a very accurate data-fit model can be synthesized over the desired performance bandwidth.

Figure 4.4 shows the open and closed-loop structural and acoustic performance predicted using the finite-element model. The broadband acoustic performance is only 1.55 dB, due

to the trade-off incurred by making the compensator robust enough to be implemented on the chamber. The acoustic performance at the first and second structural modes is 9.40 dB and 10.61 dB, respectively. In Chapter 5, the implemented performance of this compensator is shown to be very close to these predicted results.

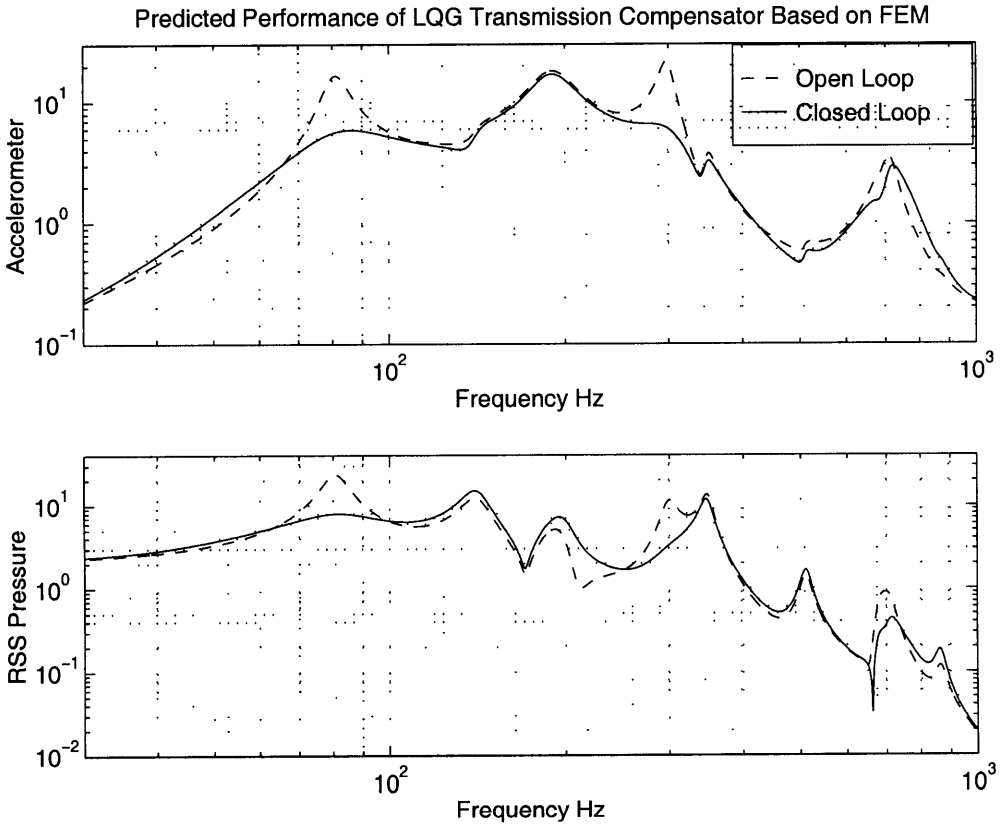

Figure 4.4 Predicted performance of FEM based LQG transmission compensator from disturbance speaker to accelerometer and RSS pressure.

4.2 Reflection Compensator

A multi-input, multi-output (MIMO) compensator was designed using the finite element model to control both transmission through the plate, and reflection of the acoustics in the lower chamber. The PVDF sensor and PZT actuator were used to control the plate vibration, while the speaker in the bottom chamber and collocated microphone were used for reflection control. A LQG design method was used with modal velocity of the first two

symmetric plate modes, and first three longitudinal acoustic modes targeted in the cost functional. This compensator is comparable to one designed and implemented by Asari, and the predicted performance will be compared to those results in Chapter 5.

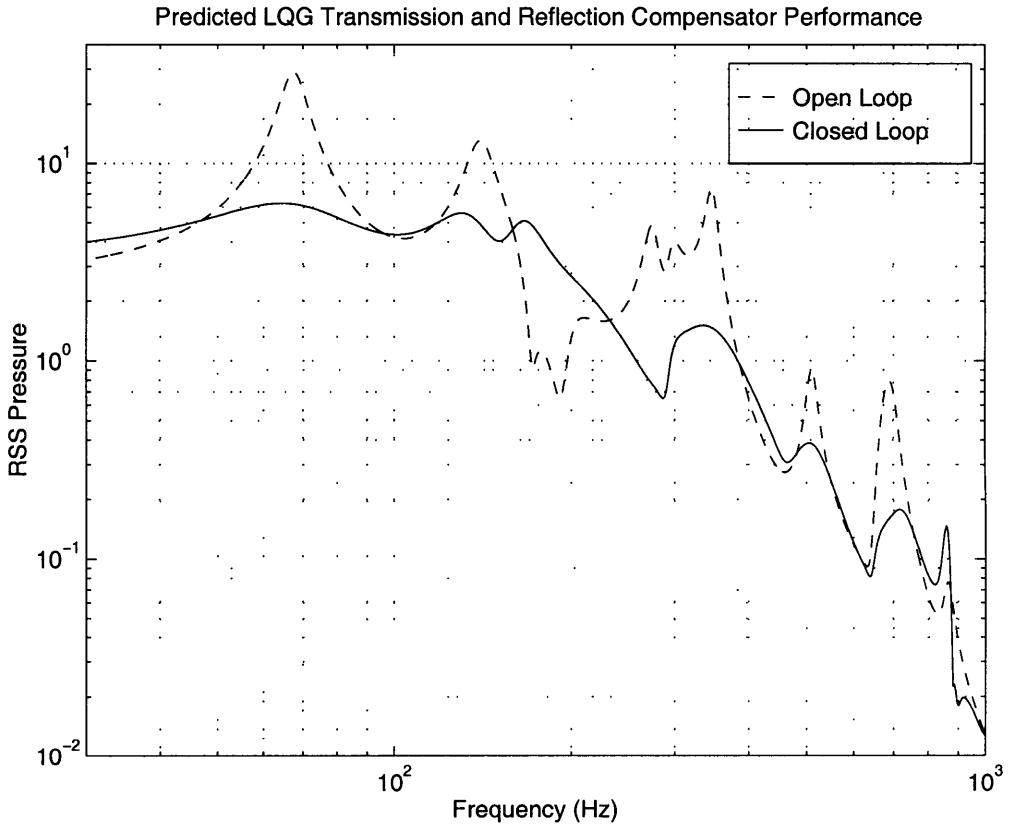

Figure 4.5 Predicted performance of MIMO LQG transmission and reflection compensator from disturbance speaker to RSS pressure.

Figure 4.5 shows the predicted open and closed-loop acoustic performance for the MIMO transmission and reflection compensator. The predicted broadband performance is 5.10 dB. The acoustic performance at the first two structural modes is 13.37 dB and 15.90 dB respectively, while the performance at the three targeted acoustic modes is 8.52 dB (140 Hz), 14.09 dB (345 Hz), and 7.53 dB (511 Hz). Comparing these results to those predicted using the transmission compensator with the PVDF sensor alone show an expected broadband improvement due to the additional reflection control. Less expected is the con-

siderable narrowband performance variation at the two structural modes. This is also seen in the implemented results presented in Chapter 5, and can only be attributed to coupling between the structure and acoustics.

4.3 Summary

The performance of four acoustic transmission compensators and one combined transmission and reflection compensator was predicted using the finite element model of the test chamber. Broadband and narrowband acoustic performance at each of the targeted modes was presented, as well as regions of significant acoustic amplification. The predicted performance suggests that the best design for acoustic transmission control is the PZT wafer and modally shaped PVDF sensor. For all of the compensators except the distributed sensuator design, the performance presented in this chapter will be compared to experimentally measured performance in Chapter 5. Conclusions will be drawn concerning the capabilities of using the finite element model to predict compensator performance, and comparison of the designs.

Chapter 5

EXPERIMENTAL VALIDATION

Compensators using the sensor/actuator pairs described in the previous chapter were experimentally implemented on the acoustic test chamber. In all cases, except for the finite element model based compensator, the results presented in this chapter were achieved by redesigning the compensator using a model fit to data from the test chamber. This is consistent with the use of a finite element model as a preliminary design tool to predict achievable performance, while acknowledging that a more accurate model is necessary for high performance implementation. Figure 5.1 shows the typical accuracy achievable using a data-fit model. The performance achieved experimentally is compared to the predicted performance over a broadband frequency range from 10 Hz - 1000 Hz, and locally at each of the targeted modes.

5.1 Transmission Compensators

Compensators using the modally shaped PVDF sensor and single wafer PZT sensuator were re-designed using a data-fit model of the open-loop transfer functions. These designs were implemented as candidates for high performance acoustic attenuation. The FEM based compensator was implemented to prove the fidelity of the finite element model, and show the trade-off between performance and robustness. The distributed sensuator design was not implemented since an adequate open-loop transfer function was not achieved. In all cases, the modal velocities of the first two symmetric plate modes were targeted in the

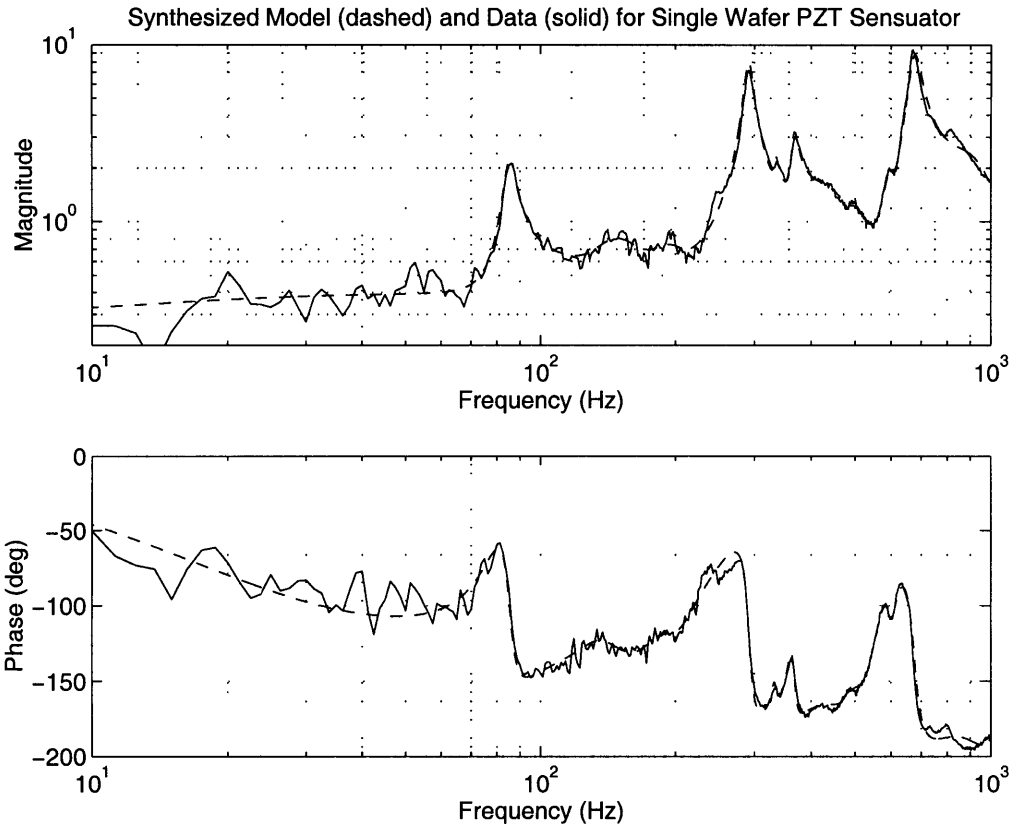

Figure 5.1 Comparison of data-fit model to data for single wafer PZT sensuator transfer function.

LQG cost functional. A Pade approximation of the time delay due to digital implementation was also augmented to the design models so the associated phase lag could be anticipated in the compensator designs. As in the previous chapter, the acoustic performance is not included in the cost functional for the compensator design (in fact, the disturbance and control to performance transfer functions are not included in the synthesized design model).

5.1.1 Shaped PVDF Sensor

The transmission compensator using a single PZT wafer and modally shaped PVDF strain sensor was designed and implemented by Asari. The results from this design are shown here to validate the performance prediction capability of the finite element model. Figure 5.2 shows the open-loop vs. closed-loop data for the disturbance speaker to PVDF

sensor and RSS pressure alongside the predicted performance using the finite element model. The acoustic performance at the first and second structural modes is 17.37 dB and 16.15 dB, respectively. The broadband performance between 10 Hz and 1000 Hz is 4.56 dB. It should also be noted that the data shows acoustic amplification below 50 Hz, and between 160 Hz and 240 Hz. [Asari, 1998] The broadband performance is moderately higher than was predicted; however, the narrowband performance at each mode and the regions of amplification compare well with the prediction.

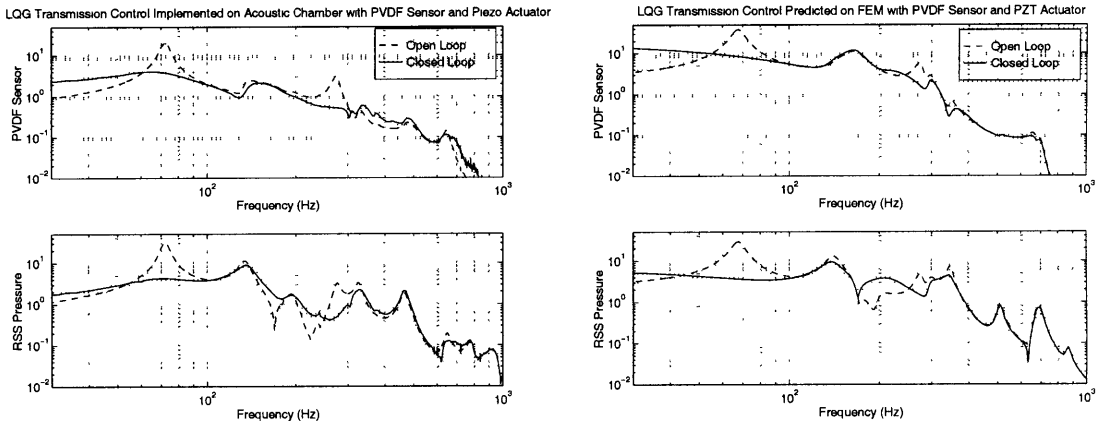

Figure 5.2 Implemented and predicted performance of LQG transmission compensator from disturbance speaker to PVDF sensor and RSS pressure.

5.1.2 Single PZT Sensuator

A transmission compensator using the single wafer PZT sensuator tuned for large pole-zero separation near the first structural mode was designed using a model fit to data from the chamber. The data-fit model includes a nonminimum phase zero at 24 Hz in the sensuator transfer function, which is 14 Hz higher than expected by the finite element model for this tuning. Prior to experimentally implementing the compensator, the performance was predicted by convolving the compensator transfer function with data from the chamber. This method is used to predict the closed-loop performance and stability, in the presence of dynamics and noise in the data that are neglected in the model. This predicted

performance is shown in Figure 5.3 alongside the predicted performance using the finite element model.

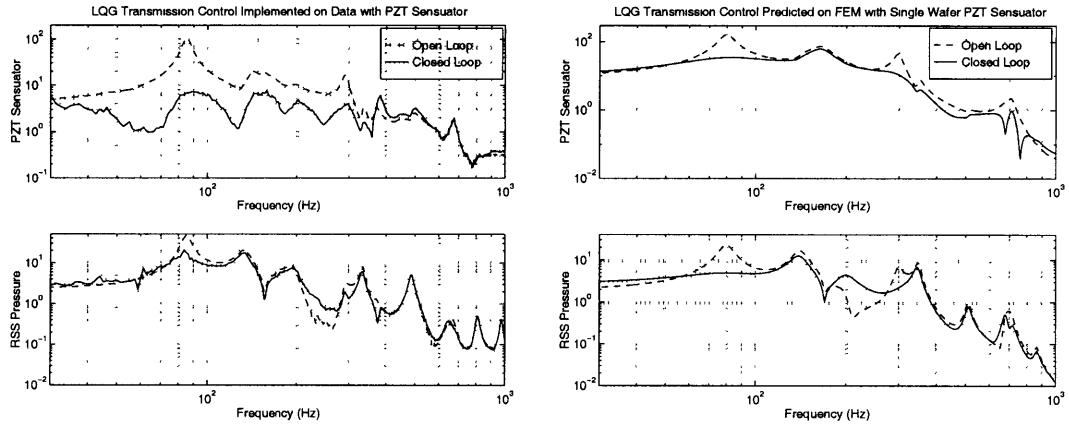

Figure 5.3 Predicted performance of LQG transmission compensator from disturbance speaker to sensuator and RSS pressure convolved with data and using finite element model.

The predicted broadband acoustic performance between 10 Hz - 1000 Hz is 3.19 dB. This includes 8.25 dB at the first structural mode, and 5.86 dB at the second structural mode. The RSS pressure is amplified in the range between 197 Hz - 277 Hz. The predicted acoustic performance is slightly less than that predicted using the finite element model in Section 4.1.2. This is likely due to the nonminimum phase zero in the finite element model being farther from the performance band than in the data-fit model.

An interesting feature of Figure 5.3 is that the predicted sensuator signal attenuation is much greater than the acoustic performance. This is not predicted by the finite element model, and not consistent with the relation between feedback sensor signal and RSS pressure performance using the shaped PVDF sensor. An explanation for this behavior is that the compensator is minimizing the strain locally over the area of the plate covered by the PZT. Since the covered area is small and collocated with the control input, strain minimization does not necessarily correspond to global vibration control of the targeted modes. The reason this behavior is not predicted by the finite element model is that the high fre-

quency modeshapes required to capture the resulting vibration of the plate were truncated during model reduction.

The compensator was next implemented on the chamber using real-time digital computation of the control input. Closed-loop stability could only be achieved for very low disturbance levels, and the achieved broadband acoustic performance was much less than predicted. Figure 5.4 shows the open and closed-loop data for a stable implementation of the compensator. The broadband acoustic performance is 1.61 dB, with 4.69 dB and 7.36 dB at the first and second structural modes respectively.

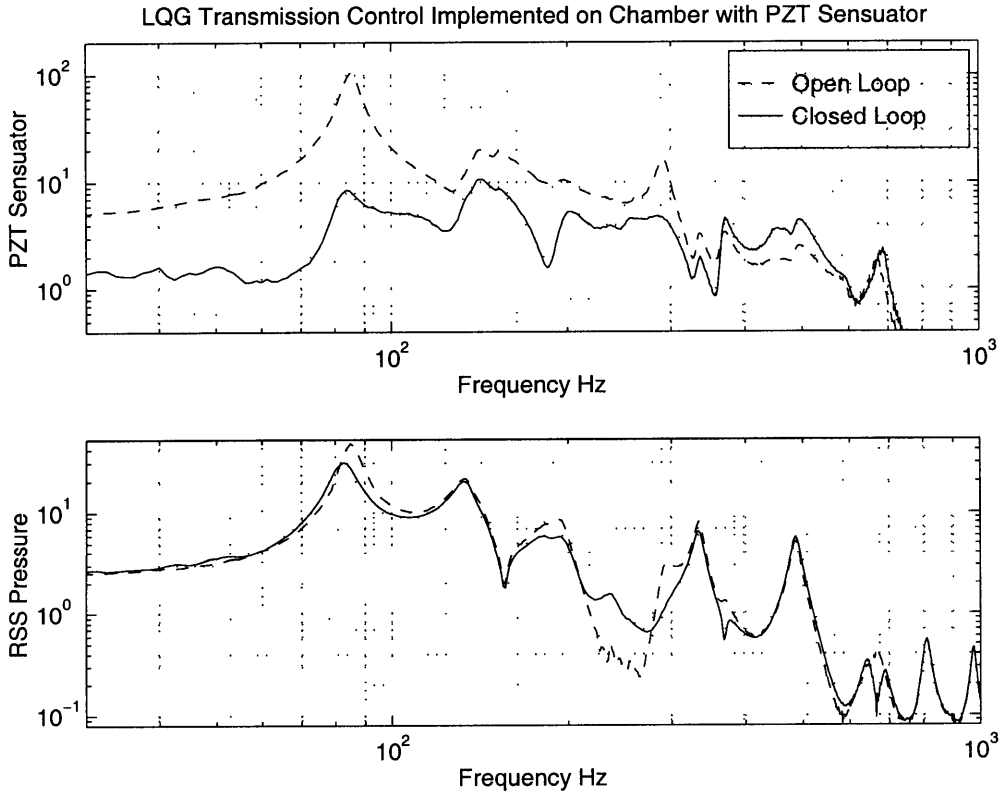

Figure 5.4 Implemented performance of LQG transmission compensator from disturbance speaker to sensuator and RSS pressure.

The cause of the compensator stability problems and limited performance is an amplitude nonlinearity exhibited by the sensuator circuit. This nonlinearity is more severe at low fre-

quency, and has the effect of de-tuning the sensuator. Figure 5.5 is a Nichols plot of the loop transfer function that shows how this nonlinearity affects the stability. The data-fit model was designed around a control input of 100 mV, and the loop is stable for this control level. At higher control levels, the nonlinearity causes the loop to be unstable. This behavior explains why the implementation was only stable for low disturbance levels, and why the performance was less than predicted.

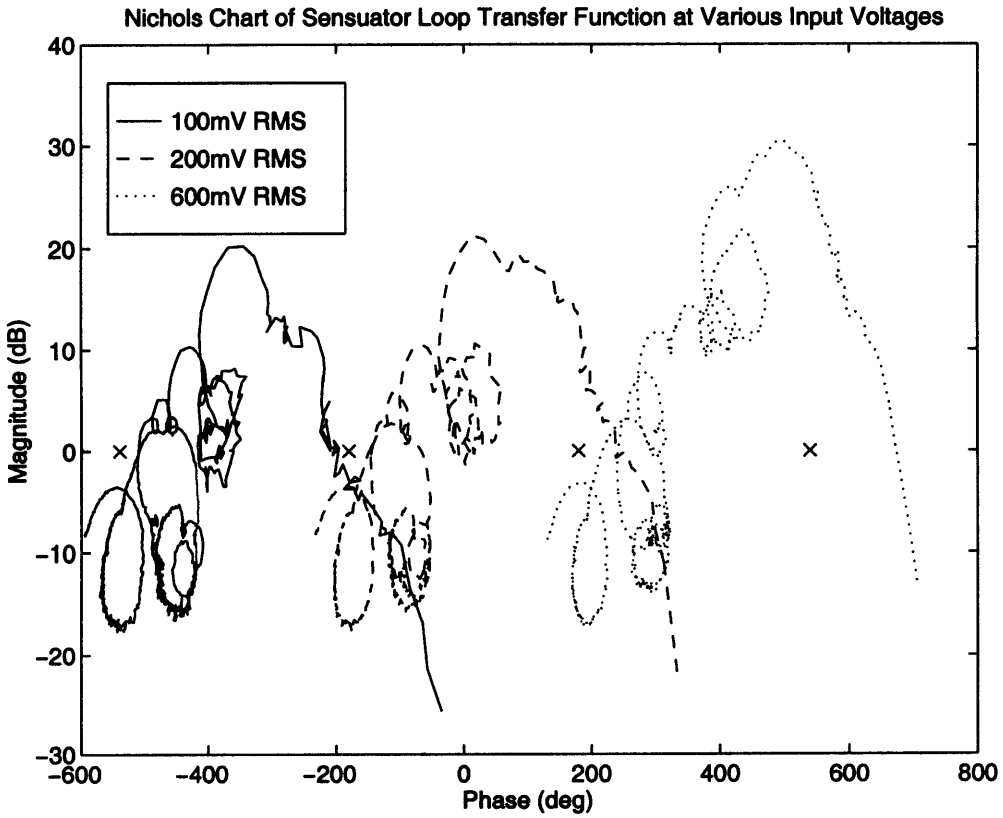

Figure 5.5 Nichols plots of loop transfer function showing sensuator amplitude nonlinearity and resulting closed-loop instability.

A second implementation of the compensator was attempted where both the disturbance level and control gain were varied to maximize the broadband performance. This corresponds to setting the closed-loop control input level to an amplitude region centered around the linearization point of the compensator design model. As expected, the broadband performance varied with both disturbance level and control gain. The maximum

broadband performance achieved was 2.05 dB, with 6.66 dB and 4.46 dB at the first and second structural modes. This implementation is shown in Figure 5.6.

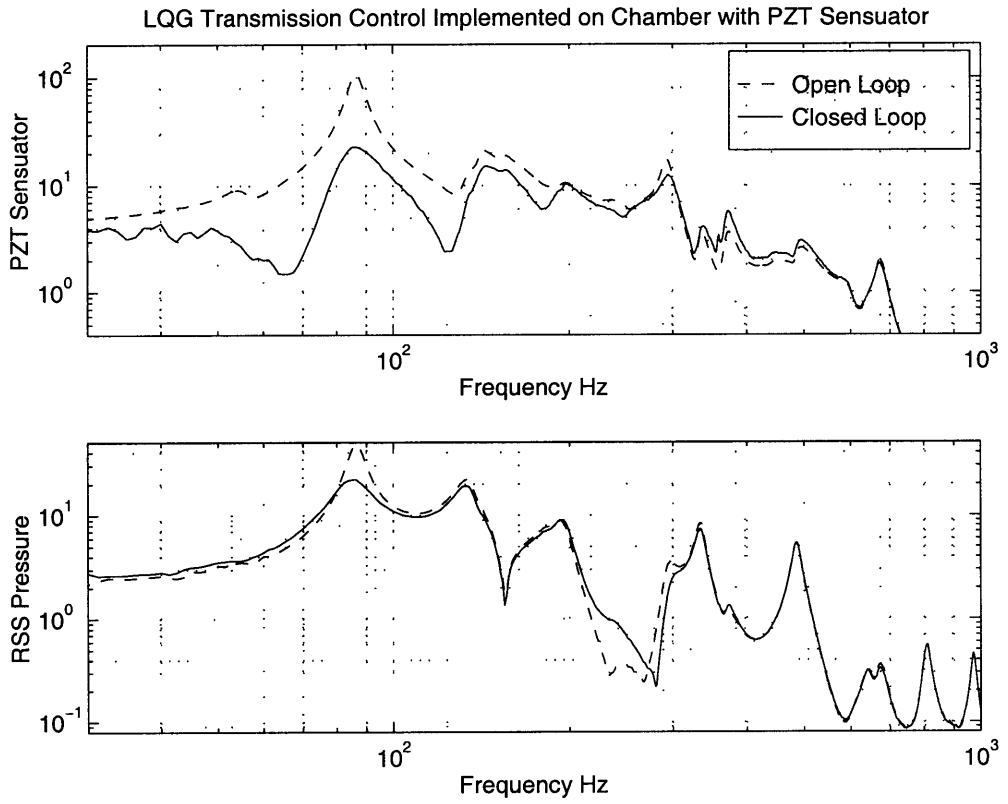

Figure 5.6 Implemented LQG compensator using single wafer PZT wafer manually adjusted for maximum broadband acoustic performance.

Comparing Figure 5.4 and Figure 5.6 shows that the increased broadband performance is gained by shifting the performance distribution between the first and second structural modes. The first implementation actually exceeds the performance prediction at the second structural mode, but the performance at the first mode is far less. The second implementation increased the performance at the first mode, and decreased the performance at the second. Since the first structural mode has the highest amplitude in the disturbance-to-performance transfer function, attenuating this mode has the greatest impact on broadband performance.

Finally, the presence of a nonminimum phase zero amplifies the effect of the sensuator nonlinearity by increasing the sensitivity to unmodeled dynamics away from the performance region. The sensuator nonlinearity can be thought of as a plant variation that is more severe at low frequency. Reducing this sensitivity in the presence of a low frequency nonminimum phase zero would result in high sensitivity to unmodeled high frequency dynamics and sensor noise amplification. While a nonminimum phase zero far below the performance frequency band may itself be acceptable, coupled with the low frequency nonlinearity it severely limits the achievable performance.

5.1.3 FEM Based Compensator

The finite element based compensator described in Section 4.1.4 was implemented on the test chamber. The implemented open and closed-loop structural and acoustic performance is shown in Figure 5.7 alongside the predicted performance from the finite element model. The broadband acoustic performance is 1.31 dB. The acoustic performance at the first and second structural modes is 8.63 dB and 5.76 dB respectively. Again, this performance reflects the trade-off between performance and robustness. The important points of this implementation are that the finite element model captures all of the significant dynamics of the test chamber well enough to be used as the basis for a state estimator, and the predicted performance closely matches the implemented performance.

5.2 Reflection Compensator

The combined transmission and reflection compensator was implemented by Asari using successive closure of the transmission loop followed by the reflection loop. [Asari, 1998] The transmission compensator used the PZT wafer and shaped PVDF sensor, while the reflection compensator used the bottom chamber speaker and collocated microphone. A successive loop closure method was used instead of a MIMO design to allow separate computers to be used in parallel to calculate the control inputs. The model and compensator for a MIMO design required more states than could be efficiently processed using one computer. Although this method is not entirely equivalent to a MIMO design, it is close

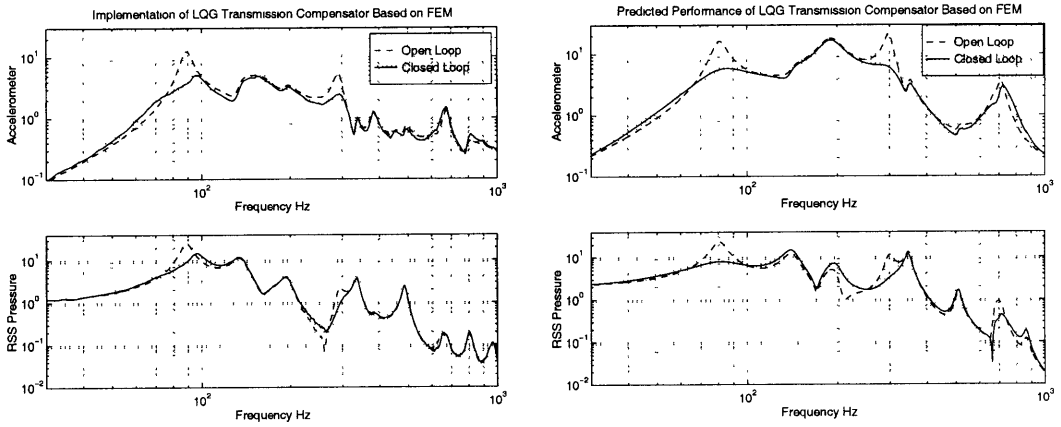

Figure 5.7 Implemented and predicted performance of LQG finite element model based transmission compensator from disturbance speaker to accelerometer and RSS pressure.

enough to allow comparison between the implemented results and those predicted using the finite element model. The results from the successive loop closure design of Asari are shown in this section to validate the capabilities of the finite element model for predicting closed-loop performance.

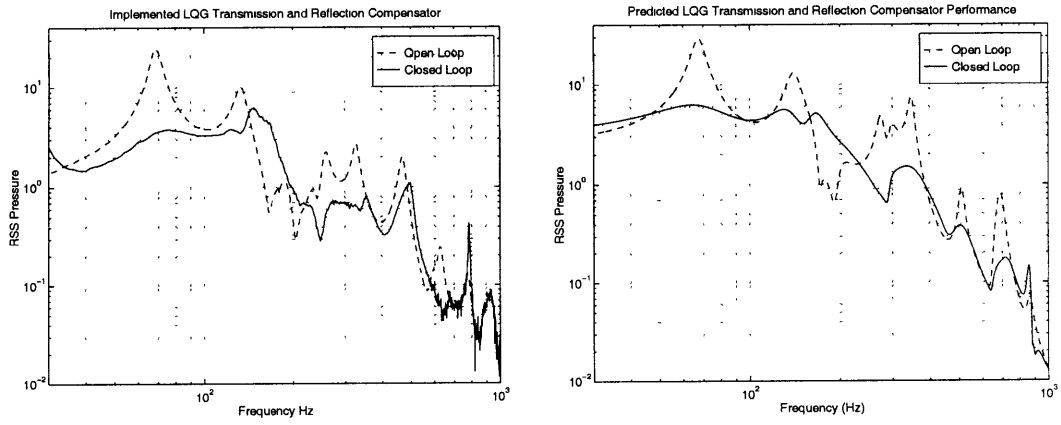

Figure 5.8 Implemented and predicted performance of LQG transmission and reflection compensator from disturbance speaker to RSS pressure using successive loop closure.

Figure 5.8 shows the acoustic performance achieved through the successive loop closure alongside the predicted performance from the finite element model. The broadband performance is 5.28 dB, with 16.82 dB and 11.81 dB at the first and second structural modes

respectively. The attenuation at the three targeted acoustic modes is 9.23 dB, 12.59 dB and 8.02 dB respectively. Both the broadband and narrowband performance compares very well to that predicted using the finite element model.

5.3 Comparison of Predicted vs. Experimental Performance

Table 5.1 summarizes the predicted and implemented performance for each of the compensator designs. For the most part, the performance predicted using the finite element model compares well to the implemented performance both broadband, and locally at the targeted modes. Exceptions to this are the PZT sensuator, and broadband performance using the shaped PVDF sensor. For the sensuator, the implemented performance is much lower due to amplitude nonlinearity. The results predicted using the finite element model are much closer to those predicted through convolution of the compensator with data. This method predicts the achievable performance if the sensuator were linear. For the PVDF sensor, the implemented broadband performance is higher than predicted by the finite element model. This discrepancy may be attributable to modeling assumptions used for the warped plate, although the narrowband performance (especially at the first structural mode) compares well. Performance data is not included at the third acoustic mode for the transmission compensators since this mode is not near either of the targeted structural modes. The influence of the transmission compensators on this mode is small, and comparing the predicted and implemented performance at this mode is not very useful.

In addition to the quantitative comparison presented in the table, qualitatively comparing the plots of the predicted and implemented closed-loop transfer functions show many similarities. Acoustic amplification at low frequency and in the region around the lower chamber speaker mode is seen in both the predicted and implemented performance. Also, the broadband performance trends using various sensors and actuators are captured in the model prediction. This aspect is discussed more in the following section.

TABLE 5.1 Performance comparison between FEM prediction and implementation

	Broadband	1st Structure	2nd Structure	1st Acoustic	2nd Acoustic	3rd Acoustic
Predicted PVDF	3.64 dB	17.88 dB	9.46 dB	0.14 dB	4.74 dB	N/A
Implemented PVDF	4.56 dB	17.37 dB	16.15 dB	2.16 dB	3.62 dB	N/A
Predicted Sensuator	3.31 dB	13.31 dB	10.05 dB	2.63 dB	2.42 dB	N/A
Predicted Sensuator (data)	3.19 dB	8.25 dB	5.86 dB	1.52 dB	2.32 dB	N/A
Implemented Sensuator	2.05 dB	6.66 dB	4.46 dB	1.21 dB	1.21 dB	N/A
Predicted FEM Based	1.55 dB	9.40 dB	10.61 dB	-1.75 dB	1.20 dB	N/A
Implemented FEM Based	1.31 dB	8.63 dB	5.76 dB	-0.31 dB	1.32 dB	N/A
Predicted Reflection	5.10 dB	13.37 dB	15.90 dB	8.52 dB	14.09 dB	7.53 dB
Implemented Reflection	5.28 dB	16.82 dB	11.81 dB	9.23 dB	12.59 dB	8.02 dB

5.4 Comparison of Shaped PVDF Sensor vs. PZT Sensuator

At the beginning of this research, both a modally shaped PVDF sensor, and a PZT sensuator seemed like good choices for acoustic transmission control. The PVDF provides a highly distributed sensuator which can be shaped for high observability of the targeted transmission modes. The PZT sensuator provides a perfectly collocated transfer function, and a method to electronically adjust the pole-zero separation. The finite element model predicts that slightly better broadband acoustic performance is achievable using the PVDF sensor; however, the most dramatic difference between the two sensors is seen during implementation.

Tuning the PZT sensuator immediately reveals a trade-off between good pole-zero separation and the presence of nonminimum phase zeros. Additionally, closed-loop implementation is difficult because the sensuator is nonlinear with input voltage, and the collocated distributed strain signal does not directly correlate to acoustic attenuation. On the other

hand, the PVDF sensor does not produce nonminimum phase zeros, is very linear, and due to its large coverage area the distributed strain signal is well correlated with acoustic performance.

Some work in the area of self sensing piezoelectric actuators has focused on improving the tuning qualities of the circuit in the presence of the amplitude nonlinearity. [van Schoor, Lengyel & Spangler, 1996] This work was successful at keeping the pole-zero structure of the transfer function constant over various input voltages, but the overall gain of the transfer function is not constant. This would still result in closed-loop stability problems using a linear control design method. A nonlinear or multi-model type controller may alleviate this problem, but requires a more complex design.

Chapter 6

CONCLUSIONS

The three goals of this research were to create a high-fidelity finite element model of the acoustic chamber; determine the capabilities and limitations of this model for the design of shaped and distributed sensors and actuators; and determine the capabilities and limitations of the model for predicting the closed loop structural acoustic performance. Each of these goals has been achieved, and the results will be summarized in this chapter.

6.1 Summary

A coupled structural acoustic finite element model of the test chamber was created using commercial FEM software (ANSYS). A modal state space method using the uncoupled structural and acoustic modes was found to be accurate for this problem, and more computationally efficient than solving the unsymmetric finite element equations. Various sensors and actuators were added to the state space model, and where appropriate, simplifying assumptions were made regarding their dynamics. All of the assumptions made in the modeling process were validated by correlating the finite element model to experimental data.

Results from the finite element model were used in the design of both a modally shaped PVDF sensor, and distributed PZT sensuator. In both cases, the sensor/actuator design was determined to be very sensitive to unmodeled but tolerated manufacturing and boundary condition uncertainties. For the PVDF sensor, a mild warp in the aluminum plate

resulted in an undesired observability of the third symmetric plate mode. Otherwise, the sensor response was as predicted and useful in a high performance acoustic transmission compensator. For the distributed PZT sensuator, warp and/or boundary condition uncertainty resulted in very low observability of the plate mode that the sensuator was designed improve. This rendered the distributed sensuator useless for high performance transmission control.

The limitations encountered were disappointing; however, since they are likely due to discrepancies that will be present between any analytic model and actual hardware, they provide useful guidelines for the use of a finite element model in sensor and actuator design. First, since shaped or distributed sensors and actuators were found to be sensitive to the dynamic modeshapes or nodelines, the critical nodelines should be verified experimentally as much as possible prior the final choice of shape or placement. Unfortunately, this is often not entirely possible since bonding the sensor or actuator will likely change the nodelines (especially in the case of PZT wafers), but any modeshape correlation is better than none. Second, using both shaped and/or distributed sensors and actuators (like the distributed sensuator) compounds the sensitivity to modeshape. Since the desirable transfer function properties (modal filtering, rolloff and bounded phase) can be achieved through either actuator or sensor design, it is recommended that only one be used. This imposes a very strict, practical limitation on any distributed sensuator design.

The finite element model was next used to predict the closed-loop response of several sensors and actuators for transmission and reflection control. For the most part, this was successful since the predicted broadband and narrowband attenuation, and regions of acoustic amplification agreed with experimental results. The predictions of course were not perfect, but they demonstrated that the finite element model can be a useful tool for predicting closed-loop response.

Finally, a transmission compensator using the PZT actuator with a shaped PVDF sensor was compared to one using the single wafer PZT sensuator. Comparing the two designs is

useful since the first offers modal filtering, and the second offers perfectly bounded phase. The finite element model predicts slightly better performance from the shaped PVDF sensor design. This prediction is verified by comparing experimental results from the PVDF sensor compensator to another prediction achieved by convolving the PZT sensuator compensator with experimental data. Implementation of the PZT sensuator compensator revealed severe stability problems due to amplitude nonlinearity. The best implemented performance in the presence of this nonlinearity was much less than predicted.

The amplitude nonlinearity of the sensuator imposes another strict, practical limitation on its use in feedback control. This nonlinearity must either be reduced by modifying the reference leg of the sensuator circuit to better track the piezo capacitance, or nonlinear control techniques must be employed. The nonlinearity, along with the compounded sensitivity to modeshape uncertainty leads to the conclusion that the sensuator design used for this research is not a practical choice for high performance acoustic transmission control. A modally shaped PVDF sensor used in conjunction with a PZT wafer located for maximum actuation of all modes in the control bandwidth is a very good choice for transmission control.

6.2 Recommendations for Future Work

This research has dealt with utilizing a finite element model in the sensor and actuator design for structural acoustic control. To this point, it has been limited to a simplified experimental setup composed of an essentially one-dimensional acoustic enclosure with a two-dimensional structure. Also, the control design has focused primarily on acoustic transmission.

Two recommended paths for continued research in the area of sensor and actuator design and modeling for acoustic control in payload fairings are: 1) extension of the transmission work to an actual (or scale) payload fairing geometry; and 2) design of a structurally collocated acoustic sensor and actuator for reflection control in the one-dimensional chamber.

The first path should follow the same steps used for this research, with consideration to the limitations and conclusions presented. A high-fidelity finite element model of the scale payload fairing will be useful for determining the approximate shape and location of sensors and actuators. Since modeshape discrepancies similar to those encountered in this thesis are likely, the critical nodelines should be verified experimentally prior to deciding the final sensor and actuator shape and location.

The second path could build upon the secondary membrane approach described in Appendix C. This seems promising from the point of observability of the acoustic modes through the membrane vibration; however, actuation authority using PVDF on an inflated membrane may not be adequate. Other options include using the PVDF in a passive shunting circuit, or a piezoceramic stack as a differential displacement actuator between the membrane and plate.

REFERENCES

[Anderson, 1968] Anderson, Brian D. O., "A Simplified Viewpoint of Hyperstability", *IEEE Transactions on Automatic Control*. AC-13, No. 3, June 1968, pp. 292-294.

[Anderson & Hagood, 1994] Anderson, E.H. and N.W. Hagood, "Simultaneous Piezoelectric Sensing/Actuation: Analysis and Application to Controlled Structures", *Journal of Sound and Vibration*, Vol. 174, 1994, pp. 617-639.

[ANSYS Users Manual, 1992] Swanson Analysis Systems, Inc., *ANSYS Users Manual Revision 5.0*, 1992.

[Asari, 1998] Asari, K., *Vibroacoustic Modeling and Control for Launch Vehicle Shrouds*, Master's thesis, Massachusetts Institute of Technology, 1998.

[Blaurock,1998] Blaurock, C., "PVDF Modal Accentuation Sensor", 1998.

[Blevins, 1979] Blevins, R. D., *Formulas for Natural Frequency and Mode Shape*, Robert E. Krieger Publishing Company, 1979.

[Clark & Fuller, 1992] Clark, Robert L. and Chris R. Fuller, "Optimal Placement of Piezoelectric Actuators and Polyvinylidene Fluoride Erroe Sensors in Active Structural Acoustic Control Approaches", *Journal of the Acoustical Society of America*, Vol. 92, 1992, pp. 1521-1533.

[Craig, 1981] Craig, R.R., *Structural Dynamics An Introduction to Computer Methods*, Wiley, New York, 1981.

[Crawley, Campbell & Hall, 2000] Crawley, Edward F., Mark E. Campbell and Steven R. Hall, *High Performance Structures: Dynamic and Control*, Cambridge University Press, pre-print from MIT 16.243 notes to be published 2000.

[Denoyer, et al., 1998] Denoyer, Keith K., Steven F. Griffin, and Dino Sciulli, "Hybrid Structural/Acoustic Control of a Sub-Scale Payload Fairing", *Proceedings, SPIE Conference on Smart Structures and Integrated Systems*, (San Diego, CA), March 1998, pp. 237-243.

[Falangas, et al., 1994] Falangas, Eric T., J.A. Dworak and Shozo Koshigoe, "Controlling Plate Vibrations Using Piezoelectric Actuators", *IEEE Control Systems*, August 1994, pp. 34-41.

[Freudenberg & Looze, 1985] Freudenberg, James, S. and Douglas P. Looze, "Right Half Plane Poles and Zeros and Design Tradeoffs in Feedback Systems", *IEEE Transactions on Automatic Control*, AC-30, No. 6, June 1985, pp. 555-565.

[Fuller & Gibbs, 1994] Fuller, C.R. and G.P. Gibbs, "Active Control of Interior Noise in a Business Jet Using Piezoceramic Actuators", *Proceedings, Noise-Con 94*, (Ft. Lauderdale, FL), May 1994, pp. 389-394.

[Fuller, et al., 1989] Fuller, C.R., V.L. Metcalf, R.J. Silcox, and D.E. Brown, "Experiments on Structural Control of Sound Transmitted Through an Elastic Plate", *Proceedings, American Control Conference*, (Pittsburg, PA), June 1989, pp. 2079-2084.

[Gere and Timoshenko, 1990] Gere, J.M. and S.P. Timoshenko, *Mechanics of Materials*, PWS-Kent, Boston, 1990.

[Glaese, 1994] Glaese, R.M., *Development of Zero-Gravity Structural Control Models from Analysis and Ground Experimentation*, Master's thesis, Massachusetts Institute of Technology, 1994.

[Glaese, 1997] Glaese, R.M., *Impedance Matching for Sructural-Acoustic Control*, Ph.D. thesis, Massachusetts Institute of Technology, 1997.

[Griffin & Denoyer, 1997] Griffin, Steven F. and Keith K. Denoyer, "Experimental Sensor and Actuator Location Procedure for Control of Dynamically Complex Smart Structures", *Proceedings, SPIE Conference on Smart Structures and Integrated Systems*, (San Diego, CA), March 1998, pp. 717-723.

[Griffin & Henderson, 1997] Griffin, S. and B. Henderson, "An Investigation into Inaccuracies in Closed-Form Piezoceramic Actuator Models For Smart Structures", *Proceedings, AIAA Structures, Structural Dynamics, and Materials Conference*, (Kissimmee, FL), April 1997. AIAA Paper 97-1309.

[Grocott, 1997] Grocott, S.C.O., *Dynamic Reconstruction and Multivariable Control for Force-Actuated, Thin Facesheet Adaptive Optics*, Ph.D. thesis, Massachusetts Institute of Technology, 1997.

[Hildebrand, 1976] Hildebrand, Francis B., *Advanced Calculus for Applications*, Prentice-Hall, 1976.

[Ko & Tongue, 1995] Ko, B. and B. H. Tongue, "Acoustic Control using a Self-Sensing Actuator", *Journal of Sound and Vibration*, Vol. 187, 1995, pp. 145-165.

[Koshigoe et al., 1993] Koshigoe, S., J. Gillis, and E. Falangas, "A New Approach for Active Control of Sound Transmission Through an Elastic Plate Backed by a Rectangular Cavity", *Journal of the Acoustical Society of America*, Vol. 94, 1993, pp. 900-907.

[Leo & Anderson, 1996] Leo, Donald J, and Eric H. Anderson. "Vibroacoustic Modeling of a Launch Vehicle Payload Fairing for Active Acoustic Control". *Proceedings,*

AIAA Structures, Structural Dynamics, and Materials Conference, (Long Beach, CA), April1998, pp. 3212-3222. AIAA Paper 98-2086.

[Lublin & Athans, 1996] Lublin, Leonard, and Michael Athans, *Linear Quadratic Regulator Control*, in The Control Handbook, CRC Press Inc., 1996.

[Makarenko & Crawley, 1998] Makarenko, Alexi A. and Edward F. Crawley, *Force and Strain Feedback for Distributed Actuation*, Master's thesis, Massachusetts Institute of Technology, 1998.

[Masters & Crawley, 1997] Masters, Brett P. and Edward F. Crawley, Evolutionary Design of Controlled Structures, Sc.D. thesis, Massachusetts Institute of Technology, 1997.

[O'Sullivan, 1998] O'Sullivan, Donald Quinn, *Aircraft Interior Structural Acoustic Control Design*, Master's thesis, Massachusetts Institute of Technology, 1998.

[Spangler, 1994] Spangler, Ronald L. Jr., *Broadband Control of Structural Vibration Using Simultaneous Sensing and Actuation with Nonlinear Piezoelectric Elements,* Ph.D. thesis, Massachusetts Institute of Technology, 1994.

[Strang, 1986] Strang, Gilbert, *Introduction to Applied Mathematics*, Wellesley-Cambridge Press, 1986.

[Vadali & Das, 1996] Vadali, S. and A. Das, "Active Control of Structural-Acoustic Systems: Noise Reduction in Payload Fairings", *Proceedings, AIAA Guidance, Navigation and Control Conference*, (San Diego, CA), July 1996. AIAA Paper 96-3756.

[van Schoor, Lengyel & Spangler, 1996] van Schoor, M.C., A. Lengyel and R. Spangler, *Self-Sensing Piezoelectric Actuator: Phase 1 Final Report*, Mide Technology Corp., 1996.

[Wang, et al., 1994] Wang, Bor-Tsuen, Ricardo A. Burdisso and Chris R. Fuller, "Optimal Placement of Piezoelectric Actuators for Active Structural Acoustic Control, *Journal of Intelligent Material Systems and Structures*, Vol. 5, 1994, pp. 67-77.

Appendix A

FINITE ELEMENT MODEL MODESHAPES

A.1 Uncoupled Modeshapes

The following figures show the uncoupled modeshapes of acoustic chamber up to 1000 Hz. The shapes are visualized as displacement plots of the circular aluminum plate, or pressure contours of a cross section through the acoustic chamber. The structural modes are grouped by symmetric (i.e. no nodal diameters) and asymmetric. The asymmetric modes actually occur in pairs with the nodal diameters rotated 90°. Only one of the two asymmetric plate modes are shown for visualization.

A.1.1 Structural

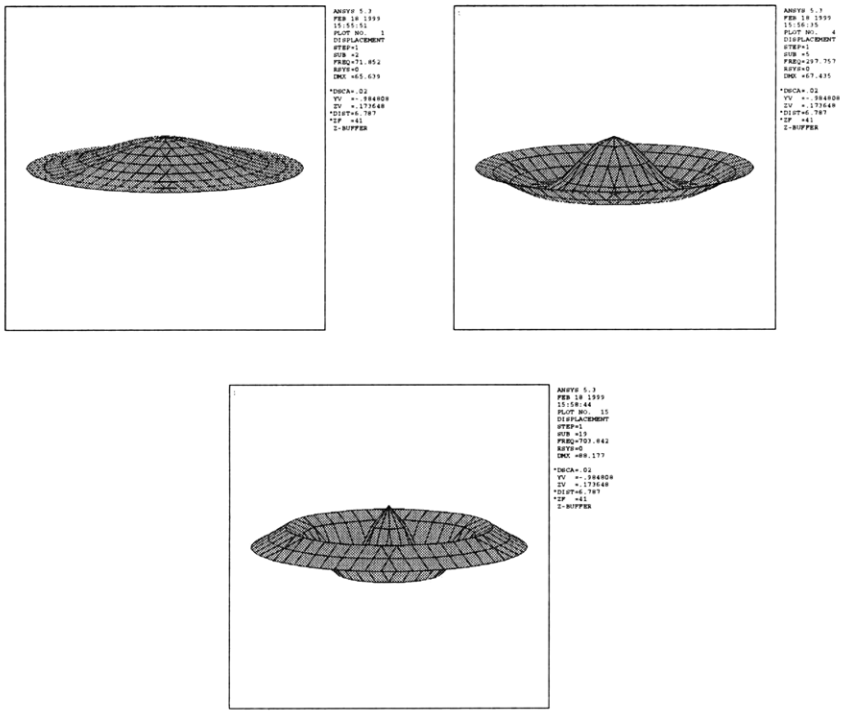

Figure A.1 Plate axisymmetric modes for uncoupled finite element model.

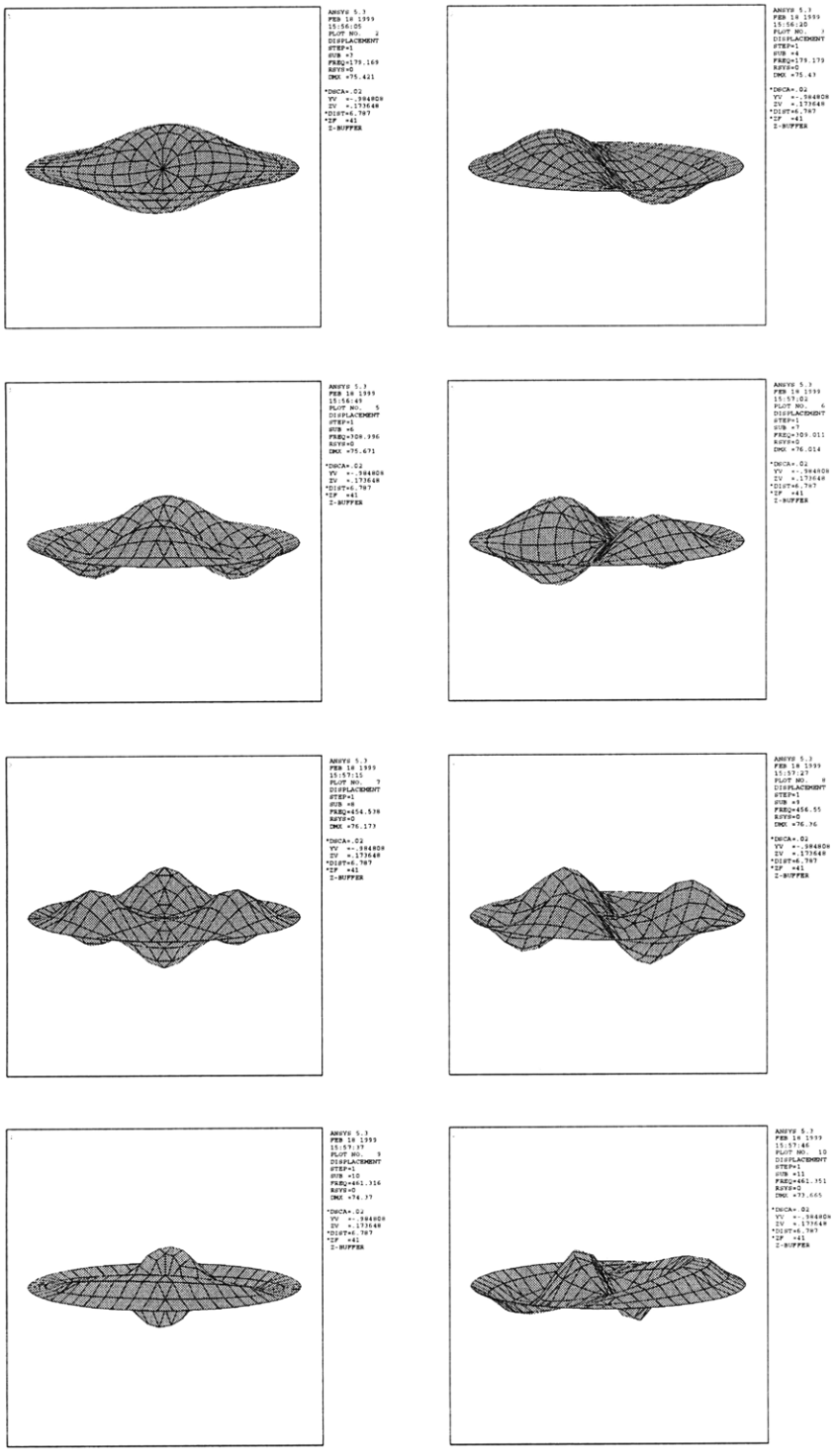

Figure A.2 Plate asymmetric modes for uncoupled finite element model.

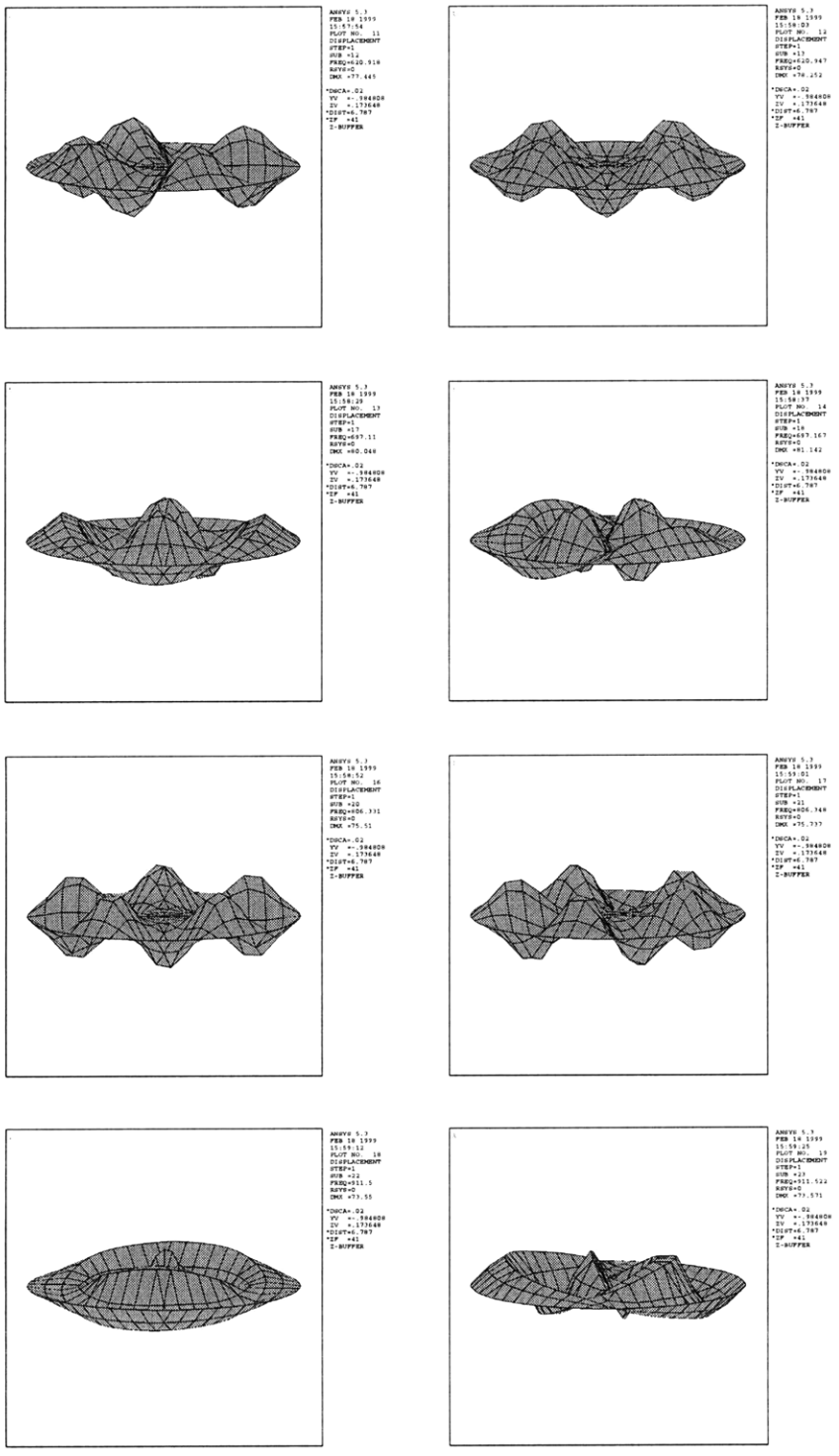

Figure A.2 Plate asymmetric modes for uncoupled finite element model.

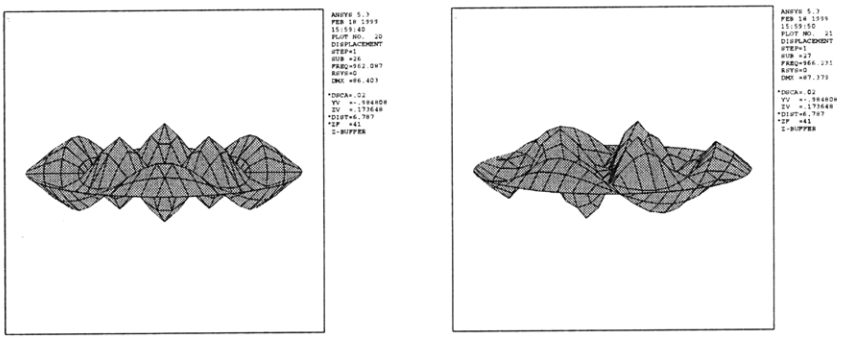

Figure A.2 Plate asymmetric modes for uncoupled finite element model.

A.1.2 Acoustic

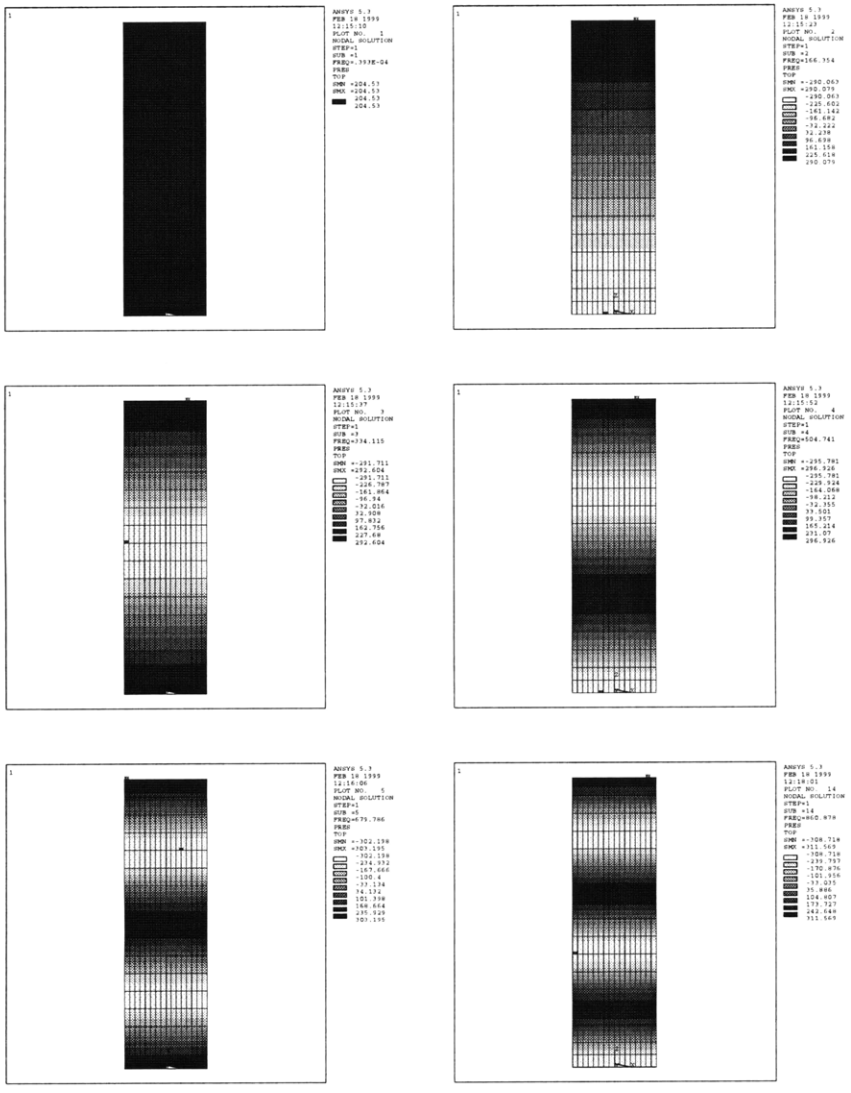

Figure A.3 Lower chamber longitudinal acoustic modes for uncoupled finite element model.

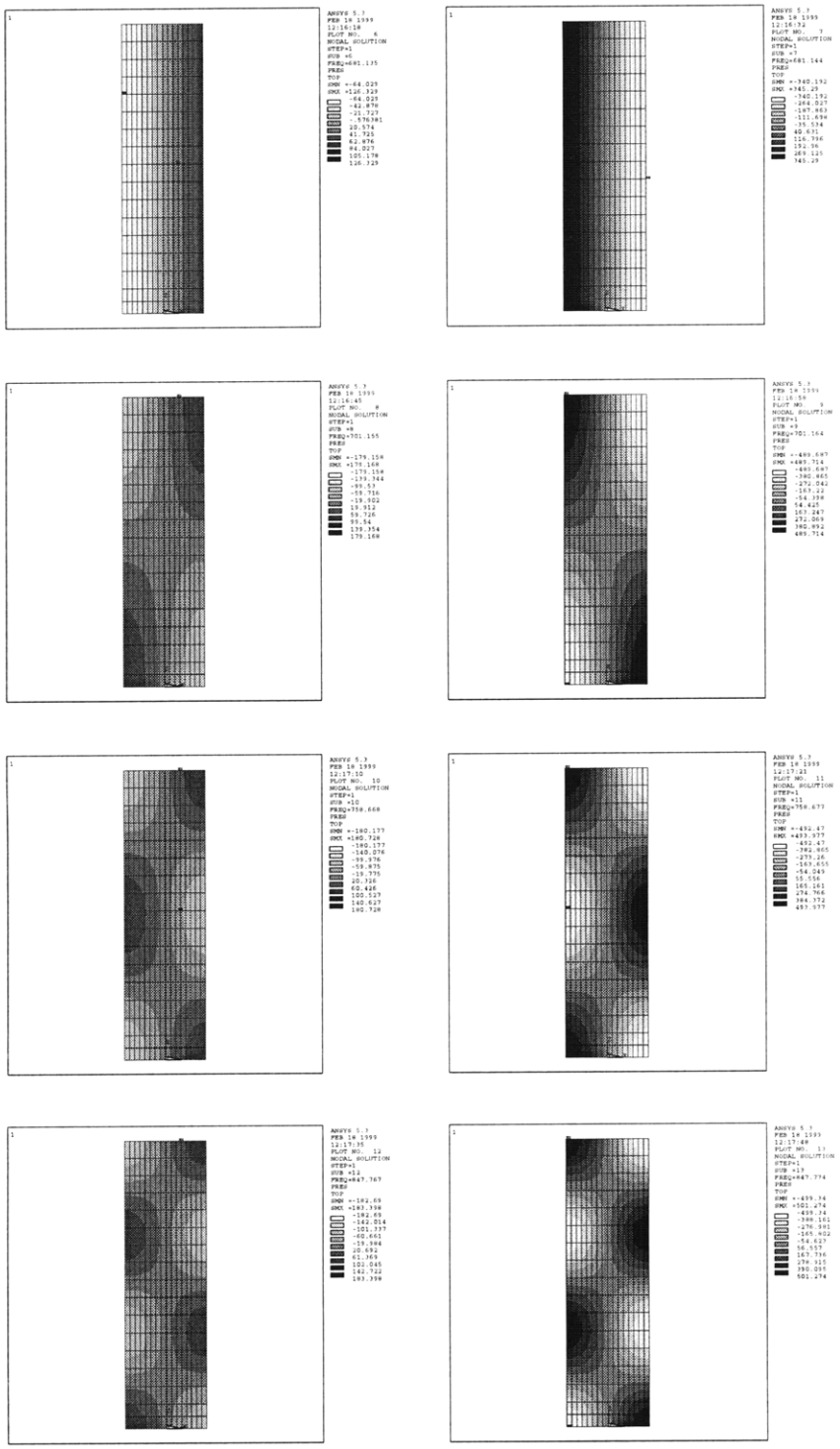

Figure A.4 Lower chamber transverse acoustic modes for uncoupled finite element model.

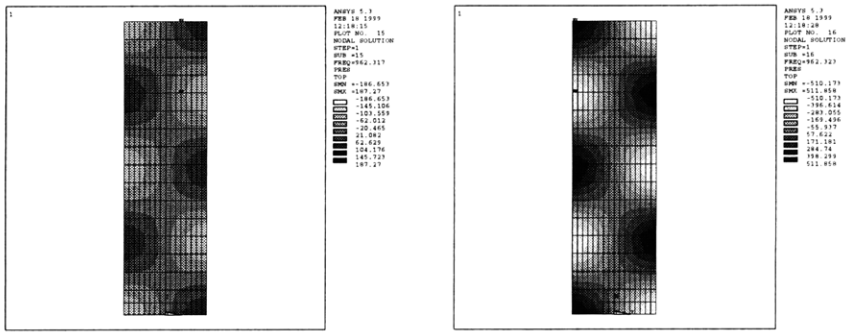

Figure A.4 Lower chamber transverse acoustic modes for uncoupled finite element model.

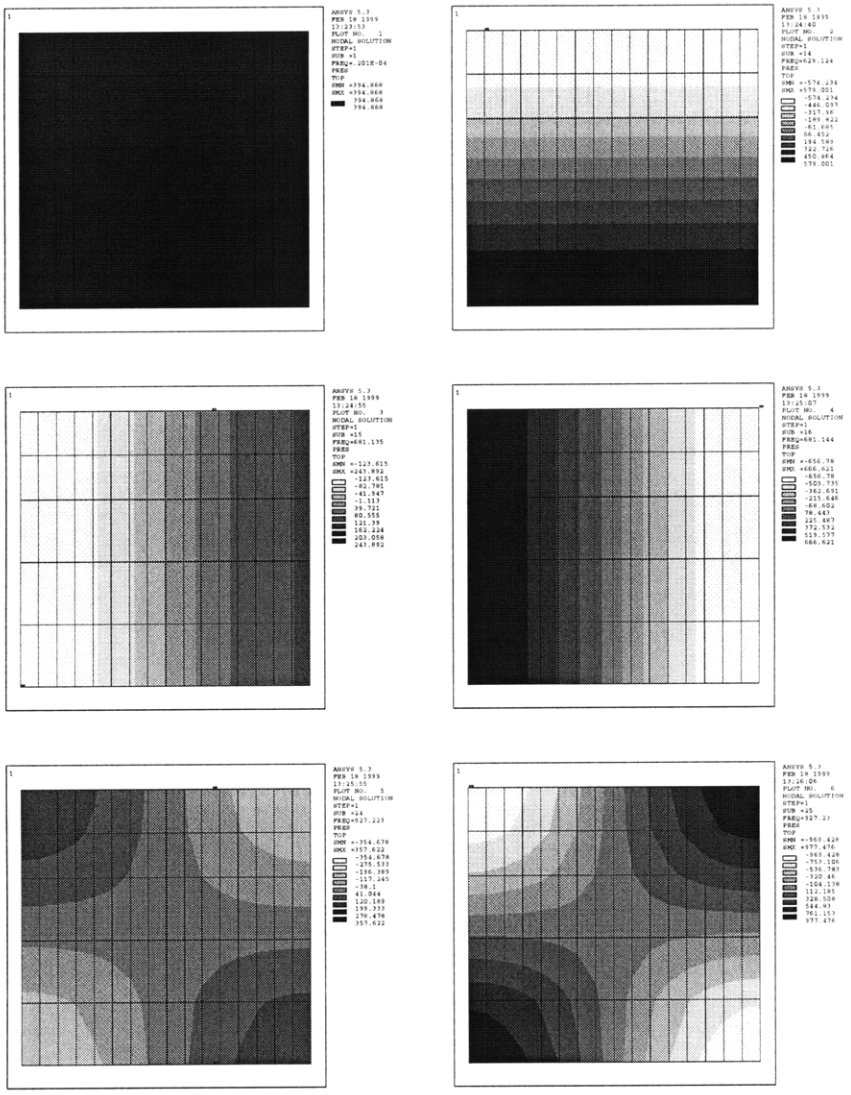

Figure A.5 Upper chamber acoustic modes for uncoupled finite element model.

A.2 Coupled Modeshapes

The following figures show the coupled modeshapes of acoustic chamber up to 1000 Hz. The shapes are visualized by the vertical displacement along a plate diameter, and the corresponding pressure along the centerline of the lower acoustic chamber. They are grouped by structural modes and acoustic modes based on their resemblance to the uncoupled modeshapes.

A.2.1 Structural

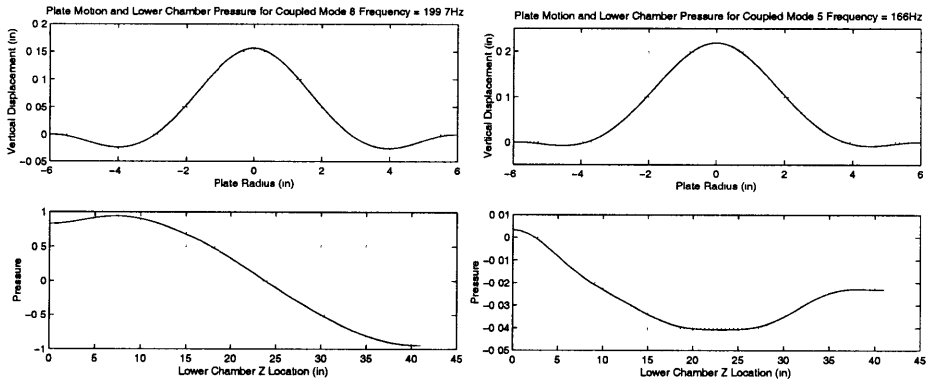

Figure A.6 Bottom and top chamber speaker modes for coupled finite element model.

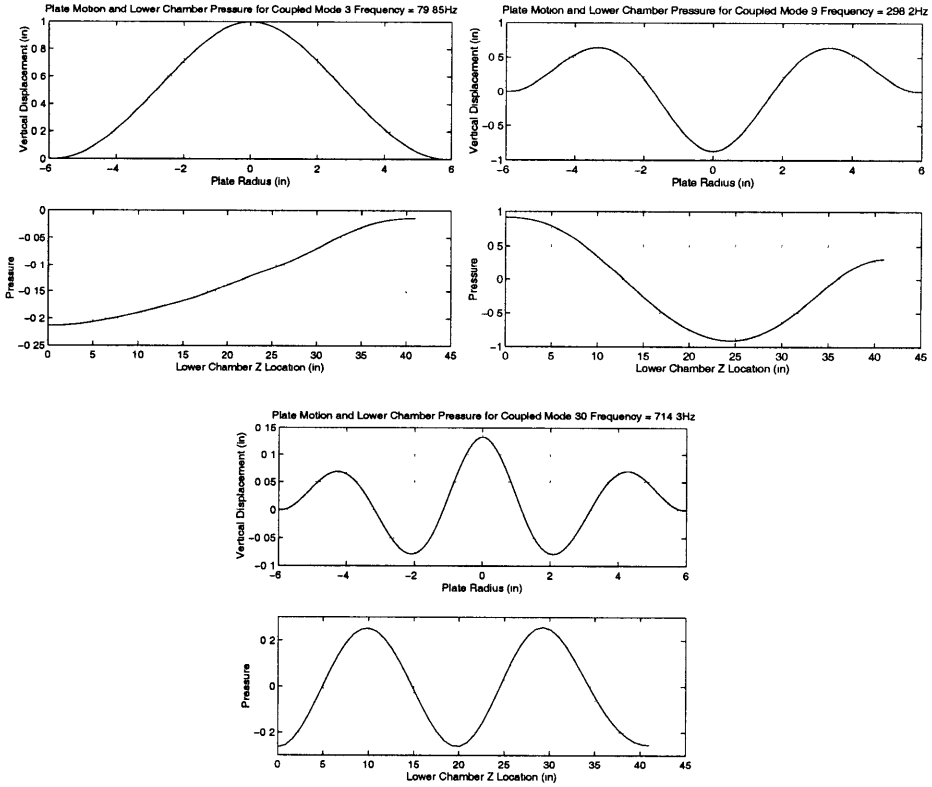

Figure A.7 Plate axisymmetric modes for coupled finite element model.

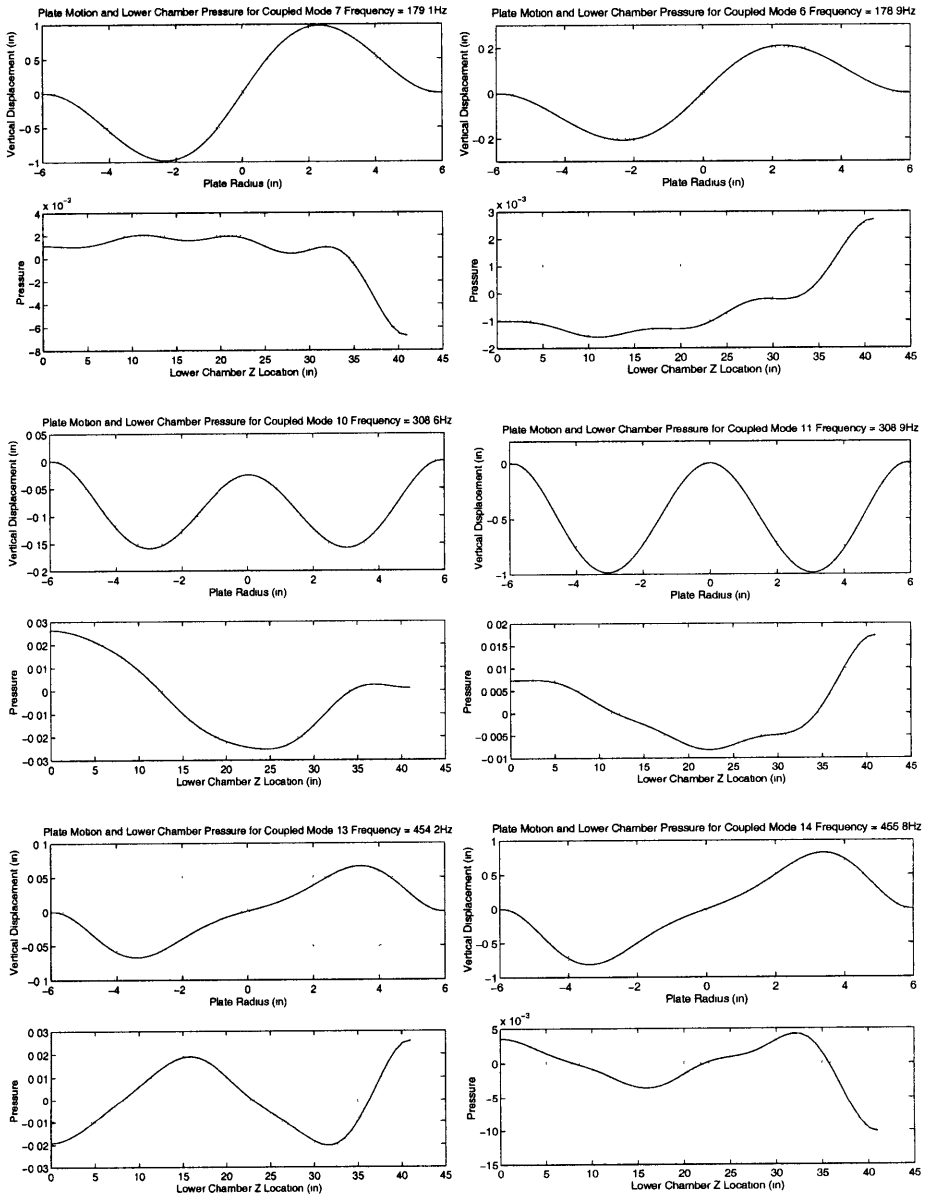

Figure A.8 Plate asymmetric modes for coupled finite element model.

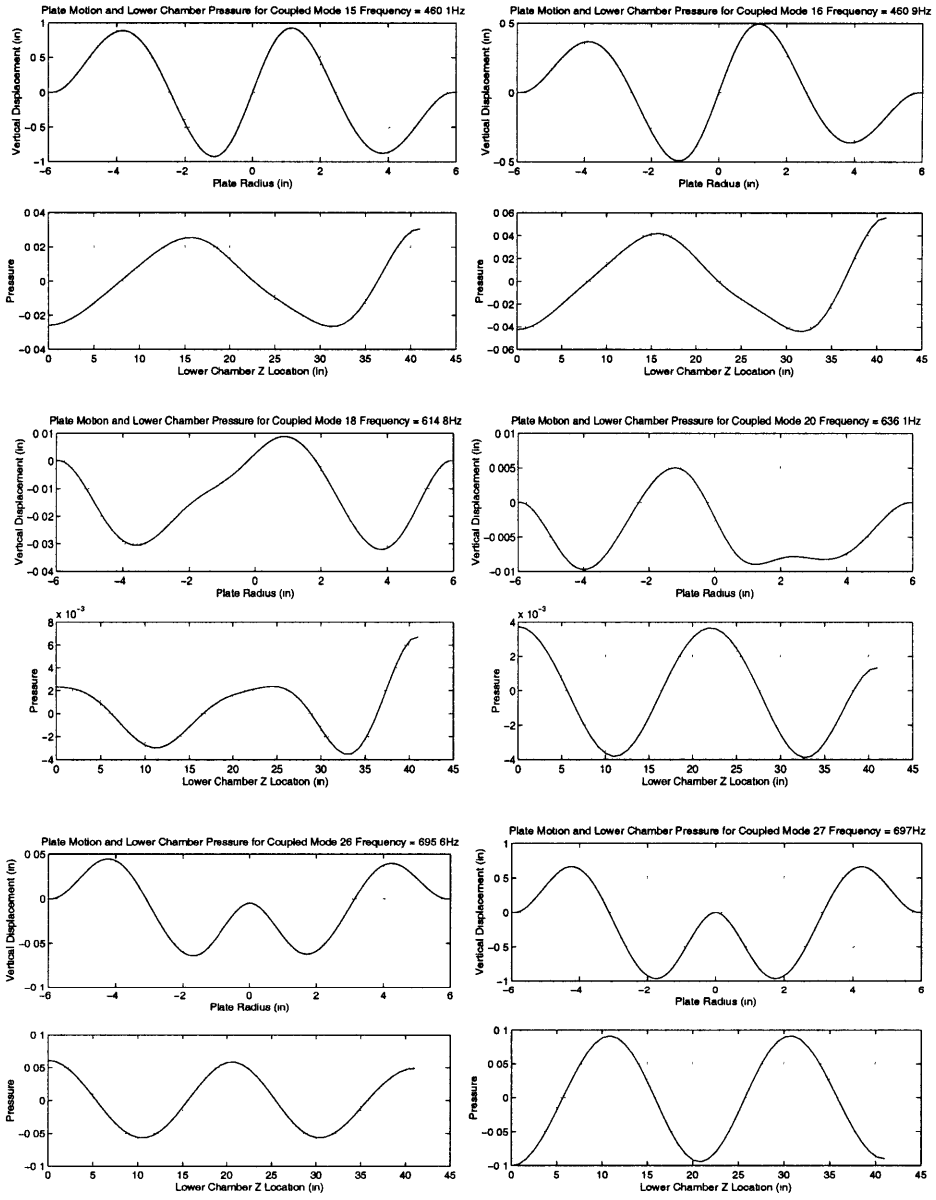

Figure A.8 Plate asymmetric modes for coupled finite element model.

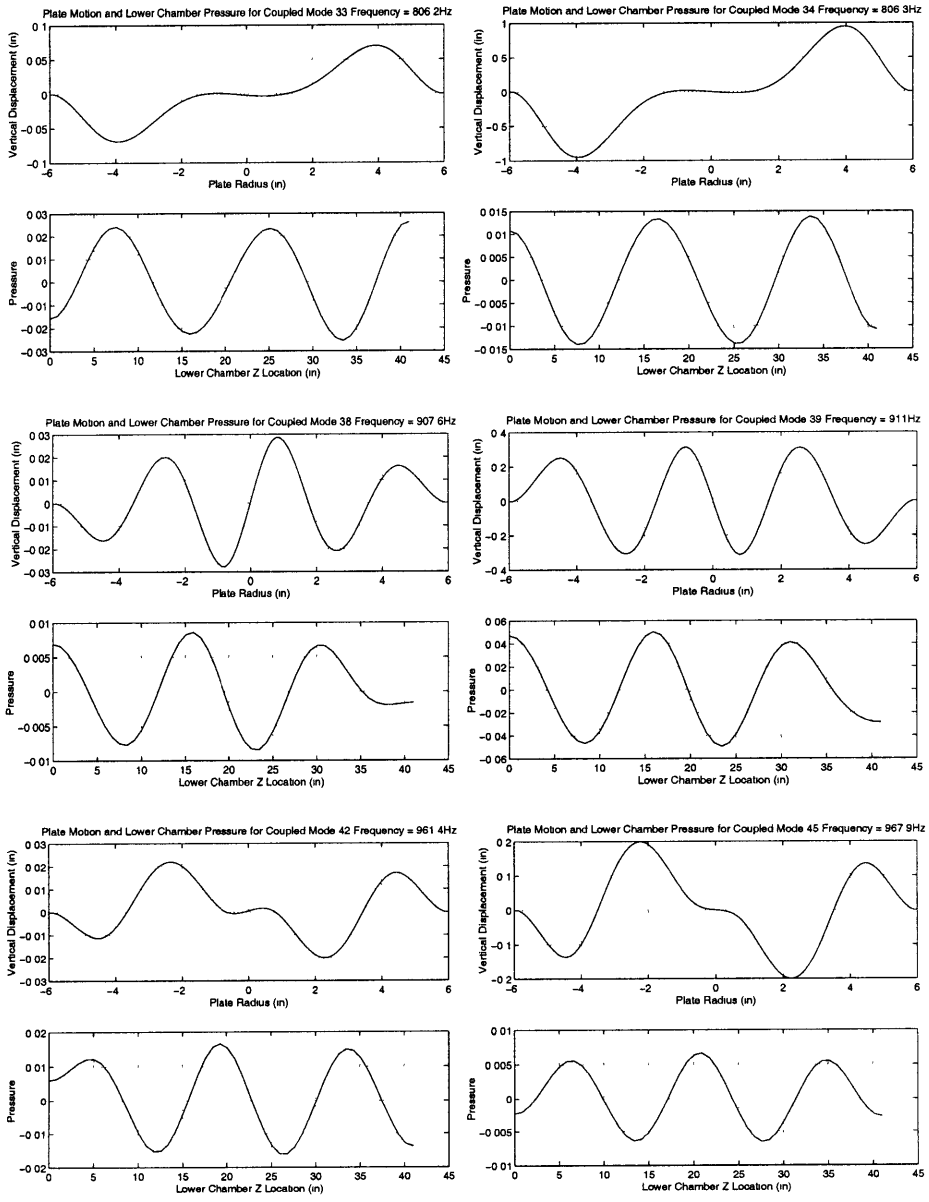

Figure A.8 Plate asymmetric modes for coupled finite element model.

A.2.2 Acoustic

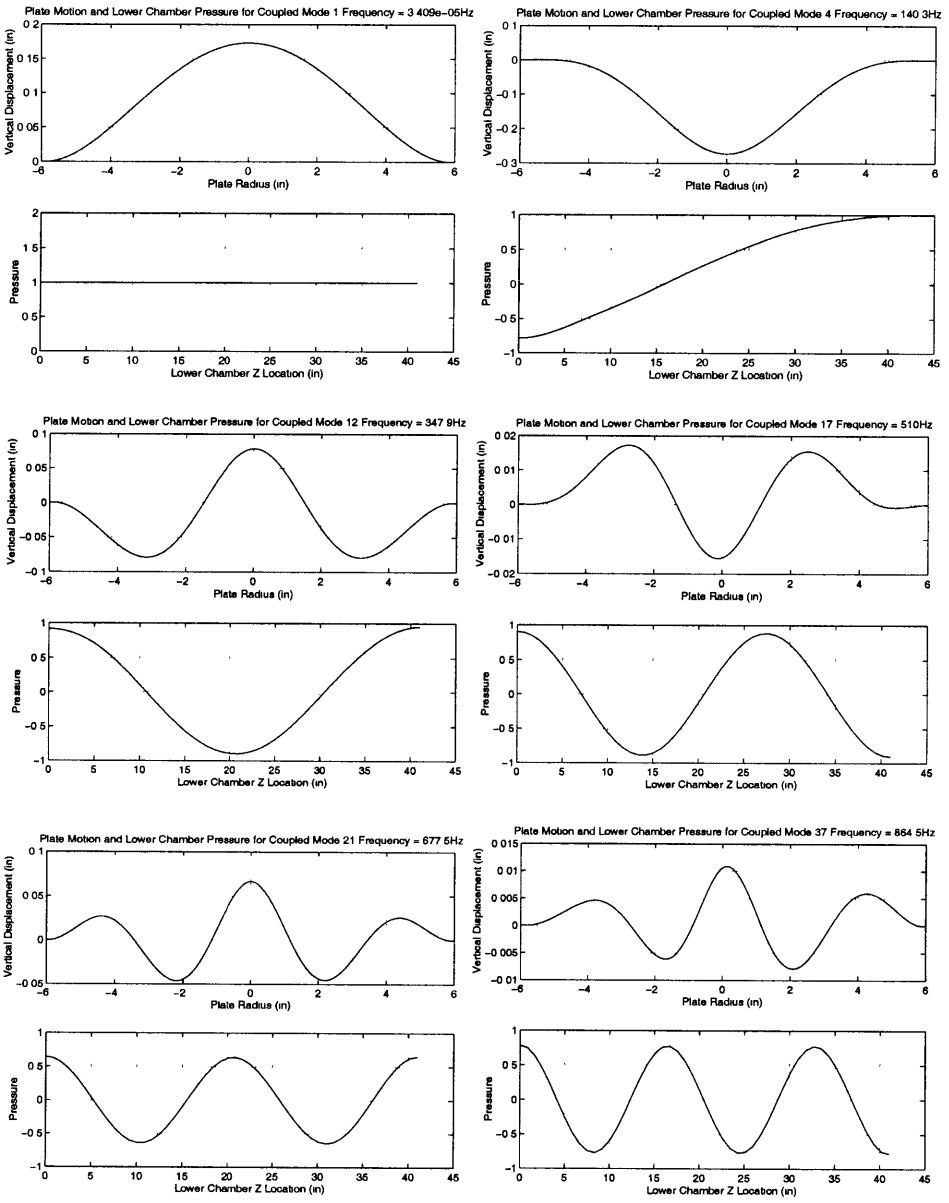

Figure A.9 Lower chamber longitudinal acoustic modes for coupled finite element model.

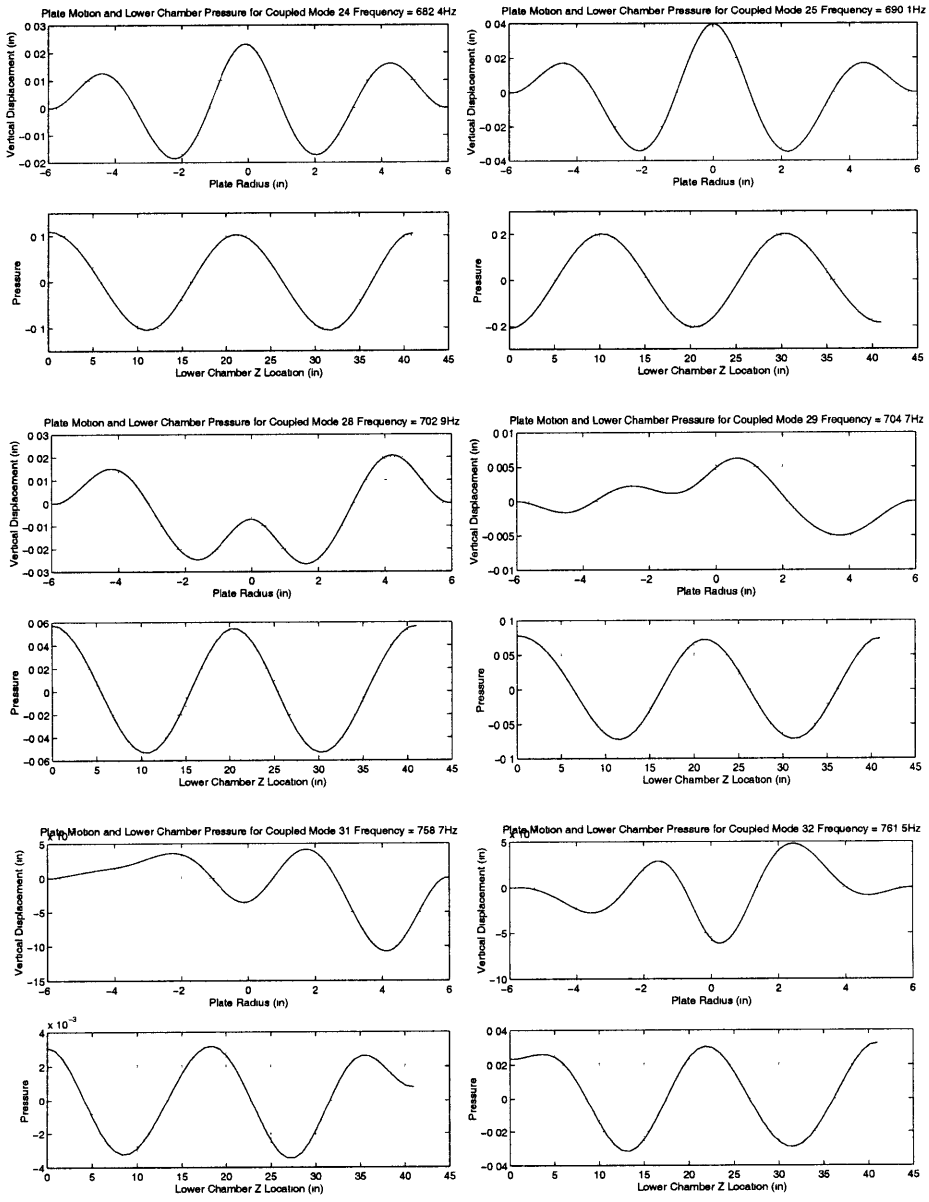

Figure A.10 Lower chamber transverse acoustic modes for coupled finite element model.

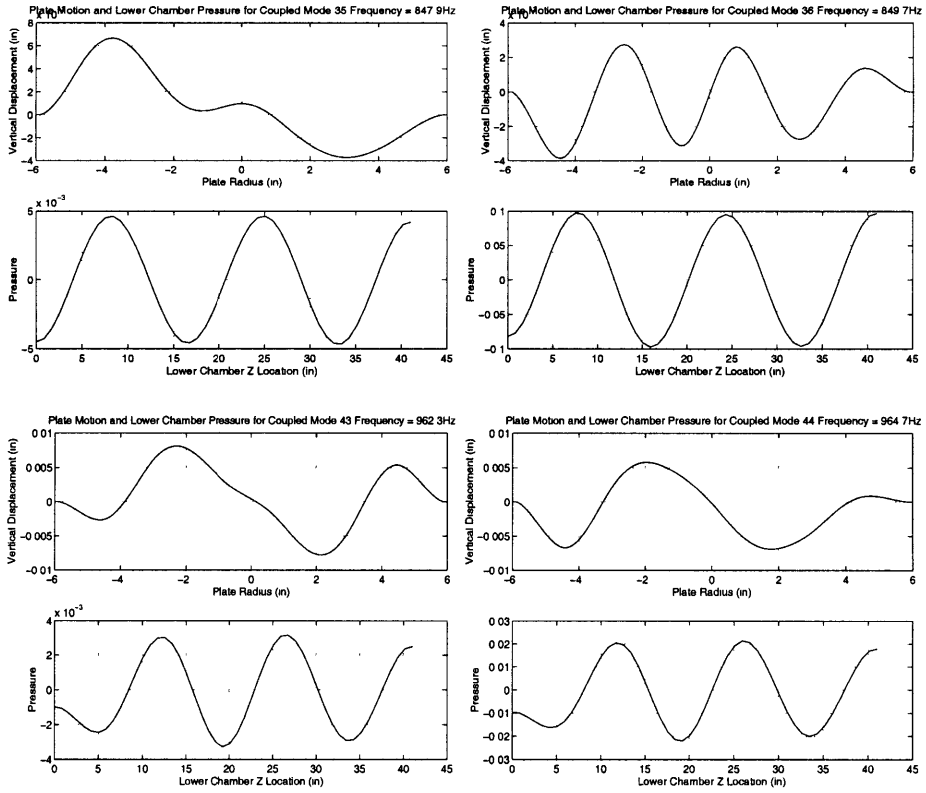

Figure A.10 Lower chamber transverse acoustic modes for coupled finite element model.

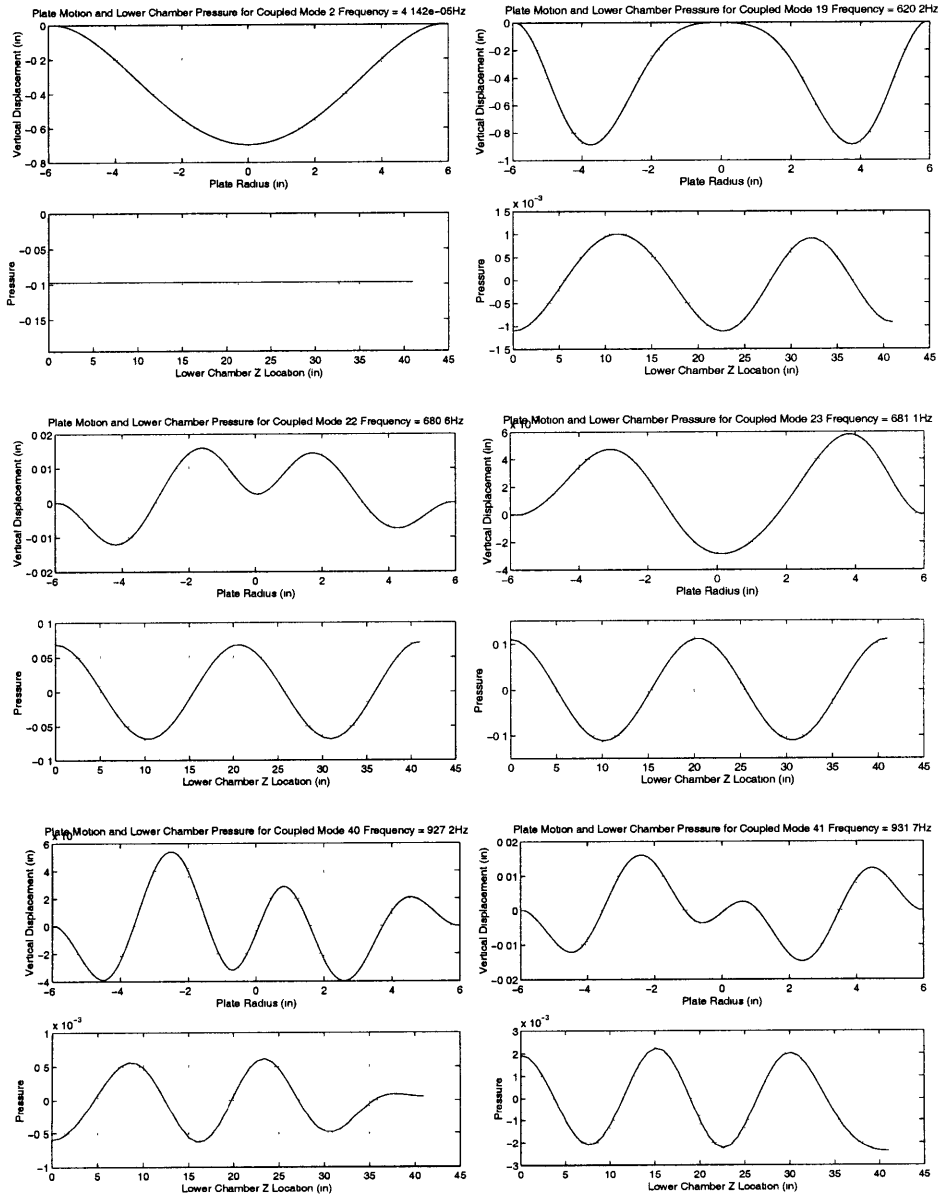

Figure A.11 Upper chamber acoustic modes for coupled finite element model.

Appendix B

INVESTIGATION OF CIRCULANCE

Circulance is a method of modeling and arranging the matrix equations of a circularly symmetric system which allows the matrices to be transformed into several smaller decoupled systems. The obvious advantage of this method is that the computational cost of solving several smaller systems is significantly less than solving a single large system. The disadvantage of the method is that it is only applicable to systems that are circularly symmetric (e.g. all cross sections about a single axis are circular). Controlled structures applications to this point have also restricted usage to systems where all the sensors and actuators share this same circular symmetry with the structure. For these applications, it has proven to be a useful method for reducing the computational cost of both the modeling and control design. [Grocott, 1997, O'Sullivan, 1998]

Structural acoustic control of launch vehicle fairings is an application where the circular symmetry of the structure and the distributed nature of the sensors and actuators may lend itself well to the use of circulance. It is also suggested that in some situations it is possible to relax the requirement of sensor and actuator symmetry. This relaxed method is outlined below, and its advantages and disadvantages are discussed.

The relaxed method applies to systems where the mass and stiffness properties of asymmetric sensors and actuators can either be neglected, or approximately modeled with circular symmetry (e.g. the mass and stiffness of a rectangular PZT wafer at the center of a circular plate may be added over a circular area without much loss of fidelity). Circulance

can then be used to reduce the cost of computing the eigenvalues and eigenvectors used to form a modal state space model. The asymmetric output and forcing of the sensors and actuators can then be added to the state space model as was done for the modeling in this thesis.

The advantage of the relaxed method is that it extends the application of circulance to symmetric controlled structures with non-symmetric sensors and actuators (if the passive effect of the sensors and actuators can be neglected or modeled in a circulant manner as described above). In addition, the distribution of the sensors and actuators in a structure often defines the number of planes of symmetry. With this relaxed method, it may be possible to increase the number of planes of symmetry by neglecting or appropriately approximating the mass and stiffness contribution of the sensors and actuators. The larger the number of planes of symmetry, the greater the computational savings of the circulance method.

The disadvantage of the relaxed method is that it requires careful modeling to ensure that inappropriate approximations are not made. More significantly, since the relaxed method is only used to model the system, the advantages of circulance cannot be carried into the control design stage. Although approximating the mass and stiffness contribution of sensors and actuators may be a valid modeling practice, approximating their forcing and sensing capabilities introduces much greater errors. Returning to the example of the PZT on the aluminum plate, approximations were made to the passive contribution of the PZT to the plate; however, the actuation capability of the PZT was carefully modeled around the edge of the rectangular patch. This results in a system that is no longer symmetric, and circulance can not be extended to control design.

Another disadvantage of circulance, in general, is that it does not handle models with nodes on the line of circular symmetry. The problem is that these nodes belong to all of the substructures ("wedges"). It seems that the properties of this node could be divided between the circulant "wedges"; however, this presents a problem with maintaining the

consistency of the degrees of freedom through the circulant transformation. The work by O'Sullivan avoided this problem by simply leaving a small hole in the model along the line of symmetry. [O'Sullivan, 1998] Solving this problem could be a topic for continued research in circulance, but is beyond the scope of this project.

Appendix C

ACTIVE MEMBRANE FOR REFLECTION CONTROL

One limitation to applying active structural acoustic control techniques to the reflection problem is that the acoustic modes are not highly observable through the vibration of the structure. This is mostly due to the mass of the structure impeding its vibration above the first structural resonance. This same result forms the basis for adding mass to a payload fairing to increase acoustic transmission loss. In this Appendix, preliminary work on an active membrane which shows promise for application to active reflection control is presented. The membrane used for these experiments is a 0.0025 in. thick Mylar drum head.

C.1 Response of Membrane to Acoustic Excitation

The first experiment using the membrane was conducted to verify that the acoustic modes are indeed observable through the membrane vibration. For this experiment, the membrane was mounted on a drum rim, and placed in the acoustic chamber 41 in. from the bottom speaker. The bottom speaker was used to excite the lower chamber acoustic modes, and the vibration of the membrane was measured using an Endevco 2222C accelerometer. The acoustic pressure was also measured using a microphone collocated with the bottom speaker (0 in.), and a microphone at the top of the chamber (52 in.).

Figure C.1 shows transfer functions to the membrane acceleration and microphone signals with and without the membrane in the chamber. These transfer functions show that the acoustic modes are fairly observable in the accelerometer signal. They also show that

there is little difference in the frequency of the acoustic modes with and without the membrane in the chamber. Table C.1 summarizes the acoustic modes with and without the membrane, and the theoretical (rigid boundary) 1-D frequencies for a 52 in. and 41 in. chamber length. It is apparent that away from the first mode, where the flexible speakers significantly couple with the acoustics, the acoustic modes are very close to the theoretical modes for the 52 in. chamber regardless of the presence of the membrane. This result is very different from the chamber with the aluminum plate, where the plate effectively divided the chamber acoustics into an upper and lower enclosure.

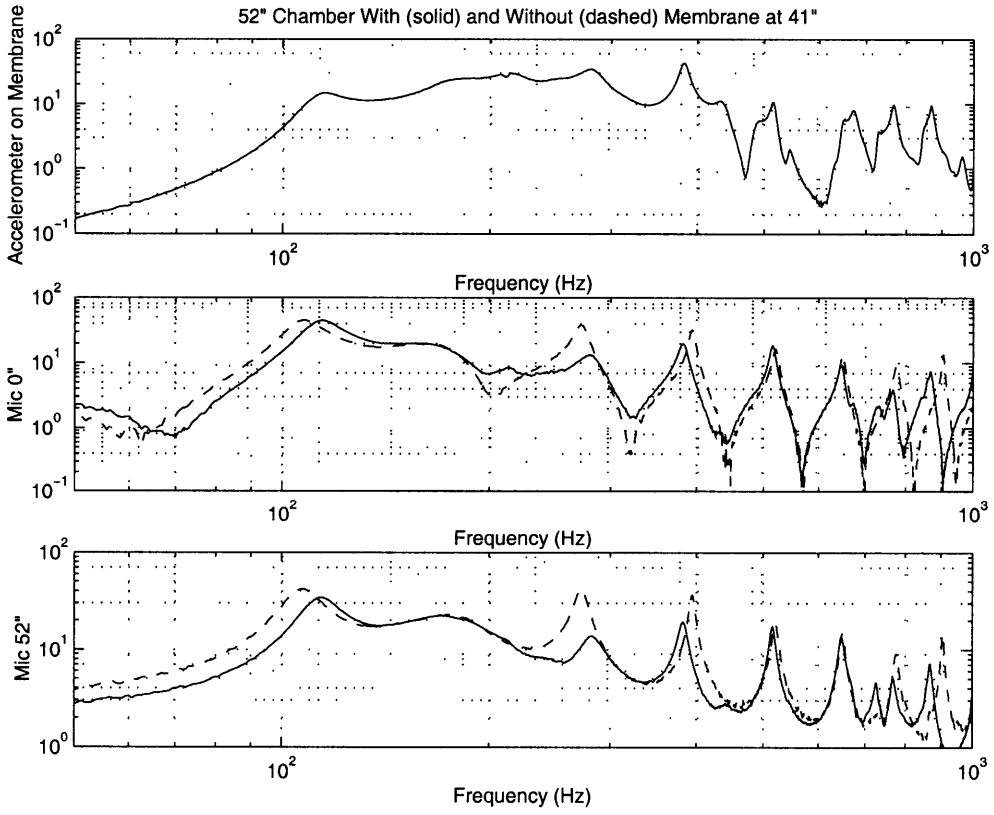

Figure C.1 Transfer functions from bottom speaker to membrane acceleration and microphones with and without membrane dividing chamber.

Another interesting feature of Figure C.1 is that the acoustic mode near 270 Hz is greatly attenuated when the membrane is added to the chamber. The fundamental mode of the

TABLE C.1 Comparison of theoretical and measured acoustic frequencies with and without membrane

Theoretical 41 in. Chamber	Theoretical 52 in. Chamber	Measured w/ Membrane	Measured wo/ Membrane
166.1 Hz	131.0 Hz	115.0 Hz	107.5 Hz
332.2 Hz	262.0 Hz	280.6 Hz	271.3 Hz
498.4 Hz	392.9 Hz	381.9 Hz	393.8 Hz
664.5 Hz	523.9 Hz	515.6 Hz	520.0 Hz
830.6 Hz	654.9 Hz	646.3 Hz	649.4 Hz
996.7 Hz	785.9 Hz	766.3 Hz	776.3 Hz
	916.9 Hz	867.5 Hz	906.3 Hz

membrane appears to be around 210 Hz, therefore its coupling with this acoustic mode is likely the cause for this attenuation. Also, the acoustic modes above 800 Hz appear to be more affected by the presence of the membrane. This is the beginning of a transition region where the mass of the membrane is sufficient to divide the acoustics into a lower and upper enclosure. Finally, many more structural modes are observable in the acceleration of the membrane than were present in the plate acceleration. This is due to a membrane being much more modally dense than a plate, and may present significant challenges for implementing structural control.

C.2 Membrane Actuation

Out-of-plane actuation of the membrane is difficult since the membrane is very thin. Two circular PVDF actuators were bonded to the membrane, and driven out-of-phase to excite the transverse dynamics. This was found to be inefficient, and unpredictable since the amount of in-plane actuation is significant for even small differences between the authority of the two actuators. It is also questionable whether PVDF film on the thin membrane actuates force or strain. A slightly better method is to induce a curvature in the membrane, and use a single PVDF actuator. This actuates force or strain in the curvilinear plane of the membrane and causes out-of-plane motion similar to changing the tension in a sagging string.

The curvature necessary for this actuation can be achieved by applying a small differential pressure between the aluminum plate and the membrane. A circular spacer was cut from a piece of 0.75 in. thick plywood, and a fitting was attached for an air hose. Compressed air was run through a low pressure regulator to supply a constant differential pressure needed to induce curvature. Experiments were performed with the aluminum plate, plywood spacer, and membrane clamped between two 7.5 in. chamber sections in the open chamber configuration shown in Figure C.2.

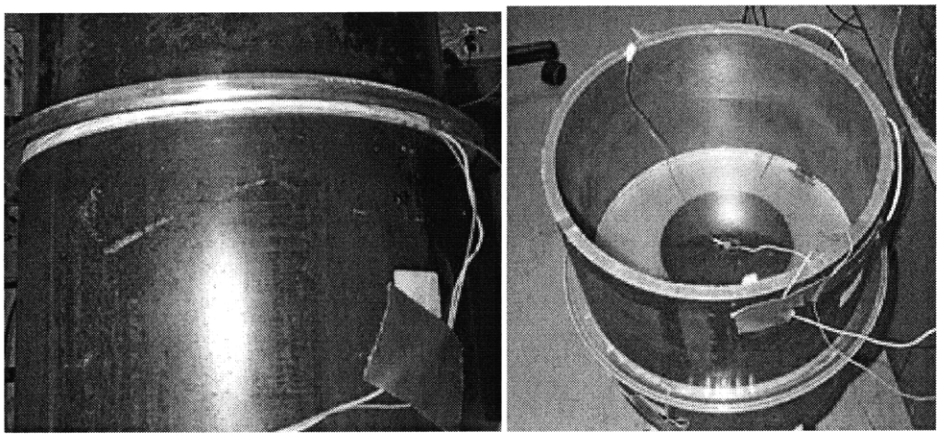

Figure C.2 PVDF actuator on inflated Mylar membrane with plywood spacer in open chamber configuration.

Figure C.3 shows transfer functions from one PVDF actuator to the accelerometer on the membrane and the other PVDF used as a strain sensor with and without a differential pressure. The PVDF signal shows that the transverse dynamics of the membrane are excited better with pressurization than without. This is less obvious in the noisy accelerometer signal; however, the broadband RMS acceleration is increased significantly with pressurization. Table C.2 compares the broadband RMS acceleration and PVDF signal differences between 10 Hz - 1000 Hz for various pressurization levels. The data in this table are normalized to the signal without pressurization.

The trend in Table C.2 is that the PVDF actuates higher out-of-plane broadband RMS acceleration as the pressure differential is increased. The same is true for the PVDF sig-

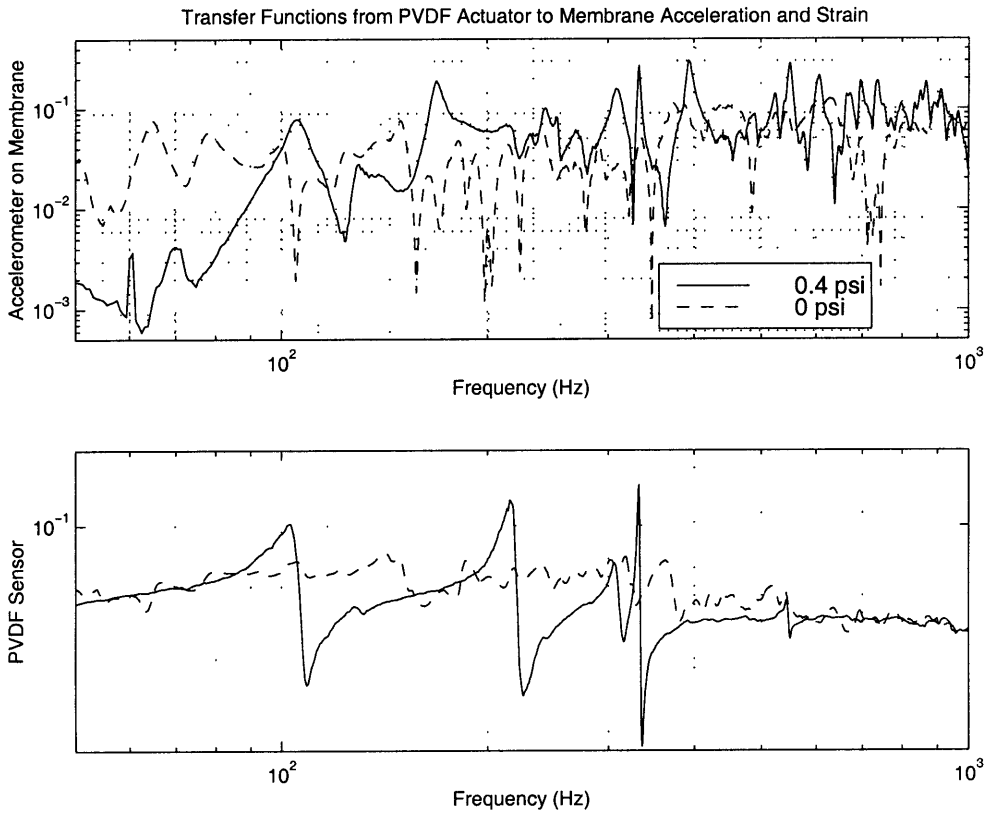

Figure C.3 Transfer functions from PVDF actuator to accelerometer and PVDF sensor for differential pressures between the membrane and aluminum plate.

TABLE C.2 Change in acceleration and PVDF signal with differential pressure

Differential Pressure	Broadband RMS Acceleration	Broadband RMS PVDF Signal
0.1 psi	2.84 dB	-0.74 dB
0.2 psi	2.42 dB	-0.68 dB
0.3 psi	2.69 dB	-0.60 dB
0.4 psi	3.04 dB	-0.51 dB

nal; however, all of this data is less than the nominal signal without pressurization. Without pressurization, the membrane has very little stiffness to resist the in-plane force/strain applied by the PVDF actuator. Pressurization increases the membrane stiffness, thus decreasing the actuation of in-plane strain. The induced curvature increases the actuation

authority for out-of-plane vibration. Extrapolating the PVDF signal to higher pressurization levels shows that 0 dB should be crossed. This is the point where the strain on the surface due to in-plane and out-of-plane actuation are equal. This same stiffening trend is seen in the stiffness dominated region of the acceleration transfer function Figure C.3 below the first fundamental frequency.

In addition to influencing the actuation authority of the membrane, the differential pressure greatly affects the membrane stiffness. This may allow the impedance of the membrane to be matched to the acoustic impedance of the chamber. The impedance match would maximize the conversion of power between the acoustic field and membrane vibration. At this matched condition, power could be dissipated passively (e.g. shunt circuit), or actively using the PVDF sensor/actuator.

Appendix D

COUPLED STRUCTURAL ACOUSTIC WAVE MODEL

A simple wave model of a single degree of freedom oscillator dividing a reverberant acoustic enclosure from an infinite acoustic far-field is developed. This model is used to investigate the effects of passive structural redesign (mass, stiffness and damping), and acoustic damping (blankets) on the acoustic transmission from the far-field to the enclosed field. A sketch of the model is shown in Figure D.1. The waves in the acoustic enclosure are divided into rightward and leftward propagating waves (subscripts r and l) on either side of an arbitrary point, x, where the pressure is to be resolved. The nominal values of the modeling parameters are given in Table D.1.

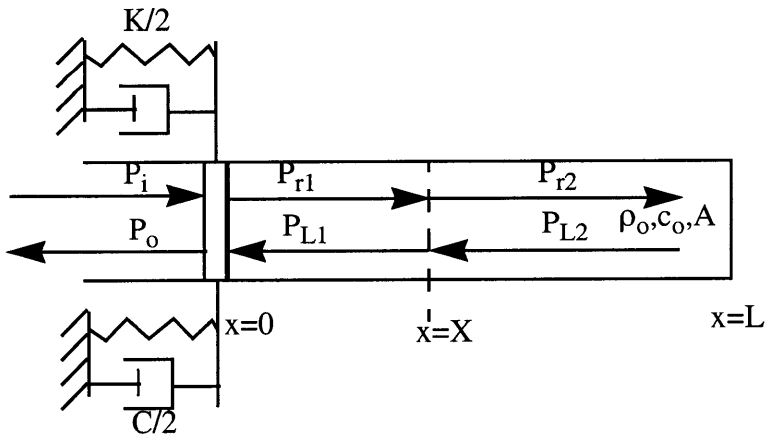

Figure D.1 Wave model of SDOF oscillator dividing reverberant acoustic enclosure and infinite far-field.

TABLE D.1 Nominal parameters of wave model

Variable	Value
M (Mass of Oscillator)	0.159 kg
K (Stiffness of Oscillator)	31643 N/m^2
C (Viscous Damping of Oscillator)	1.4186 N sec/m
ρ_0 (Density of Air)	1.2 kg/m^3
c_0 (Speed of Sound)	346 m/sec
A (Area of Oscillator/Enclosure)	0.07 m^2
z (Acoustic Propagation Loss)	0.01

The boundary condition at x = 0 is given by:

$$P_{r1}\big|_{x=0} = \frac{Ms^2 + Cs + K}{Ms^2 + (C + \rho_o c_o A)s + K} P_{L1}\big|_{x=0} + \frac{\rho_o c_o A s}{Ms^2 + (C + \rho_o c_o A)s + K} P_i \qquad \text{(D.1)}$$

The boundary condition at x = L is given by:

$$P_{r2}\big|_{x=L} = P_{L2}\big|_{x=L} \qquad \text{(D.2)}$$

The continuity equations at x = X are:

$$\begin{aligned} P_{r1}\big|_X &= P_{r2}\big|_X \\ P_{L1}\big|_X &= P_{L2}\big|_X \end{aligned} \qquad \text{(D.3)}$$

The leftward propagating wave at x = 0 can be written in terms of the rightward propagating wave at x = 0 using (D.3) and the propagation equation. The result is:

$$P_{L1}\big|_{x=0} = e^{-\frac{4\zeta kL}{2\pi}} e^{-2jkL} P_{r1}\big|_{x=0} \qquad \text{(D.4)}$$

The first term on the right side of (D.4) represents the propagation loss, while the second term governs the phase loss. The wave number is given by $k = \omega/c_0$. Substituting D.4 into D.1, the rightward propagating wave at x = 0 can be written only as a function of the incoming disturbance, P_i.

$$P_{r1}\big|_{x=0} = \frac{\rho_0 c_0 A s}{Ms^2 + (C + \rho_0 c_0 A)s + K - e^{-\frac{4\varsigma kL}{2\pi}} e^{-2jkL}(Ms^2 + Cs + K)} P_i \tag{D.5}$$

Finally, the propagation equation is used to relate the rightward and leftward propagating waves at x = X to the rightward propagating wave at x = 0.

$$\begin{aligned} P_{r1}\big|_X &= e^{-\frac{2\varsigma kX}{2\pi}} e^{-2jkX} P_{r1}\big|_{x=0} \\ P_{L1}\big|_X &= e^{-\frac{2\varsigma k(2L-X)}{2\pi}} e^{-2jk(2L-X)} P_{r1}\big|_{x=0} \end{aligned} \tag{D.6}$$

The total pressure is simply the sum of the leftward and rightward propagating waves.